Doctoral Dissertations   Student Scholarship

Spring 2001

Solar flare gamma-ray spectroscopy with CGRO-COMPTEL

Christopher Alex Young
University of New Hampshire, Durham

Follow this and additional works at: https://scholars.unh.edu/dissertation

Recommended Citation

Young, Christopher Alex, "Solar flare gamma-ray spectroscopy with CGRO-COMPTEL" (2001). *Doctoral Dissertations*. 30.
https://scholars.unh.edu/dissertation/30

INFORMATION TO USERS

This manuscript has been reproduced from the microfilm master. UMI films the text directly from the original or copy submitted. Thus, some thesis and dissertation copies are in typewriter face, while others may be from any type of computer printer.

The quality of this reproduction is dependent upon the quality of the copy submitted. Broken or indistinct print, colored or poor quality illustrations and photographs, print bleedthrough, substandard margins, and improper alignment can adversely affect reproduction.

In the unlikely event that the author did not send UMI a complete manuscript and there are missing pages, these will be noted. Also, if unauthorized copyright material had to be removed, a note will indicate the deletion.

Oversize materials (e.g., maps, drawings, charts) are reproduced by sectioning the original, beginning at the upper left-hand corner and continuing from left to right in equal sections with small overlaps. Each original is also photographed in one exposure and is included in reduced form at the back of the book.

Photographs included in the original manuscript have been reproduced xerographically in this copy. Higher quality 6" x 9" black and white photographic prints are available for any photographs or illustrations appearing in this copy for an additional charge. Contact UMI directly to order.

UMI®

Bell & Howell Information and Learning
300 North Zeeb Road, Ann Arbor, MI 48106-1346 USA
800-521-0600

SOLAR FLARE GAMMA-RAY SPECTROSCOPY
WITH
CGRO-COMPTEL

BY

C. Alex Young
BS, Florida State University, 1991
MS, University of New Hampshire, 1996

A DISSERTATION

Submitted to the University of New Hampshire
in Partial Fulfillment of
the Requirements for the Degree of

Doctor of Philosophy
in
Physics

May 2001

UMI Number: 3006151

UMI®

This dissertation has been examined and approved.

_____
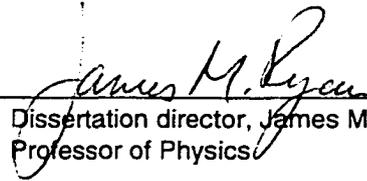
Dissertation director, James M. Ryan
Professor of Physics

_____
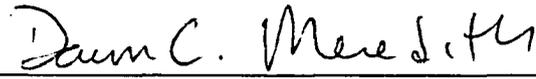
Dawn C. Meredith
Associate Professor of Physics

_____
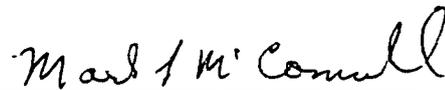
Mark L. McConnell
Research Associate Professor of Physics

_____
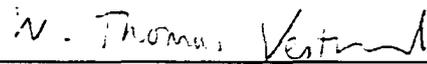
W. Thomas Vestrand
Space and Remote Sensing Sciences
Staff Member, LANL

_____

Martin A. Lee
Professor of Physics

_____

John R. Calarco
Professor of Physics

_____

4/27/01
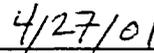
Date

For my family, the old and new.

iii

ACKNOWLEDGEMENTS

As is the case with most researchers, many people have provided comments, advice, and simple encouragement. Just as I believe that I have given proper credit in the text to the authors of books and papers from which I gained knowledge and research data, I give credit due those people who offered the most practical help, those who helped me to get through this process to a completed thesis.

I am most grateful to my advisor and mentor, Dr. James Ryan. He has been an inspiration and a driving force behind my journey to become a physicist.

Dr. Dawn Meredith as my advisor, teacher, colleague, and friend; I could not have gotten this far without her. She got me on track and successfully kept me there.

Much thanks to Dr. Mark McConnell. He is a great teacher and has been a valuable part of my committee. Also, thanks to my committee members Drs. Martin Lee, John Calarco, and Thomas Vestrand.

Drs. Eric Kolaczyk and Alanna Connors have been excellent teachers and guides in the world of statistics and in the application of Dr. Kolaczyk work.

All the necessary computer resources would have been useless without the skills of Dr. Tom Milliman, Rita Freuder, and John Labonte. Dorothy Kittredge, Patricia Frost, Nancy DeSchuiteneer, Rosemary Raynes, Katie Makem and Robbin Pendexter have only made graduate school better and kept everything going.

Many thanks to Drs. Gerhard Rank, Gerry Share, Ron Murphy, Richard Schwartz, Brian Dennis, Herman DeBrunner and Masato Yoshimori for all the help and advice concerning high-energy solar physics. I hope to continue the great work they have started and continue to do.

The completion of this thesis was certainly made possible by the support of my colleagues and friends at Greenbelt and in the SoHO group. Special thanks to Drs. Joe Gurman, Andy Endal, and Mario Perez for supporting both the time, expense, and resources necessary. Thanks to Jean Deselle and Jamie Serago, and Robin LeMaster. Thanks to Amy for the computer support and office mate moral boosting. And to Dr. Brian Thomas who understands.

I thank Drs. Richard Miller and Ben Hersh for many helpful comments and stimulating discussion that I will miss. Thanks to Drs. Cheenu Kappadath, Abe Falcone and Martina Arndt for their science insights. I thank Brett Austin for the statistics and computer help.

I also thank my current and former classmates Drs. Doug Biesecker, Eric Dors, Alan Tutein, Ioannis Kontodinas, Yuri Litvinenko and Marc Kippen and Valerie Boykin and Raid Suleman for all their technical and scientific help.

I very grateful to Drs. Jack Mulhern, Robert Lambert, and Joe Hollweg for both the opportunity and the pleasure of being their student. Special thanks to Dr. Mulhern for all his support and concern.

iv

Thanks to my parents for being such great parents and friends and seeing me to this goal.

Most importantly, I thank my wife and best friend, Hana. She has helped me to learn about myself and made my life wonderful. Her love, beauty, and wisdom keep me going.

TABLE OF CONTENTS

LIST OF TABLES

LIST OF FIGURES

x

xi

ABSTRACT

SOLAR FLARE GAMMA-RAY SPECTROSCOPY
WITH
CGRO-COMPTEL

by

C. Alex Young
University of New Hampshire, May 2001

The X-ray and γ-ray emission from solar flares provides important information about high-energy particles in solar flares. Energetic protons and ions interact with the solar atmosphere, giving rise to nuclear line emission at MeV energies and higher energy photons from the decay of neutral and charged pions. Electrons interact with the solar atmosphere producing a bremsstrahlung continuum. The solar flare spectrum is generally a superposition of these spectra with nuclear line emission dominating from ~1-8 MeV and the bremsstrahlung at lower and higher energies. The main goal of this thesis has been to explain a small part of a γ-ray flare observed by COMPTEL in June 1991.

A difficult interval to explain in the 11 June 1991 solar flare is the Intermediate (Rank 1997) or Interphase (Murphy and Share 1999; Dunphy et al. 1999) immediately following the peak of the impulsive phase. All three analyses of this flare using COMPTEL, OSSE and EGRET data yielded a hard proton spectrum with a power law index around 2 using the 2.2 to 4.44 MeV fluence ratio. This hard of a spectrum would indicate the presence of a high-energy component above eight MeV and emission due to spallation products. However, none of the three instruments observed such a component. We discuss the standard techniques used in solar flare spectral deconvolution and introduce a new technique we use with the COMPTEL observations.

This work presented the explanation that the proton spectrum is soft during this interval of the 11 June 1991 solar flare based on this new analysis of the COMPTEL observations. This means that the region of 2.223/4-7 MeV fluence space is largely unexplored for soft proton spectra. The use of this ratio must be reexamined for proton spectra with indices greater than 5 or 6. We then applied a model we developed for the transport of neutrons created from a soft proton spectrum to determine the photospheric ^{3}He abundance during this flare. We calculated a ^{3}He/H ratio of 8.7e-05 with a 1 σ range of 1.96e-04 to 1.75e-05 for this flare using this new model. This is larger than all previous values reported.

xii

In addition, we presented an additional flare observation from COMPTEL. In response to a BACODINE cosmic gamma-ray burst alert, COMPTEL on the CGRO recorded gamma rays above 1 MeV from the C4 flare at 0221 UT 20 January 2000. This event, though at the limits of COMPTEL's sensitivity, clearly shows a nuclear line excess above the continuum. Using new spectroscopy techniques we were able to resolve individual lines. This allowed us to make a basic comparison of this event with the GRL (gamma ray line) flare distribution from SMM and also compare this flare with a well-observed large GRL flare seen by OSSE. We showed this flare is normal, i.e., it is a natural extension of the SMM distribution of flares. The analysis of this flare means there is no evidence for a lower flare size for proton acceleration. Protons even in small flares contain a large part of the accelerated particle energy.

CHAPTER I

SOLAR FLARES

What is a Solar Flare?

Solar flares are abrupt, quick outbursts of energy 10^{28} to 10^{34} ergs on time scales of seconds to tens of minutes (Miller et al. 1997; Lang 1999). These energy releases occur in active regions, highly magnetized atmospheres associated with sunspots. Flares vary in frequency and intensity with the 11-year solar cycle. Solar flares have been detected over a large range of wavelengths, 17 orders of magnitude, from radio to gamma rays and with a variety of techniques. Large-scale magnetic field rearrangements produce relativistic electrons, ions, neutrons and other secondary particles.

What constitutes a flare is not completely agreed upon. Svestka (Svestka 1976) defines a flare as " a rapid temporary heating of a restricted part of the solar corona and chromosphere." To be clearer about what constitutes heating we chose the definition used by Golub and Pasachoff (Golub and Pasachoff 1997), that is, when material is heated to temperatures of 10^7 K or greater. One generally agreed upon basic fact is that magnetic fields play a crucial role in solar activity, particularly solar flares (Tandberg-Hanssen and Emslie 1988; Priest and Forbes 2000).

The First Observation

Carrington (Carrington 1859) and Hodgson (Hodgson 1859) independently observed the first reported visible light flare while observing a sunspot group. They observed a relatively rare event, a large "white light" flare. Flares generally only produce minor perturbations in the solar continuum emission. On the other hand, flares generate copious amounts of radio, UV and X-ray emission, several thousand times more intense than normal solar radiation in these wavebands. These emissions indicate the presence of high-energy electrons and plasma heated to tens of millions degrees.

Solar flare emission in radio was detected in the early days of radio astronomy (Southworth 1944; Hey 1945). Such emission is termed a radio burst because of its brief and energetic characteristics. Radio bursts in the millimeter and microwave bands indicate a population of nonthermal relativistic electrons. These electrons spiral around the intense magnetic fields of coronal loops producing synchrotron and gyrosynchrotron radiation. Longer wavelength radio emission indicates the presence of moving electrons (Bastian et al. 1998).

Up until the late 1950s solar flare, observations were confined to the ground based observatories, i. e., the radio and optical wavelengths. Ultraviolet, X-ray or gamma ray emission is absorbed by the Earth's atmosphere. Balloon experiments provided the first evidence for X-rays from flares (Peterson and Winckler 1959). The first images of solar flares in UV and X-ray came from the Skylab mission in 1973-74 (Eddy 1978).

Evidence for accelerated protons and nuclei was first provided by OSO-7 (Chupp et al. 1973). Theoretical calculations (Dolan and Fazio 1964; Lingenfelter and Ramaty 1967)) predicted nuclear γ–ray lines of energies between 0.511 and 7 MeV during a solar flare. These result from electron-positron annihilation and excited carbon, nitrogen, oxygen and other nuclei. During solar flare events of August 4 and August 7, 1972, OSO-7 observed clear evidence for 0.511, 2.2, 4.4 and 6.1 MeV γ–ray lines.

Until the launch of the Solar Maximum Mission (SMM) satellite in 1980, understanding of particle acceleration in solar flares was largely based upon charged particle measurements in space and X-ray and radio observations. Only a small number of flares with relativistic electrons and energetic ions had been detected. These data led to the "two phase" or "pre-SMM" (Vestrand and Miller 1999) paradigm for particle acceleration. This paradigm held that the energetization of particles occurred in two stages (Wild et al. 1963; de Jager 1969). During the first phase, particles are accelerated to about 100 keV, generating Type II radio bursts and hard X-ray emission. In the largest flares, a few minutes to a half an hour after the first phase, previously accelerated particles are boosted to higher energies. These particles generate γ–ray emission; Type III and IV radio bursts and energetic electrons and ions that escape into the interplanetary medium. This two step acceleration paradigm has the following observable predictions (Vestrand and Miller 1999):

3

1. The second phase (when it occurs) should be delayed by at least a few minutes with respect to the first phase. This delay should increase with particle energy.

2. The second phase acceleration is relatively rare. Therefore, γ–ray flares should be rare.

3. A size threshold should exist for the acceleration of high-energy particles.

4. Gamma ray and SEP measurements should be correlated for magnetically well-connected events (open solar magnetic field lines connect with the Earth's magnetic field).

A Standard Model – The Loop

Solar flares vary from simple to complex structures but the common element of a solar flare is the magnetic flux loop. Solar flares appear to be constructed of a dynamic loop or arcade of loops that connect regions of sunspots of opposite magnetic polarity. Near the apex of the loop, magnetic energy is released probably via magnetic reconnection (Tandberg-Hanssen and Emslie 1988; Priest and Forbes 2000), perhaps by emerging magnetic flux or colliding magnetic flux (Sturrock 1980). Figure 1.1 shows the canonical scenario for the release of magnetic energy in a solar flare loop. At the reconnection site, that is generally assumed to be the acceleration site (Tandberg-Hanssen and Emslie 1988; Lang 1999; Priest and Forbes 2000), nonthermal electrons and ions are accelerated to relativistic energies. During the first part of the flare, relativistic electrons (MeV energies) by way of gyrosynchrotron emit microwaves near the tops of the loops.

4

Electrons and ions travel along the magnetic structure towards the footpoints of the loop where they interact in the chromosphere. The electrons interacting with the ambient material produce nonthermal Bremsstrahlung. The protons and ions interact with the ambient chromospheric material producing gamma ray lines (via nuclear excitation and spallation reactions), energetic neutrons, and pions that
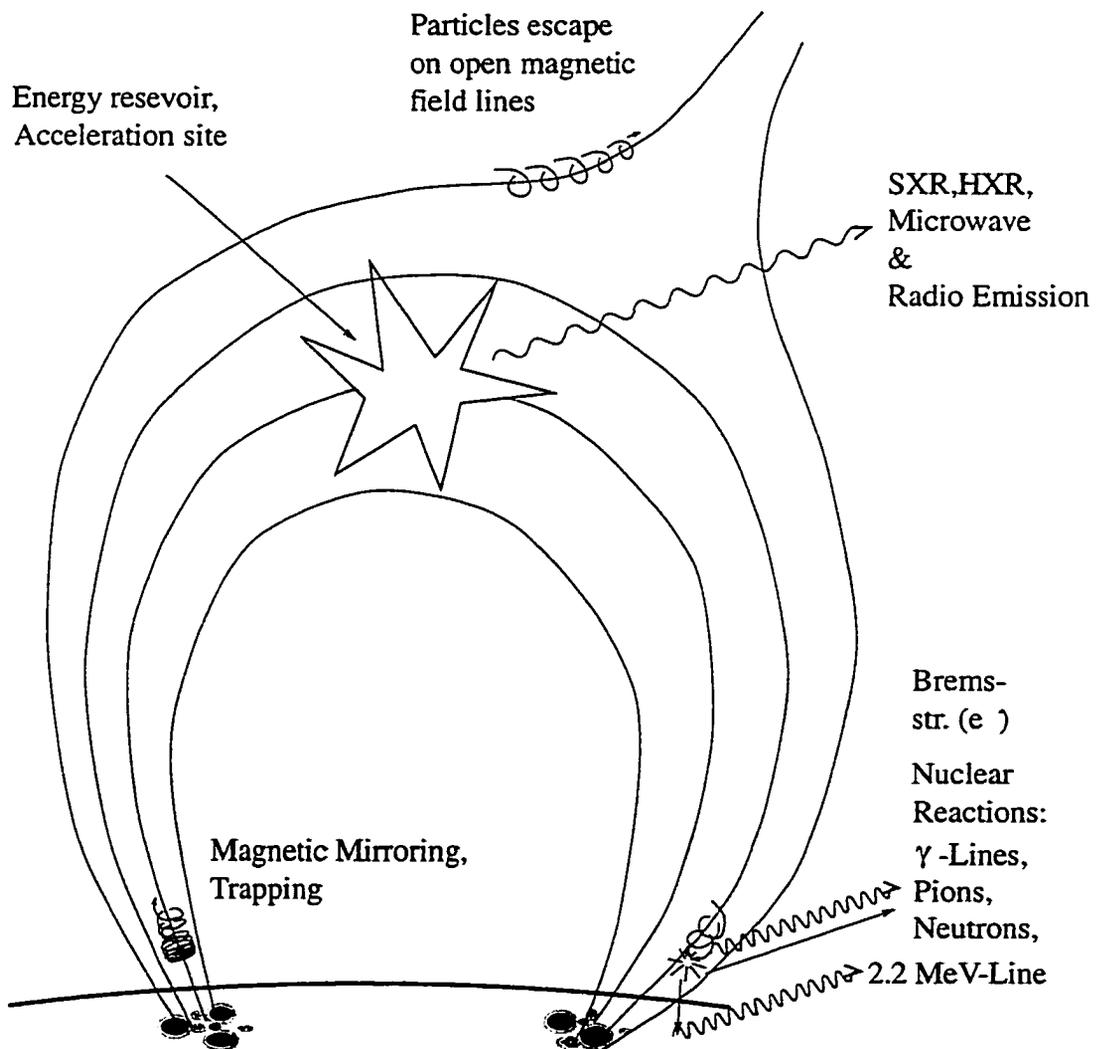
Figure 1.1 - Cartoon of the canonical solar flare magnetic loop. This drawing shows the respective locations of particle acceleration and radiation production. (Rank 1996)

5

then decay directly (π°) or indirectly ($\pi^\pm$) into γ-rays. When these particles interact in the chromosphere, they rapidly heat the plasma. Large pressure gradients cause the plasma to rise along the magnetic loops. This fills the loop with a several million-degree plasma that emits soft X-rays.

One way to classify this loop structure is by the extent of its confinement

as seen in Hα. This leads to the small, compact loop flare and the large, two-

ribbon flare (Heyvaerts et al. 1977; Tandberg-Hanssen and Emslie 1988). A

compact loop flare tends to take place in a small loop in the lower corona.

(a) Preflare Heating

(b) Impulsive Phase
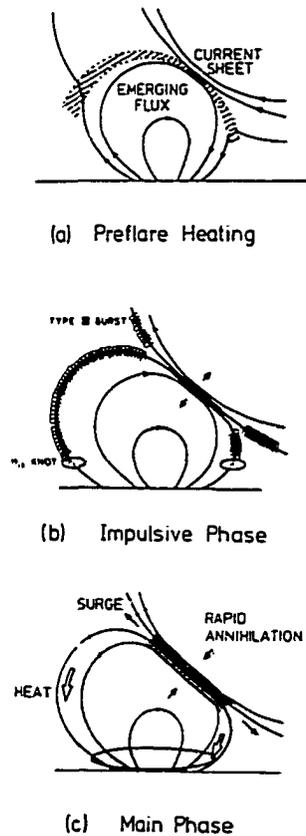
(c) Main Phase

Figure 1.2 - (a) Preflare phase: Emerging magnetic flux, current sheet formation and heating. (b) Impulsive phase: Reconnection, fast particle acceleration occurs. Hard X-rays and gamma rays are produced. (c) Main phase: Soft X-rays and Hα emission from heating of the loop and solar atmosphere. (Heyvaerts et al. 1977)

7

Its emission is mostly confined to the plasma in the loop. A two-ribbon flare is associated with an erupting prominence and the flare emission occurs in an arcade of post-flare loops (unfortunate term because they occur during not after the flare) along the prominence with the individual loops oriented basically at right angles to the prominence's long axis. Emission occurs at the feet of the
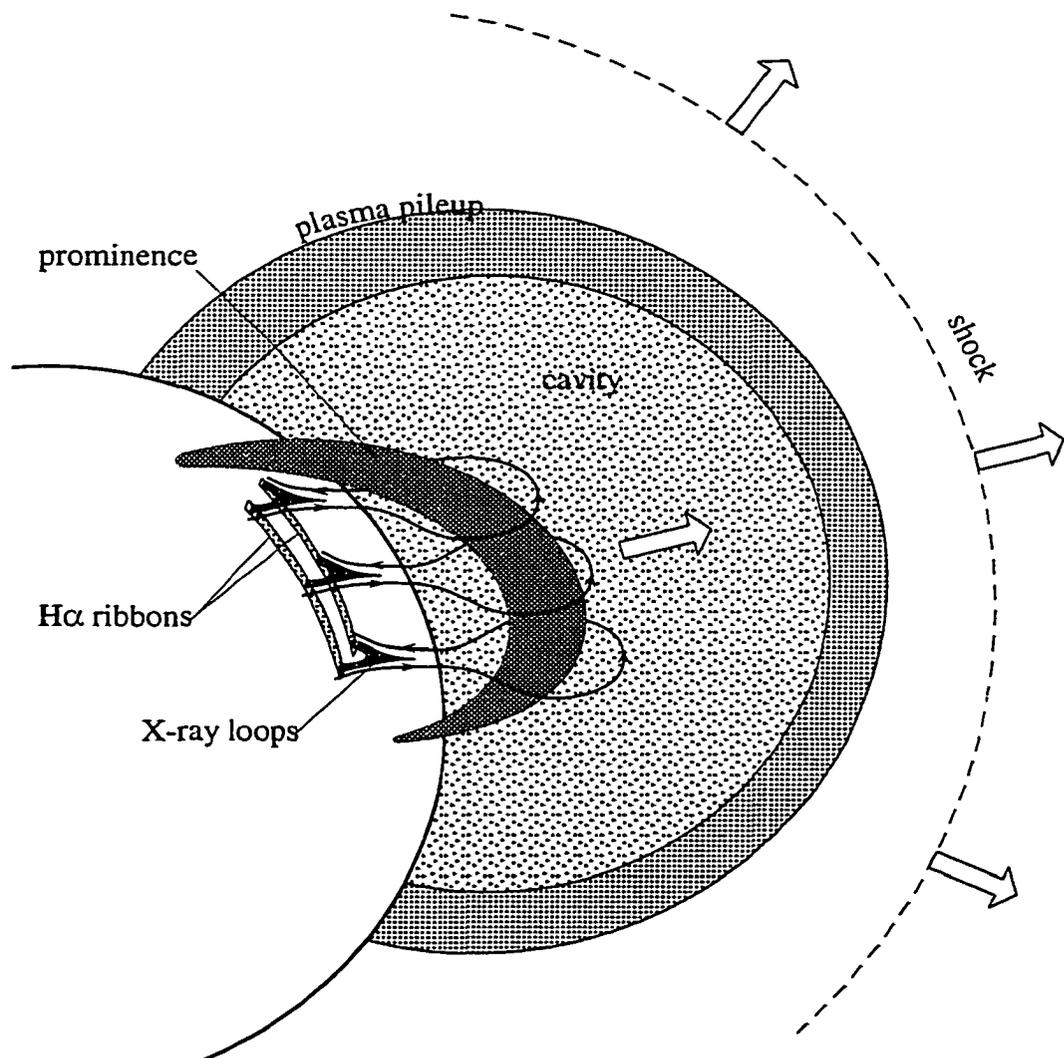
Figure 1.3 - Schematic diagram showing the relationship between various features associated with a CME. The shaded region labeled "plasma pileup" refers to the outer circular arc seen in coronagraphs. (Forbes 2000)

8

loops forming two ribbons along either side of the prominence. The triggering for both types of flares seems though to be the same, namely a large-scale eruption and reconnection of sheared magnetic fields (Tandberg-Hanssen and Emslie 1988).
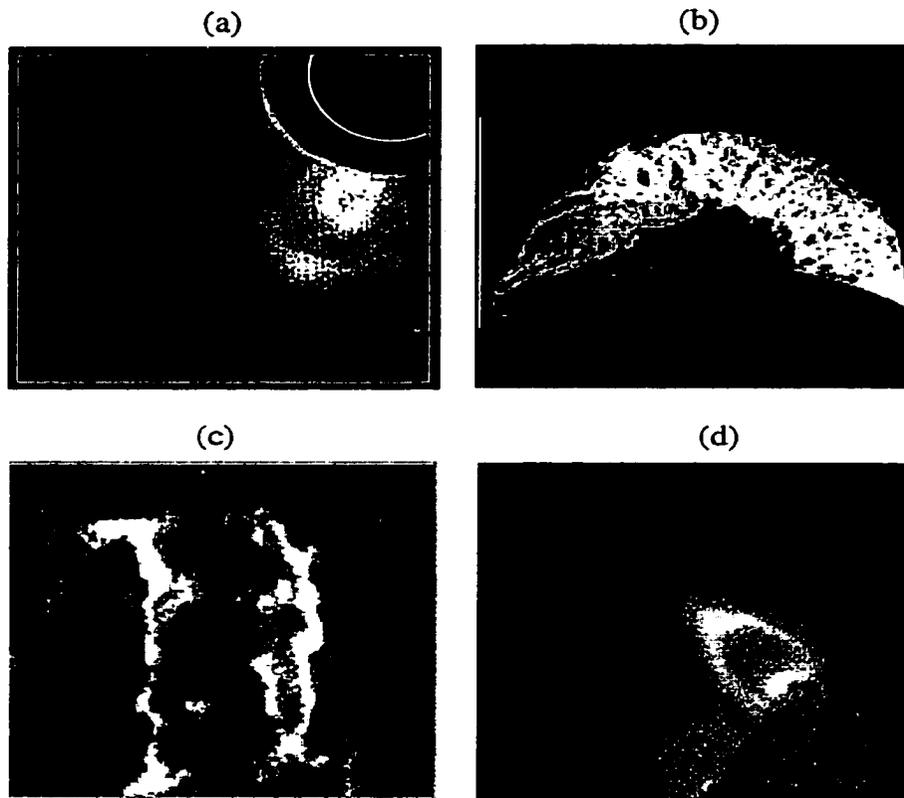
Figure 1.4 - Solar eruptive phenomena: (a) white light coronagraph image of a coronal mass ejection (CME) containing an erupted prominence. The white circular line in the upper right-hand corner indicates the location of the Sun's surface behind the occulting disk of the instrument (August 18, 1980, SMM archive, High-Altitude Observatory). (b) Hα image of the large prominence eruption, known as "granddaddy" (June 4, 1946, High-Altitude Observatory). (c) Ha ribbons produced by a flare associated with a CME (July 29, 1973, Big Bear Solar Observatory). (d) Cusp-shaped X-ray loop system, as seen on the limb of the Sun after an eruptive event (March, 8 1999, Yohkoh archive, Institute of Space and Astronautical Science). Such post eruption loop systems are common to the three phenomena of CMEs, erupting prominences, and large flares. (Forbes 2000)

9

Flare Classifications

Optical Classifications

Prior to the 1960s, flare classification relied on the visible part of the spectrum (Brown and Smith 1980). Solar flares on the disk of the Sun are observed as a temporary emission within some dark Fraunhofer line. The most commonly used is the Hα line (This is the Balmer α transition from n=3 to n=2 at 6563 Å). Flares are observed as brightening on the solar disk several times the intensity of the adjacent continuum. Area and brightness are the basis for optical classification. The term great flare is used when it covers an area of 10^{19} cm^2. The term subflare is used if the area covered is smaller than about 3×10^{18} cm^2. The standard units of measure for area are generally either millionths of a solar hemisphere or square degrees in heliographic coordinates. Because the above classification ignores flare brightness, an addition parameter is necessary.

Area (Millionths of a solar hemisphere)	Area (square degrees heliographic)[1]	Importance Faint (F), normal (N), and bright (B)
<100	<2.06	S (subflare)
100-250	2.06 - 5.15	1
250-600	5.15-12.4	2
600-1200	12.4-24.7	3
>1200	>24.7	4

Table 1.1 Solar flare optical classification based on area and brightness measurements in the Hα waveband.

---

[1] Square degrees heliocentric = 1.48e18 cm^2

10

(A small flare can be very bright whereas a large flare can be dim.) The intensity classifications of faint (F), normal (N), and brilliant (B) completes the dual importance scheme shown in Table 1.1.

Soft X-ray Classifications

Recent data suggest that the X-ray signature of flares may be as good as if not better than optical characteristics for classify flares. Given the definition that we stated earlier for solar flares (T> 10^7K), X-rays would seem to also provide better physical insight.

The most commonly used classification today is based on the integrated total output of soft X-rays during a flare. (We call ~10 keV photons soft X-rays (SXR), ~100 keV photons hard X-rays (HXR), and greater than ~1 MeV photons γ rays). Using the SXR band pass of 1-8 Å (1.6 – 12.4 keV), flares are classified as C, M, or X flares as listed in Table 1.2.

Class	Intensity (erg cm^2 s^{-1})	(W m^2)
B	10^{-4}	10^{-7}
C	10^{-3}	10^{-6}
M	10^{-2}	10^{-5}
X	10^{-1}	10^{-4}

Table 1.2 Solar flare soft X-ray classification system based on the integrated total output of soft X-rays measured by the GOES satellites for 1-8 A.

The letter represents the flux order of magnitude and an associated number indicates the multiple of that order of magnitude (e.g. M3 $\Rightarrow$ 3×10^{-2} erg cm^{-2} s^{-1}). The class B was added to include subflares (smaller than class C).

11

Extreme examples of this classification scheme are $X12 = 1.2$ erg cm^{-2} s^{-1} and

$B.6 = 6 \times 10^{-05}$ erg cm^{-2} s^{-1}. Current classifications are based on the measurement

of the Geosynchronous Operational Environmental Satellites (GOES). X12 is the

maximum greatest measurable flux for current GOES detectors.

Hard X-ray Classifications

For hard X-ray, Dennis (Dennis 1985; Dennis 1988) presented a

classification scheme first proposed by Tanaka (Tanaka 1983) and expanded by

Tsuneta (Tsuneta 1983) and Tanaka (Tanaka 1987). This classification groups

flares into three types according to their temporal, spectral, and spatial hard X-

ray characteristics.

1. Type A or Hot Thermal Flares:

    Temporal: gradual rise and fall of hard X-ray emission at energies below ~40
    keV; weak impulsive emission at higher energies;
    Spectral: thermal fit below 40 keV with temperatures of 3-4 x 10^7 K, very
    steep spectra above 40 keV with power-law $\gamma \geq 7$;
    Spatial: compact (<5000 km)

2. Type B or Impulsive Flares:

    Temporal: typical impulsive hard X-ray spikes with variability on time-scales of
    seconds;
    Spectral: soft spectrum on the rise becoming harder at the peak and again on
    the decay; often exponential or broken power-law on the rise and at the peak,
    changing to a single power-law on the decay;
    Spatial: emission from the low altitude including footpoints at the peak,
    evolving to a more compact source at the higher altitude later in the flare.

3. Type C or Gradual Flares:

    Temporal: gradually varying hard X-ray emission on time scales of minutes
    sometimes lasting for 30 minutes or longer;

12

Spectral: spectrum above ~50 keV hardens with time with γ decreasing monotonically from ≥ 5 early in the flare to ≤ 2 later in the flare after the peak; Spatial: the source is located at high altitudes of $\geq 4 \times 10^4$ km.

Figure 1.5 shows the time evolution of the Hα, soft X-ray and hard X-ray

emission produced by a flare on August 28, 1966.
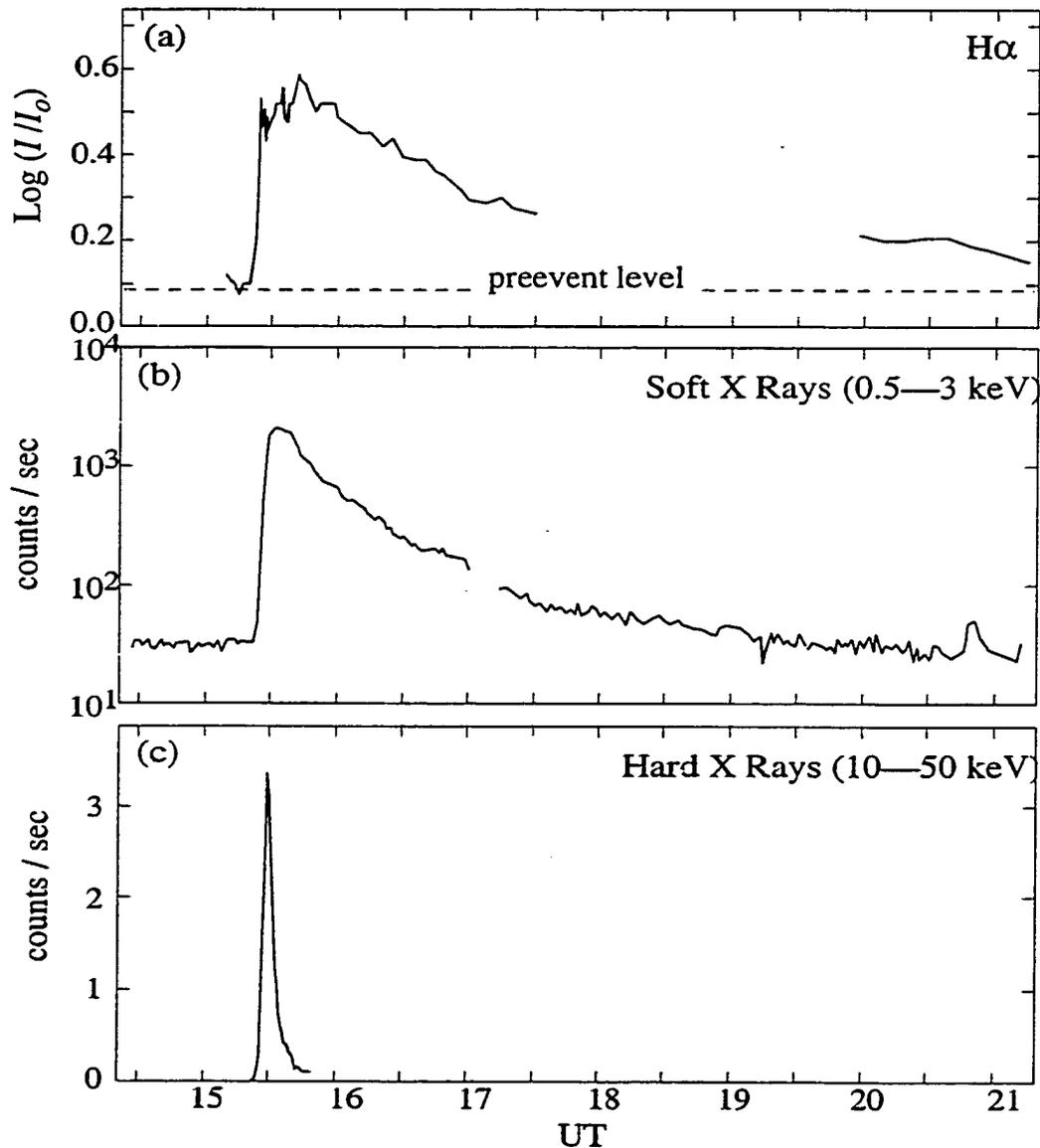
Figure 1.5 - Time evolution of the radiation produced by a flare on August 28, 1966, which was associated with both a two-ribbon flare and a prominence eruption: (a) Hα ribbon intensity (Dodson and Hedeman 1968), (b) thermal, soft X-ray emission (Zirin and Lackner 1969), and (c) nonthermal, hard X-ray emission (Arnoldy et al. 1968). (Forbes 2000)

13

Particle Acceleration

In order to explain the intense radiation produced in solar flares we must first understand the acceleration of electrons and ions that produce the radiation. Many important questions need to be answered such as, What types of particles are accelerated? Where are they accelerated? How fast are they accelerated and how much energy do they contain? By what processes are they accelerated? These are difficult questions and are still subjects of ongoing research (Melrose 1994; Miller et al. 1997; Priest and Forbes 2000). Here we discuss some of the more favored mechanisms believed to be responsible for particle acceleration in solar flares.

Since we believe magnetic reconnection to be the main source of energy release in flares, we have many of the needed elements, including heating, plasma flows, turbulence, shocks and electric fields. Unfortunately, the problem is not simple. Excluding collisions, the only way to perform work to accelerate charged particles is with electric fields, because the only nonzero term in the Lorentz force is $V \cdot E$. However, large-scale parallel (to B) electric fields are quickly shorted out in the highly conducting plasma (Melrose 1994; Priest and Forbes 2000). Consequently, how one generates of the required electric fields is not so obvious. In the environment of solar flares, there are three strong candidates.

14

Direct Electric Fields

The most straightforward form of acceleration is by parallel electric fields, where ions are accelerated in one direction and electrons in the other. As we stated earlier, plasmas are highly conducting and parallel electric fields are quickly shorted out. There must be a localized region with some form of anomalous resistivity for the electric fields to be maintained. This anomalous resistivity could be due to low-frequency electrostatic waves or double layers. Double layers fall into two classes: weak and strong. Double layers (WDL) in the solar environment have a potential drop on the order of T_e/e (with temperature T_e in units of energy) and are formed by regions of turbulent waves. A single double layer is not effective for flares (Melrose 1994) but a series of WDLs may produce stochastic acceleration (discussed below) by low-frequency waves.

A region that separates two oppositely directed magnetic fields is called a neutral sheet and must contain an electric field. A particle entering the neutral sheet is subject to a net drift in the direction of decreasing electric potential so it has a high probability of emerging with a higher energy. One of the original versions of this model was introduced by Speiser (1965) to explain particle acceleration in magnetotail. An advanced version of this model was employed by Litvinenko (1996) in the context of particle acceleration in solar flares.

Stochastic Acceleration

Stochastic acceleration can be defined as any process in which a particle can either gain or lose energy instantaneously but systematically gains energy

15

over a long time (Miller et al. 1997; Vestrand and Miller 1999). This idea was first proposed by Fermi (Fermi 1949) as a mechanism for accelerating cosmic rays. Later the mechanism was further invoked as a diffusive process (Parker 1957). Lee derived the relativistically correct hard sphere diffusion coefficient from the covariant Boltzmann equation (Lee 1994).

Stochastic acceleration by low-amplitude waves was proposed to be caused by a resonant wave-particle interaction in which the Doppler-shifted wave frequency in the particle's guiding center frame equals a multiple of the gyrofrequency. Transit-time damping (Lee 1973) due to a resonance with fast-mode MHD waves is extremely efficient for electron acceleration under flare conditions where the Alfvén speed is comparable to the electron thermal speed (Miller 1996). It is a promising mechanism for explaining hard X-ray spikes.

Another flare particle acceleration mechanism is stochastic Fermi acceleration with large-amplitude fast-mode waves produced by many small reconnection sites (LaRosa et al. 1996). Alfvén waves generated by reconnection and cascading to short wavelengths have been invoked for ion acceleration (Miller and Ramaty 1992; Miller and Aaron 1995; Miller and Moore 1996). Ion abundance enhancements may be caused by a gyro-resonance with electrostatic or electromagnetic waves that are close to the cyclotron frequency of the ion (Fisk 1978). For example, the enhancement of the ^{3}He/^{4}He ratio from the normal coronal value of 5×10^{-4} to 0.1 has been explained by Temerin and Roth (Temerin and Roth 1996) and Litvinenko (Litvinenko 1996) using electromagnetic ion-

16

cyclotron waves. Furthermore, lower-hybrid waves may account for radio emission, but do not appear to accelerate enough electrons for hard X-ray bursts (Vlahos et al. 1982; McClements et al. 1993).

Shock Acceleration

Shock waves are also a natural particle accelerator in solar flares and coronal mass ejections. They are present at the reconnection region (as slow-mode shocks) and where the reconnection jet meets the ambient field (as a fast-mode shock), and they also propagate away from the flare site (as fast-mode shocks) where they show up as Moreton waves and Type II radio bursts. Electron-drift acceleration is probably important in Type II radio bursts (Holman and Pesses 1983). Diffusive acceleration is more likely at fast-mode shocks than slow-mode shocks, since the scattering centers tend to converge towards the shock in the shock frame of the fast shock but not a slow shock (Isenberg 1986). It is a viable mechanism for ion acceleration up to 100 MeV in less than 1 s (Ellison and Ramaty 1985). Furthermore, Tsuneta and Naito (Tsuneta and Naito 1998) have suggested the acceleration of 20-100 keV nonthermal electrons in about 0.3-0.6 s at the fast shock in the reconnection jet below the reconnection site. As in many mechanisms, such electrons could create the commonly observed double-source hard X-ray structure at the chromospheric footpoints of the reconnected field lines.

Acceleration by fast-mode shock waves may be separated into two forms: diffusive shock acceleration (DSA) and shock drift acceleration (SDA). DSA

17

requires effective scattering such that a given particle cycles across the shock many times (Axford et al. 1977; Gubchenko and Zaitsev 1979; Achterberg and Norman 1980; Kocharov and Kovaltsov 1992; Anastasiadis and Vlahos 1994; Blandford 1994; Hirayama 1994). DSA is the widely accepted mechanism for the acceleration of Galactic cosmic rays and is a plausible mechanism for the acceleration of higher energy solar energetic particles. However, the available evidence suggests that prompt acceleration of ions is not due to a single strong shock (Nakajima et al. 1990). DSA by a collection of weak shocks remains a possibility, and this may be treated as a form of acceleration by MHD (fast-mode) turbulence. The difference between this and stochastic acceleration is that since the scattering centers are moving towards each other in the rest frame of the shock, there is a first-order energy gain with each interaction so that the acceleration is much faster.

Particle Transport and Interaction

Once particles are accelerated, they interact with the surrounding solar medium. It is this interaction that facilitates the processes that create the radiation from the accelerated particles. Though the particle interaction and transport processes are complex, the overall processes can be characterized by the paradigms if "thin" and "thick" target interactions. (The dynamics of the interaction and transport processes contain a great deal of information on the high-energy solar flare. We will not cover these topics here but many excellent papers covered the range of complexity and detail, e.g., (Melrose and Brown

18

1976; Zweibel and Haber 1983; Ryan 1986; Hulot et al. 1989; Ryan and Lee 1991; Fletcher 1997; Ryan 1999).)

We consider a population of accelerated particles interacting in a homogeneous volume of an ambient medium (Lingenfelter and Ramaty 1967; Ramaty et al. 1975; Kuzhevskii 1982; Kocharov 1988; Chupp 1976). The instantaneous production rate of secondary particles is

$$q(E_s,t) = n\int_0^\infty dE N(E,t) c\beta\sigma(E) f(E,E_s) \quad (2.1)$$

where n is the ambient number density and N(E,t) is the instantaneous number of accelerated particles per unit energy per nucleon at time t. The variables E and E_s are the energies per nucleon of the primary and secondary particles; $c\beta$ is the velocity of the primary particles; $\sigma(E)$ is the cross-section for the production of secondaries as a function of E and $f(E,E_s)dE_s$ is the probability that a secondary particle produced by a primary particle of energy per nucleon E will have energy per nucleon in dE_s around E_s. We assume the particles are produced in the interaction region at a rate of Q(E,t) and if they lose energy or escape from this volume then N(E,t) is related to the production rate by the continuity equation

$$\frac{\partial N(E,t)}{\partial t} + \frac{\partial}{\partial E}\left[\left(\left|\frac{dE}{dt}\right|_{loss}\right)N(E,t)\right] + \frac{N(E,t)}{T_{esc}(E,t)} = Q(E,t) \quad (2.2)$$

$\left|\frac{dE}{dt}\right|_{loss}$ is the energy loss rate, T_{esc} is the mean escape time. They both can depend on energy and time. Assuming they are dependent only on energy, the solution to this equation is

19

$$N(E,t) = \left.\left|\frac{dE}{dt}\right|_{loss}^{-1} \int_E^\infty dE' Q(E,t) \exp\left(\frac{-\tau(E)}{t_{esc}}\right)\right. \quad (2.3)$$

where is $t' = t - \tau(E) = t - \int_E^{E'} \dfrac{dE''}{\left|\frac{dE}{dt}\right|_{loss}(E'')}$. There are two important limiting cases

for which standard limits are applied.

Thin-Target Interaction Model

Nuclear reactions are produced by energetic particles that escape from the interaction region at the Sun. These particles can then be detected in the interplanetary medium and if there are a sufficient number of thin-target reactions, secondary products could be detected. The escape time must be sufficiently short so that the source $Q(E,t)$ does not vary appreciably over a time t_{esc} and an energy interval E'-E. For the interval E' to E, $t_{esc}\left|\frac{dE}{dt}\right|_{loss}$ is approximately constant so $N(E,t) = t_{esc}(E)Q(E,t)$.

Thick-Target Interaction Model

Nuclear reactions are produced by particles slowing in the solar atmosphere. Particles and their secondaries thermalize and mix with the solar atmosphere. We still see high-energy neutrons and γ-ray lines from these thick interactions. At all energies of interest, $t_{esc} \gg t - t'$ so

$$N(E,t) = \left|\frac{dE}{dt}\right|_{loss}^{-1} \int_E^\infty dE' Q(E,t). \quad (2.4)$$

We assume conditions are such that electrons, protons, alphas, nuclei of carbon, nitrogen, oxygen, neon and heavier elements are accelerated

20

somewhere in the chromosphere or corona. Accelerated particles interact with atoms, ions, and fields in the solar atmosphere. Interaction results in direct (collisional) excitation of nuclear states, nuclear disintegration and production of neutrons, X-rays, γ-ray lines, new elements, and isotopes. The γ-rays and high-energy neutrons probe behavior of sub-relativistic and relativistic ions. The X-ray and γ-ray continuums probe sub-relativistic and relativistic electrons.

Particle, X-ray, and Gamma-ray Production

In the next sections we discuss some of the important radiation mechanisms and emission types in hard X ray through gamma-ray energies (as well as high energy particles.) In the first section we discuss the thermal emission process for a super-hot plasma and the non-thermal emission from high-energy electrons. The last four sections discuss the nuclear gamma-ray emission component and solar energetic particles.

Bremsstrahlung

A flaring region of the Sun, because it a superheated plasma, necessarily contains large numbers of free electrons. These free electrons when accelerated, radiate efficiently by free-free or Bremsstrahlung emission by interacting with ions. This type of Bremsstrahlung is categorized into two types depending on the velocity distribution of the electrons. If the electrons have a thermal distribution characterized by the average temperature of the background plasma the electrons radiate via thermal Bremsstrahlung. If the electron population has a non-thermal distribution then the emission is further classified as 'thin'-target if

21

the electrons escape from the interaction region or 'thick'-target if they slow down and thermalize in the interaction region (Tandberg-Hanssen and Emslie 1988; Lang 1999).

Thermal

For a solar flare, we can have hot plasmas with temperatures on the order of 10^8K or kT $\approx$ 9 keV, meaning that X-rays are produced. Thermal Bremsstrahlung is more efficient than non-thermal Bremsstrahlung because the thermal electrons only lose a small fraction of their energy to the cooler ambient electrons by Coulomb collisions.

In a plasma of volume V, a uniform density hot electron plasma, n_e, with a Maxwellian velocity distribution f(v) has an energy distribution of

$$f_E(E) = f(v)\,dv/dE = \frac{2n_e}{\pi^{1/2}(kT)^{3/2}} E^{1/2} \exp(-E/kT) \text{ electrons cm}^{-3} \text{ erg}^{-1}.(2.5)$$

These electrons interact with ambient stationary protons n_i producing isotropic Bremsstrahlung emission given by

$$I(\varepsilon) = \int_V n_i dV \int_\varepsilon^\infty f_E(E)v(E)\sigma_B(\varepsilon,E)dE ,(2.6)$$

where $\sigma_B(E,\varepsilon)$ is the Bremsstrahlung cross-section. For energies less than 511keV (of photons & electrons) the cross-section is well approximated by the angle-integrated Bethe-Heitler cross-section (Koch and Motz 1959),

$$\sigma_B(\varepsilon,E) = \frac{8\alpha}{3}r_0^2 \frac{m_e c^2}{\varepsilon E} \log\frac{1+(1-\varepsilon/E)^{\frac{1}{2}}}{1-(1-\varepsilon/E)^{\frac{1}{2}}} \text{ cm}^2 \text{ keV}^{-1} .(2.7)$$

22

Relativistic corrections and directionality are important for energies comparable to the electron rest mass, 511 keV. The cross-section scales proportional to Z^2 to account for this and the solar atmospheric composition the abundance-weighted $\overline{Z^2}$ is included giving

$$\sigma_B(\varepsilon, E) = \frac{\kappa_{BH}\overline{Z^2}}{\varepsilon E} \log \frac{1 + (1 - \varepsilon/E)^{\frac{1}{2}}}{1 - (1 - \varepsilon/E)^{\frac{1}{2}}} \quad cm^2 \; keV^{-1} \; ,(2.8)$$

where $\kappa_{BH} = 7.9 \times 10^{-25} \, cm^2 \, keV$.

To solve for $I(\varepsilon)$, first a change of variables $E = \varepsilon(1+x)$ is made and the

function $g(a) = \int_0^\infty \frac{e^{-ax}}{[x(1+x)]^{1/2}} dx$ is defined. Integrating by parts one obtains

$$I(\varepsilon) = \frac{D}{\varepsilon} \int_0^\infty \frac{Q(T)}{T^{1/2}} \exp(-\varepsilon/kT) g(\varepsilon/kT) dT \; (2.9)$$

where $D = (8/\pi m_e k)^{1/2} \kappa_{BH} \overline{Z^2} \, cm^3 s^{-1} K^{1/2}$ and $Q(T) = \int n_i n_e \frac{dV}{dT}$. Q(T) is the emission measure for a non-homogeneous, non-isothermal source.

Non-thermal

Instead of a thermal population, now a suprathermal population with differential energy spectrum $F(E_0)$ (electrons $cm^{-2} \, s^{-1} \, keV^{-1}$) is considered. To calculate the X-ray flux $I(\varepsilon)$ (photons $cm^{-2} \, s^{-1} \, keV^{-1}$) observed at the Earth, originating from a flare of area S, the target region must be specified as either thin or thick-target.

For the thin-target case, $I(\varepsilon)$ is,

$$I(\varepsilon) = \frac{S\Delta N}{4\pi R^2} \int_\varepsilon^\infty F(E_o)\sigma_B(\varepsilon, E_o)dE_o \quad photons \; cm^{-2} \, s^{-1} \, keV^{-1} \; (2.10)$$

23

where R = 1AU, $\Delta N = \int\limits_{source} n_p(s)ds$ is the column density of the source and n_p is

the ambient proton density.

In the thick-target case, $I(\varepsilon)$ is calculated in the same fashion except $F(E_0)$

is the target averaged electron flux. So to express $I(\varepsilon)$ in terms of the injected

spectrum we must consider energy losses (Tandberg-Hanssen and Emslie

1988). For the simplest case only Coulomb collisions with ambient particles are

considered. The energy loss rate is $\dfrac{dE}{dt} = -\sigma_E(E)n_p v(E)E$ with

$\sigma_E = 2\pi e^4 \log\Lambda/E^2 = C/E^2$. The number of photons emitted per unit energy by an

electron of initial energy E_0 is

$$m(\varepsilon, E_o) = \int\limits_{t_1(E=E_0)}^{t_2(E=\varepsilon)} n_p(s(t))\sigma_B(\varepsilon, E(t))v(E(t))dt \quad (2.11)$$

or using the energy loss rate dE/dt to change variables gives

$$m(\varepsilon, E_o) = \int\limits_{\varepsilon}^{E_o} \frac{\sigma_B(\varepsilon, E)dE}{E\sigma_E(E)} . \quad (2.12)$$

The Bremsstrahlung flux observed at Earth due to a thick target is

$$I(\varepsilon) = \frac{S}{4\pi R^2} \int\limits_{E_o=\varepsilon}^{\infty} F(E_o)m(\varepsilon, E_o)dE_o .(2.13)$$

Substituting equation (2.12) one can write this equation in the same form as the

equation for thin-target by defining an effective column density ΔN_{eff},

$$\Delta N_{eff} = \frac{1}{C\sigma_B(\varepsilon, E_o)} \int\limits_{\varepsilon}^{E_o} E\sigma_B(\varepsilon, E)dE .(2.14)$$

24

The effective column density behaves as E_0^2 and corresponds roughly to the column density needed to stop an electron of injected energy E_0. Electrons of energy $E>\varepsilon$ are the principle contributors to photons of energy ε, especially when $F(E_0)$ rapidly decreases as a function of energy. The thin-target model is a good approximation when $\Delta N < \Delta N_{eff}(\varepsilon)$ and the thick-target model is when $\Delta N > \Delta N_{eff}(\varepsilon)$ (Tandberg-Hanssen and Emslie 1988).

If an electron source function of the form $F(E_0) = AE_0^{-\delta}$ is assumed the thin and thick-target cases can be written respectively as,

$$I_{thin}(\varepsilon) = \frac{S\Delta NA}{4\pi R^2} \frac{\kappa_{BH}\overline{Z^2}}{\varepsilon} \int_\varepsilon^\infty E_0^{-(\delta+1)} \log\frac{1+(1-\varepsilon/E)^{\frac{1}{2}}}{1-(1-\varepsilon/E)^{\frac{1}{2}}} dE$$

and $\quad\quad\quad\quad\quad\quad\quad\quad\quad\quad\quad$.(2.15)

$$I_{thick}(\varepsilon) = \frac{SA}{4\pi R^2 C} \frac{\kappa_{BH}\overline{Z^2}}{\varepsilon} \int_\varepsilon^\infty E_0^{-\delta} \int_\varepsilon^E \log\frac{1+(1-\varepsilon/E)^{\frac{1}{2}}}{1-(1-\varepsilon/E)^{\frac{1}{2}}} dE dE_0$$

For the thin-target case the integral can be evaluated by parts. Substituting $x=\varepsilon/E_0$ and using the standard beta function

$$B(a,b) = \int_0^1 x^{a-1}(1-x)^{b-1} dx,$$

$$I_{thin}(\varepsilon) = \frac{S\Delta NA}{4\pi R^2} \kappa_{BH}\overline{Z^2} \frac{B(\delta, 1/2)}{\delta} \varepsilon^{-(\delta+1)} .(2.16)$$

The hard X-ray spectrum is a power law $I_{thin}(\varepsilon) = a\varepsilon^{-\gamma}$ with $\gamma=\delta+1$ and

$$a = \frac{S\Delta NA}{4\pi R^2} \kappa_{BH}\overline{Z^2} \frac{B(\gamma-1, 1/2)}{\gamma-1} .(2.17)$$

25

For the thick-target case, it is helpful to change the order of integration in

the double integral $\int\limits_{\varepsilon}^{\infty E}\int\limits_{\varepsilon} dEdE_0 \rightarrow \int\limits_{E=\varepsilon}^{\infty}\int\limits_{E_0=E}^{\infty} dEdE_0$. The integral is then evaluated by

parts giving

$$I_{thick}(\varepsilon) = \frac{SA}{4\pi R^2 C}\kappa_{BH}\overline{Z^2}\frac{B(\delta-2,1/2)}{(\delta-1)(\delta-2)}\varepsilon^{-(\delta-1)}.(2.18)$$

As in the thin-target case $I_{thick}(\varepsilon)$ is a power law $I_{thick}(\varepsilon) = a\varepsilon^{-\gamma}$ with $\gamma=\delta-1$ and

$$a = \frac{SA\kappa_{BH}\overline{Z^2}}{4\pi R^2 C}\frac{B(\gamma-1,1/2)}{\gamma(\gamma-1)}.(2.19)$$

Comparing the equations for thin-target and thick-target X-ray flux, the thick-

target is that of the thin-target with an effective injected electron flux of

$$F_{eff}(E_0) = \frac{A}{\delta-1}\left(\frac{E_0^2}{C\Delta N}\right)E_0^{-\delta}.$$ This is two powers of E_0 harder (or flatter) than $F(E_0)$

$= AE_0^{-\delta}$. Formulae (2.16) and (2.17) or (2.18) and (2.19) allow properties of the

injected electron flux to be inferred from the hard X-ray flux once a power law

electron spectrum and thin or thick-targets are assumed. In addition, the integral

electron flux and energy fluxes above some reference energy E_1 are defined as

$$F_1 = \int\limits_{E_1}^{\infty} AE^{-\delta}{}_0 dE_0 \text{ and } \mathcal{S}_1 = \int\limits_{E_1}^{\infty} AE^{-\delta}{}_0 E_0 dE_0 \text{ respectively.}$$

Prompt Nuclear Lines

Collisionally excited nuclei rapidly (~ns) radiate excess energy falling to

their ground state. Each isotope has a characteristic γ-ray line. Some of the most

important lines originating from direct excitations are:

26

Element	Energy (MeV)	Element	Energy (MeV)
Delayed Line		**Proton Excitation**	
$e^+ + e^-$	0.511	^{14}N	5.105
(pair			2.313
annihilation)			
$^2H = ^2D$	2.223		
(neutron		^{20}Ne	1.634
capture)			2.613
			3.34
Spallation			
^{12}C	4.438	^{24}Mg	1.369
			2.754
^{16}O	6.129	^{28}Si	1.779
	6.917		6.878
	7.117	^{56}Fe	0.847
	2.714		1.238
Alpha			1.811
Excitation			
^7Be	0.431		
^7Li	0.478		

Table 3 Some of the gamma-ray lines from solar flares. The lines marked with an asterisk * are the most prominent and were detected in the 4 June 1991 flare with OSSE (Murphy et al. 1990; Murphy et al. 1991; Murphy et al. 1997). (Table adapted from (Lang 1999))

Some strong lines come from the fusion reactions, $^4He(\alpha, p)$ $^7Li^*$ and $^4He(\alpha, n)$

$^7Be^*$. Their energies are 0.48 MeV (Li) and 0.43 MeV (^7Be). The lifetimes of the excited states are negligible compared to the particle acceleration time and the changing secondaries' production rates, thus, the name prompt lines. This means these lines can serve as a timing of particle acceleration and interaction. The rate of nuclear interactions is directly proportional to the instantaneous number of accelerated particles in the interaction region, which in turn is governed by the acceleration mechanisms and energy losses of the particles. The probability of direct excitation of nuclei is typically a maximum around 10

MeV and accelerated particles have a falling spectrum. This means that nuclear γ-ray lines contain information on 10-20 MeV particles.

Delayed Lines

The Neutron Capture Line

These lines are emitted over a long time interval compared to the production time of secondaries. Neutron capture by hydrogen (protons) produces deuterium and a 2.223 MeV γ-ray line, $^1H + n \rightarrow {}^2D + \gamma_{2.223\ MeV}$. Neutrons are created in several reactions, pp, pα, αα, pCNO, and αCNO. Neutrons from soft
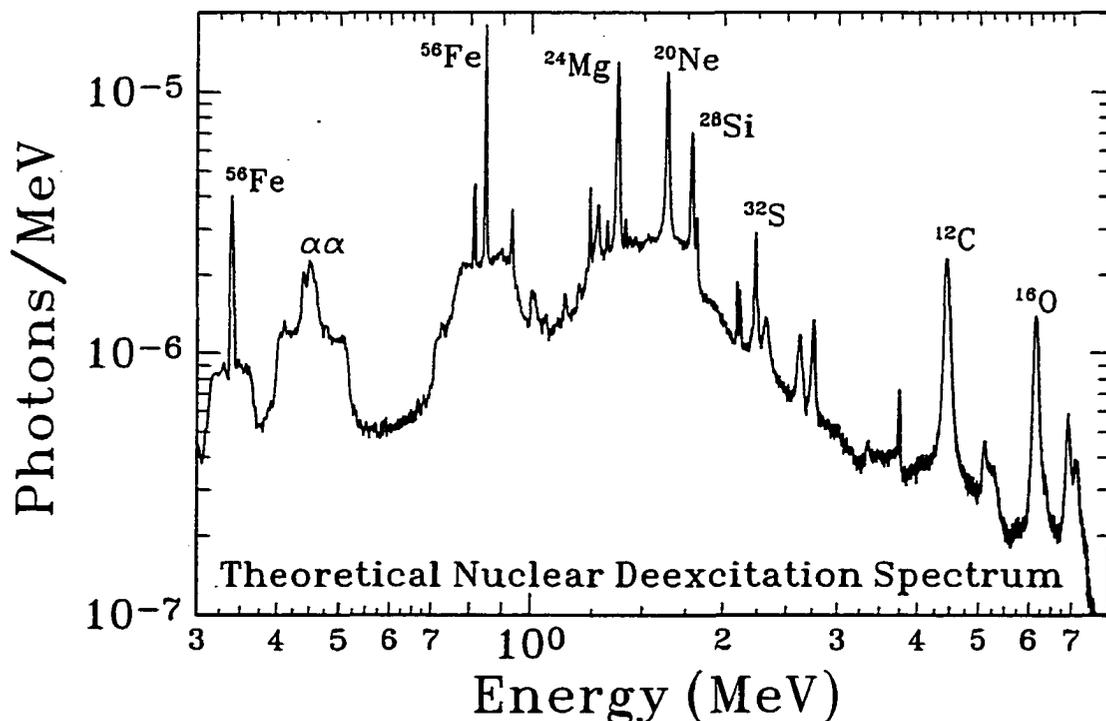
Figure 1.6 - A theoretical nuclear deexcitation spectrum generated using standard solar abundances. It does not include the neutron capture and annihilation lines. (Ramaty et al. 1996)

28

proton/ion spectra are generated predominantly in interactions with heavy nuclei. Major sources for hard spectra are pα and αp reactions. Neutrons with downward initial velocities (towards the photosphere) rapidly thermalize through elastic scattering with protons. This occurs at a column density ~10 g cm^{-2} or a photospheric depth ~100km, unless the neutrons are scattered out of the Sun. Thermal neutrons undergo radiative capture via ^{1}H(n,γ) ^{2}D or non-radiatively via ^{3}He(nap) ^{3}H. The cross-section for ^{3}He(n,p)^{3}H is ~17,000 times greater than that for ^{1}H(n,γ)^{2}D. So, if the ^{3}He abundance were the same as the solar wind (i.e. one ^{3}He per 2500 ^{4}He) the fractions of neutrons captured by hydrogen and ^{3}He would be comparable. There is no direct observation of ^{3}He abundance in the photosphere. Thus, the 2.223 MeV line provides the possibility of probing the composition of the photospheric layers. Theoretical considerations of the fate of a neutron propagating toward the photosphere reveals that it should take about one minute to be captured. Experiments confirm the theoretical predictions. First, the delay between 2.22 and the prompt 4.44 and 6.13 MeV lines is known to exist. Second, limb darkening of the 2.22 MeV line is observed, as predicted by its photospheric origin. The principle interaction of this line with the solar atmosphere is through Compton scattering. The Compton mean free path is comparable to the neutron mean free path at ~10 g cm^{-2}. This limb darkening was observed by studying the ratio of fluences, F (2.22 MeV) to F (4.43 MeV) as a function of heliolongitude for different flares. The width of the 2.2 MeV line depends on photospheric temperatures, but it is always a narrow line.

29

Electron-positron Annihilation Line

Another delayed γ-ray line is the 0.511 MeV annihilation emission. Nuclear reactions produce various radio nuclides (e.g. ^{11}C, ^{12}N, ^{14}O, ^{15}O, ^{19}Ne) that decay by β^+ emission. The initial positron energy lies within a range of several hundred keV to tens of MeV. Only a small fraction of these positrons annihilates at these energies. Most positrons thermalize after which they annihilate with electrons. The delay time is determined by the half-life of the radio nuclides and positron slowing-down time. The average lifetime of the positron emitters ranges from a fraction of a second to 20 minutes. In the initial phase of particle acceleration within a period < 20 minutes the dominant contribution comes from the decay of ^{14}O, ^{15}O, and π^+ mesons. The ^{11}C nucleus become the main positron emitter at a later stage when nuclear reactions stop. Therefore, the corresponding positrons contain information on the post-flare plasma.

The main energy losses for slowing positrons are ionization and Coulomb losses. Relativistic positrons annihilate with a 10% probability. This doesn't contribute noticeably to the 0.511 MeV line due to Doppler broadening. Some positrons escape the Sun. The rest slow down and annihilate with the ambient electrons. Annihilation may occur in flight, creating two 0.511 MeV photons or proceed via a quasi-atomic positronium state.

1. 25% are in a spin zero state (singlet).

2. 75% are in a spin one state (triplet).

30

Singlet state positronium annihilates with a rate of 8×10^9 s^{-1} into two 0.511 MeV γ-rays. The Triplet State (forbidden) annihilates with a rate of 7×10^6 s^{-1} into three γ-rays forming a continuum below 0.511 MeV. The Triplet State can annihilate before collision provided the ambient density is less than 10^{15} cm^{-3} (latter stages of the flare). The width of the 0.511 MeV line and the positronium tail provides temperature and density information.

Pion Decay

If the energies of the accelerated protons and alphas are high enough, pions can be produced due primarily from p+p and p+α reactions. π^o mesons are produced in nuclear reactions by particles with energies greater than a few hundred MeV and $\pi\pm$ have a slightly lower production threshold. π^o decay γ-rays are prompt. π^os have a lifetime $< 10^{-15}$ s, decaying into two γ-rays with center of mass energies of 67.5 MeV each. The photons should appear somewhat later than the prompt nuclear lines because their creation particles must be accelerated too much higher energies than the particles that excite nuclear lines. There should also be a difference in the corresponding γ-ray intensities because the number of accelerating particles falls off with increasing energy. The $\pi^\pm$ particles decay into charged muons that then decay into electrons and positrons. These particles can then produce a secondary bremsstrahlung that can be significant between 8 to 30 MeV (Ramaty et al. 1975; Rank 1996).

31

SEP

Solar Energetic Particles (SEP) were first detected in the form of flare-associated increases in the incident cosmic-ray intensity in the early 1940's (Rieger 1989; Vestrand and Miller 1999). These Ground Level Events (GLE) require >one GeV solar protons and are detected at a rate of a few per solar cycle. After the launch of spacecraft detectors (covering ions with energies up to a few hundred MeV per nucleon and electrons of a few tens of MeV) the rate increased by several orders of magnitude. Of interest to the study of energetic particles in flares is the relationship between interacting charged particles producing gamma rays and those observed in interplanetary space after flares. This allows for testing of the two-phase paradigm that predicts a correlation between γ–ray line events and the interplanetary particle fluence. Coronal

influence and transport effects can be reasonably accounted for by considering magnetically well-connected events. Then peak flux is a reliable indicator of particle fluence (van Hollebeke et al. 1975; van Hollebeke 1979). Correlation studies between SEP events and γ–ray line events with ISEE-3 (Cliver et al.

1989) and Helios (Kallenrode et al. 1987) showed that γ–ray line events produce

large particle fluxes but that the converse was not true. Also shown was that spectra from interplanetary space protons tend to be harder than for interacting particles (Rieger 1989). Analysis of a large number of SEP measurements showed that duration of the soft X-ray flare is an ordering parameter (Bai 1986; Cane et al. 1986), i.e., long duration events are more prolific producers of

32

interplanetary protons than short events. This allows for the division of SEP events into two broad classes (Vestrand and Miller 1999). The first class called impulsive events is associated with GOES 1-8 Å soft X-ray flares with duration up to an hour. These events have enhanced abundances of heavy elements, charge states indicative of 10 MK plasma, enhanced abundance of ^{3}He, high e/p ratios, high interacting to interplanetary proton ratios and broken power law electron spectra that are magnetically well-connected. Gradual events are associated with soft X-ray durations longer than one hour. They have charge states of 1 MK plasma, low ^{3}He/^{4}He ratios, low e/p ratios, interacting to interplanetary proton ratios, and electron spectra fit with a single power-law in rigidity. Gradual events come from uniformly distributed positions on the solar disk and are associated with Coronal Mass Ejections (CME). Impulsive events are associated with soft X-ray loops of small-scale size (< 10,000 km) with closed flux tubes while gradual events are associated with large soft X-ray spatial scales (Pallavicini, Serio et al. 1977). Also, gradual events have a high correlation with Type III radio bursts, which is explained by shocks accelerating protons high in the corona with access to open field lines.

Gamma-Ray Spectroscopy

The thresholds for nuclear-excitation reactions are a few MeV. Neutron and positron production thresholds are tens of MeV. The pion generation threshold is hundreds of MeV. The large differences in reaction thresholds and the shape of the energy dependence of the corresponding cross-sections means that the

33
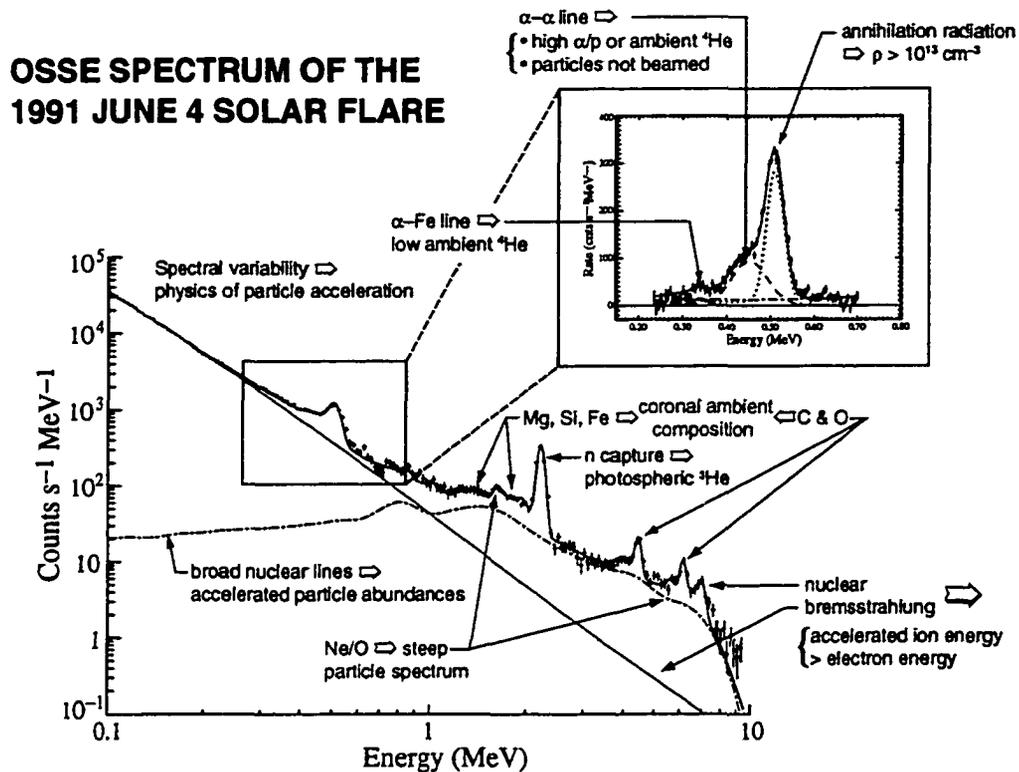
Figure 1.7 - Observed gamma-ray spectrum from the June 4, 1991 X-class solar flare with the OSSE instrument (Murphy et al. 1997).

fluence ratios of different components should depend on actual spectra of accelerated particles and the interaction model. The ratio of the 2.22 MeV line to the prompt lines (e.g. 4.44 MeV) (Ramaty et al. 1975) provides information in the particle spectrum to the range 10-100 MeV and the ratio to π^0 decay γ-rays yields

spectral data for 100-1000 MeV (Ramaty et al. 1987). The flux ratio of the line produced by ^{16}O at 6.13 MeV to the line produced by ^{20}Ne at 1.63 MeV (Ramaty et al. 1996) is sensitive to particle spectral shape. Based on their production energy thresholds, they are sensitive to particle spectral shape in the 2-20 MeV nucleon^{-1} energy range. Another useful ratio is the flux ratio of the 4.44 and 6.13 MeV lines to the 5.3 MeV line produced by spallation reactions on ^{14}C and ^{16}O

34

(Mandzhavidze and Ramaty 2000). Prompt line spectra give information on the composition of accelerated ions and the ambient solar atmosphere. Lines are broadened by 1-2 % when protons or alphas excite nuclei. Lines are broadened by as much as 25% when produced by accelerated heavy nuclei interacting with ambient hydrogen or helium. γ-ray spectroscopy doesn't require knowledge of the ionic states unlike atomic spectra. In addition, cross-sections for nuclear interactions are known with better accuracy than atomic cross-sections. The Figure 1.7, from the OSSE observation and analysis of the 4 June 1991 solar flare, shows the basic information gained from the different parts of a solar flare γ-ray spectrum.

CHAPTER II

INSTRUMENT AND RESPONSE

The Compton Gamma-Ray Observatory

The Compton Gamma-Ray Observatory (CGRO) was a spacecraft launched April 5, 1991 by the space shuttle Atlantis and operated until June 4, 2000 (Gehrels et al. 1993). It was one of NASA's great observatories with four instruments to monitor and image the sky from ~20 keV to 30 GeV. It did so with an unprecedented combination of sensitivity, energy resolution, and spatial resolution. CGRO orbited the Earth in a circle at 450 km with an inclination of

COMPTON OBSERVATORY INSTRUMENTS
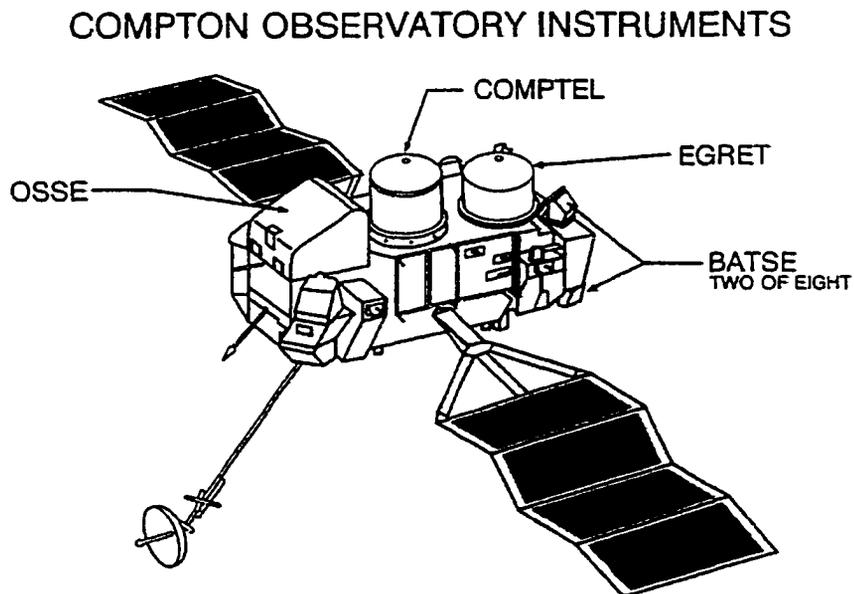
Figure 2.1 - A drawing of the CGRO spacecraft and it's four γ-ray experiments.

36

28.5°. Weighing 17 tons, it was to at the time the most massive spacecraft placed in orbit.

BATSE

The **B**urst **A**nd **T**ransient **S**ource **E**xperiment (Fishman et al. 1989) consists of eight identically configured detectors located on the eight corners of CGRO. BATSE provides continuous monitoring of complete sky. Each detector unit contains a directionally sensitive Large Area Detector (LAD 20 keV – 1.9 MeV) and a Spectroscopy Detector (SPEC 10 keV – 100 MeV) both made of NaI(Tl) with sensitive areas of 2025 cm^2 and 127 cm^2 respectively. The two main objectives of BATSE were to monitor the sky for X-ray and γ-ray transients. In addition, Earth occultations provide monitoring of hard X-ray sources. The typical burst sensitivity and 1-day occultation sensitivity were ~3 x 10^{-8} ergs cm^{-2} and 100 mCrab (30-100 keV) respectively.

OSSE

The **O**riented **S**cintillation **S**pectrometer **E**xperiment (Murphy et al. 1993; Murphy et al. 1997) overlaps the BATSE energy range (50 keV – 10 MeV) but with higher energy resolution and sensitivity. There are four collimated NaI(Tl)-CsI(Na) phoswich detectors with a 3.8° x 11.4° FWHM rectangular field-of-view. The detectors move independent of each other and somewhat of the spacecraft in the X-Z plane of CGRO. The photopeak effective area at 600 keV per detector is ~470 cm^2. OSSE can detect γ–ray lines down to 1x10^{-3} photons cm^{-2} s^{-1} for a

37

1000s exposure. OSSE's main objectives included study of galactic and extra-galactic hard X-ray and low energy γ–ray sources such as black hole candidates, pulsars, and AGNs, as well as transients such as γ–ray bursts and solar flares.

COMPTEL

The **COMP**ton **TEL**escope (Schönfelder et al. 1993) fills the gap between BATSE and OSSE from ~1 MeV to 30 MeV with a 1σ angular resolution between 1° and 2° within a ~1 sr field-of-view. COMPTEL has two independent modes of operation, as an imaging telescope and a spectrometer. The telescope has an energy resolution of 8.8% FWHM at 1.27 MeV with on-axis effective area between 10 and 50 cm^2. It is also sensitive to solar neutrons around 100 MeV. Scientific objectives included studying the galactic and cosmic diffuse emission, MeV blazars, black hole candidates, γ–ray bursts and solar flares.

EGRET

The **Energetic Gamma-Ray Experiment Telescope** (Thompson et al. 1993; Dunphy et al. 1999) is a spark chamber with an energy range from ~20 MeV to ~30 GeV. Its effective area is ~1500 cm^2 in the 200 MeV to 1 GeV range with Gaussian shaped field-of-view with FWHM of ~40°. Away from the Galactic plane, estimated sensitivity for a 2-week exposure was 6×10^{-8} γ cm^{-2} s^{-1} (>100 MeV). EGRET studied blazar AGNs, pulsars, and diffuse galactic emission. In addition to the telescope mode, EGRET has a calorimeter called TASC (Total Absorption Shower Counter). TASC consists of a $76 \times 76 \times 20$ cm^3 NaI crystal.

TASC has a burst/flare mode that records 1 to 200 MeV spectra every 32.57 s

independent of the spark chamber and EGRET veto domes.

COMPTEL

Measurement Principle

COMPTEL uses the dominate photon-matter interaction process in its range of

interest, ~1-30 MeV. This process is COMPTON scattering. A photon of energy

E_γ incident upon the top of the detector is scattered by an electron at rest in the

detector. Energy, ΔE, is transferred from the photon to the electron and the

photon is deflected through an angle ϕ_{geo}, with respect to the original direction of

the photon. The energy dependant distribution of ϕ_{geo} is determined by the

differential Klein-Nishina cross-section.

Conservation of momentum and energy allows one to solve for ϕ_{geo} in

terms of the energy of the photon E_γ and the energy transferred to the electron or

positron (ΔE). This is the well-known Compton scattering formula,

$$\cos(\phi_{geo}) = \left(1 + mc^2\left(\frac{1}{E_\gamma} - \frac{1}{(E_\gamma - \Delta E)}\right)\right) \quad (2.1)$$

where mc^2 is the rest energy of the electron or positron.

If we can measure, E_γ and $E_\gamma - \Delta E$ we can compute ϕ_{geo}. We can determine the

direction of the incident photon if we could measure the direction of the scattered

electron and the direction of the scattered photon.

39

COMPTEL utilizes this detection principle with two detector planes. In the ideal COMPTEL, these detectors would have complete energy absorption, perfect energy resolution and no uncertainly in location measurement. For such a detector a celestial photon incident upon the top plane, detector one (D_1) would Compton scatter through an angle ϕ_{geo} with respect to its incident direction. It would transfer some of its energy ΔE to an electron in the detector. For this ideal case, ΔE is equal to the measured energy deposit in the detector, E_1. The scattered photon is then completely absorbed in the bottom detector (D_2), depositing a measured energy of E_2. The four measured quantities are E_1, E_2, the interaction location in D_1 (x_1, y_1), and the interaction location in D_2 (x_2, y_2). The measured energies $E_1 + E_2$ give us the total energy deposited which for this ideal case is E_γ. The Compton formula is then used to calculate the scatter angle ϕ_{bar}, which for this case is ϕ_{geo}. The intersection of (x_1, y_1) and (x_2, y_2) gives us the scattered gamma ray direction. If we also had the scatter direction of the electron, we could use this with ϕ_{geo} and the scattered gamma ray direction to determine the exact arrival direction of the celestial photon on the sky. COMPTEL is not capable of measuring the electron scatter direction so the incident photon direction lies on the mantel of a cone of half-angle ϕ. If we project this onto sky coordinates (χ, ϕ) we obtain a circle called an event circle. Figure 2.2 shows the geometry of the system.
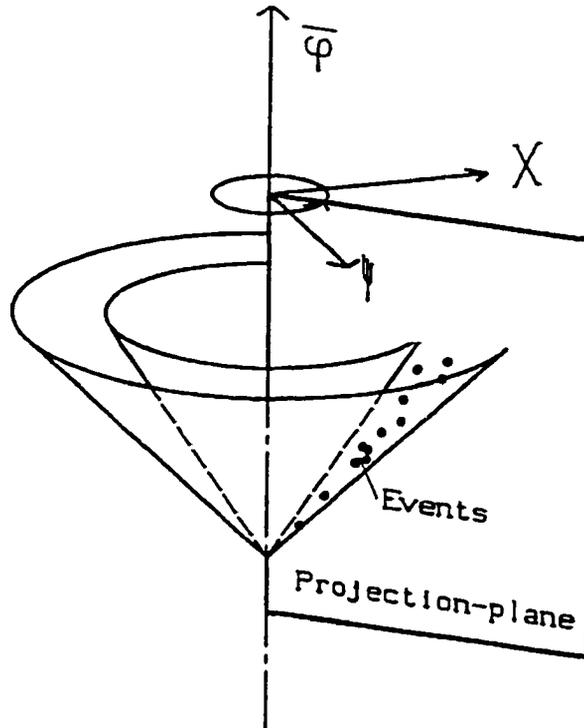
Figure 2.2 - Illustration of the COMPTEL 3 dimensional data space due to a celestial source. Perfect data lie on a cone with semi-angle of 45°.
In reality, the cone mantle is blurred due to measurement errors. (Schönfelder et al. 1993)

In the real COMPTEL, the interaction locations and energy absorption in

D_1 and D_2 suffer from statistical and systematic errors (van Dijk 1996; Kappadath

1998). These errors manifest themselves as uncertainties in (x_1,y_1) and (x_2,y_2).

More importantly, the total energy E_T and the measured angle $\bar{\phi}$ have complex

distributions around E_γ and ϕ_{geo} respectively. Generally, the measured quantities

of energy and angle are $E_T \leq E_\gamma$ and $\bar{\phi} \geq \phi_{geo}$.

Instrument

    D_1 Assembly

41

The D_1 assembly consists of seven cells, each 28-cm in diameter 8.5 cm deep filled with liquid scintillator NE213A. The cells are mounted on a circular aluminum plate 1.45-m in diameter. Each cell is viewed by eight EMI 9755NA photomultiplier tubes (PMTs) that look into cells through fused silica windows. The total geometrical area is 4188 cm². The mass of each D_1 module is 15.3 kg and the total mass of the D_1 assembly is 167.5 kg.

D_2 Assembly

The lower detector assembly (D_2) is comprised of 14 identical detector modules of cylindrical NaI (TI) crystals, 28.2 cm in diameter and 7.5 cm thick. The total geometric area if the 14 crystals is 8744 cm². The bottom housing of each module has seven 7.6-cm diameter openings with seven 12-mm thick quartz-glass windows glued to EMI9754NA PMTs. Each D_2 module is mounted below a support sandwich of density 0.9-g cm⁻². A single module is 28.2 kg and the entire assembly is 429.1 kg.

Veto-Domes

The anticoincidence subsystem is four veto-dome assemblies. The main part of each assembly is a Cassini-shaped dome of a 1.5-cm thick plastic scintillator (NE110) with a cylindrical extension at the open end. Each detector plane (D_1 and D_2) is surrounded by two of these domes. The larger top dome overlaps a smaller bottom dome. Twenty-four PMTs view each of the four veto-domes. On top of each veto dome is a light-emitting diode used for in-flight

42

testing. The mass of the large dome is 114.2 kg and the small is 73.9 kg. The entire anticoincidence subsystem has a mass of 376.2 kg.

Calibration Units

A calibration system is necessary to maintain the energy, angular, and positional resolution of COMPTEL. Thus, it is necessary to monitor and adjust the energy response of the D_1 and D_2 modules. For this task of monitoring the gains in the system, COMPTEL has two tagged, γ-ray calibration sources (CALs). These CAL events are tagged.
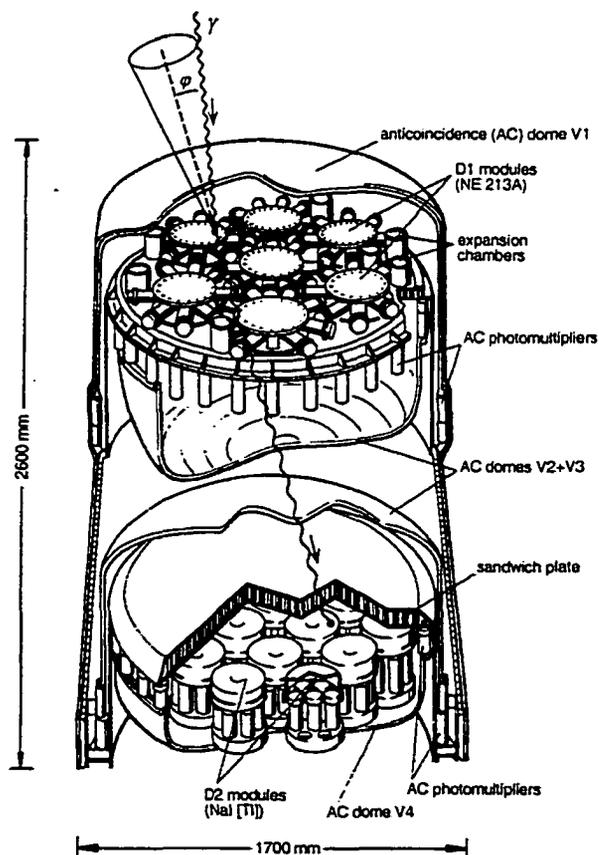
Figure 2.3 - The COMPTEL instrument assembly. (Schönfelder et al. 1993)

43

The calibration system consists of two ^{60}Co doped scintillators, each viewed by two 1.25 cm PMTs. These units are placed midway between D_1 and D_2, out of the γ-ray light path. The source strengths were chosen so that enough events in each cell are produced to monitor the gain over minute timescales.

TOF

The time of flight (TOF) between D_1 and D_2 is measured with a digital accuracy of 0.25 ns. An event consisting of first an interaction in D_2 then in D_1 (back-scattered event) is clearly separated from forward-scattered events. The forward and back-scattered TOF peaks (with a resolution of 1ns) are separated by about 11σ. There is a dependence of the TOF peak position on energy that is significant at low energies. High-energy neutrons that show up in the forward-scattered TOF peak can be effectively rejected using the PSD information from the D_1 modules. These corrections in TOF and PSD are made in ground data processing.

Energy Resolution

The D_1 detector modules were designed to maximize the probability of a single Compton scatter. Studies have shown that less than 3% of events in D_1 involve multiple scatters (Schönfelder et al. 1993). The energy response of D_1 is relatively simple and can be well represented by a Gaussian photopeak with energy resolution of $\sigma(E_{MeV}) = 0.056\ E^{-0.57}$ MeV.

The energy response of D_2 is more complicated than D_1 due to its multiple energy loss processes. Typical energy losses include pair production,

44

photoelectric absorption and multiple Compton scattering. From fitting combined calibration energy spectra of the 14 D_2 modules, the energy resolution can be represented by a function of the form:

$$\sigma(E_{MeV}) = 10^{-2}\left(9.86E_{MeV} + 4.143E_{MeV}^2\right)^{1/2} MeV. \quad (2.2)$$

In flight calibration including corrections to the 2.223 MeV line (Weidenspointner, 1994) have led to a corrected energy resolution of the form:

$$\sigma(E_{MeV}) = 10^{-2}\left(9.86E_{MeV} + 0.013E_{MeV}^2\right)^{1/2} MeV. \quad (2.3)$$

The energy response of the COMPTEL telescope describes the distribution of the measure total energy $E_T = E_1 + E_2$. This total energy response is a convolution of the energy responses of D_1 and D_2 along with the energy losses that occur between the detector planes. The characteristic response of COMPTEL is a photopeak from photons suffering negligible energy loss and a tail extending to lower energies that mainly consists of photons that were not completely absorbed in D_2. Empirical data and Monte Carlo simulations were used to determine the energy resolution described by a Gaussian photopeak with width $\sigma(E_{MeV})$ (Schönfelder et al. 1993),

$$\sigma(E_{MeV}) = 10^{-2}\left(14.61E_{MeV} + 2.53E_{MeV}^2\right)^{1/2} MeV. \quad (2.4)$$

Figure 2.4 shows a total energy loss for a Monte Carlo simulation of a 4.4 MeV line.

45
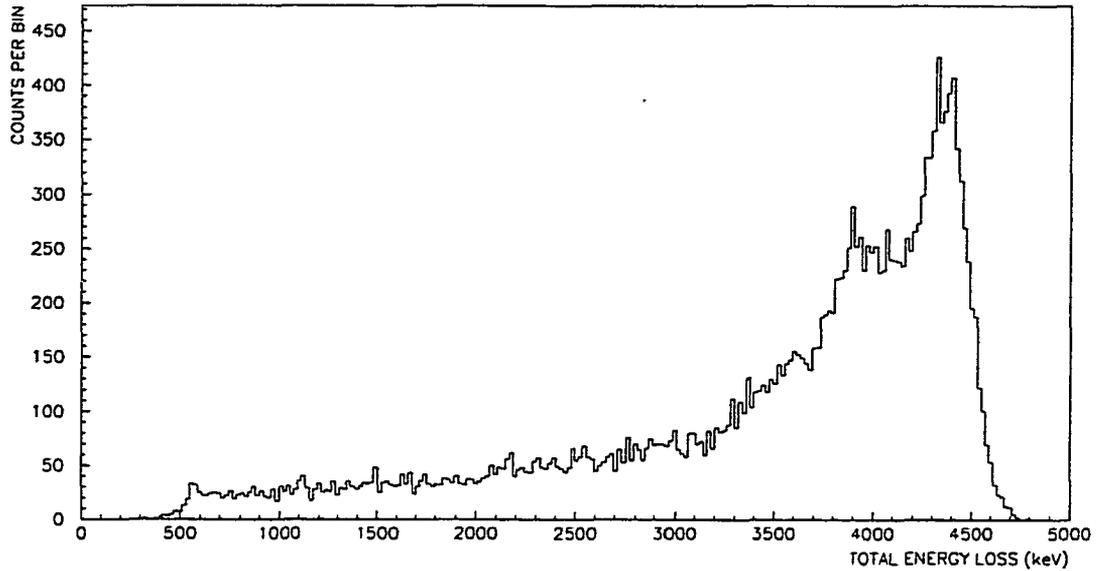
Figure 2.4 - Simulated energy loss spectrum for a 4.4 MeV line. [28]

Angular Resolution Measure

The Angular Resolution Measure (ARM) of an event is defined as the difference between the geometrical scatter angle phigeo and the measured angle $\bar{\phi}$, ARM = $\bar{\phi}$-ϕ_{geo}. Figure 2.5 shows the ARM distribution for a simulated point source. The Gaussian peak at ARM=0° in this distribution corresponds to the photopeak in the E_T distribution. Events with large positive ARM values suffer from energy loss in D_2 and the small fraction to the left of ARM=0° suffer from energy losses in D_1. The telescope angular resolution determined from calibrations and simulations is represented by

$$\sigma(E_{MeV}) = \frac{1.247}{1-\exp\left(-0.854 E_{MeV}^{0.9396}\right)} . \quad (2.5)$$

46
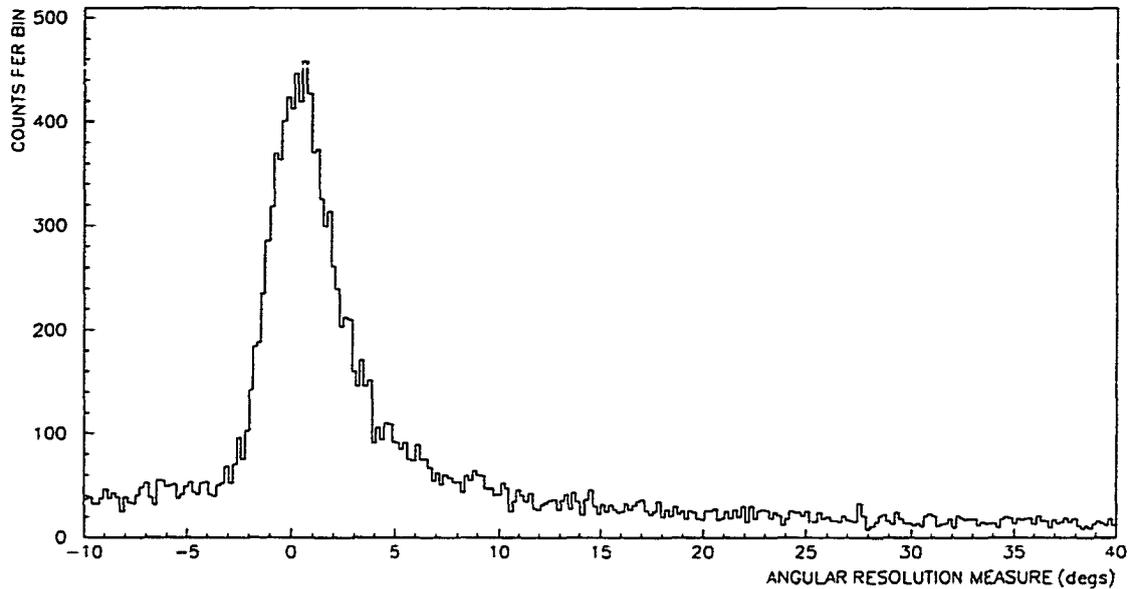
Figure 2.5 - Simulated ARM spectrum for a 4.4 MeV line.

Event Selections and Effective Area

A gamma ray event is identified by a delayed coincidence between the D_1 and D_2 detectors, along with the requirement there is not a coincident signal from any of the four veto domes. For each event the following quantities are measured:

1. The energy loss E_1 in D_1.

2. The interaction location in D_1.

3. The scintillation pulse shape in D_1.

4. The energy loss E_2 in D_2.

5. The interaction location in D_2.

6. The time-of-flight of the scattered gamma ray from D_1 to D_2.

7. The time of the event.

47

Although the effective detection area of a Compton telescope is small, the telescope is sensitive because source gamma rays are distinguished from background events by the multiparameter signature of each event. Figure 2.6 is a
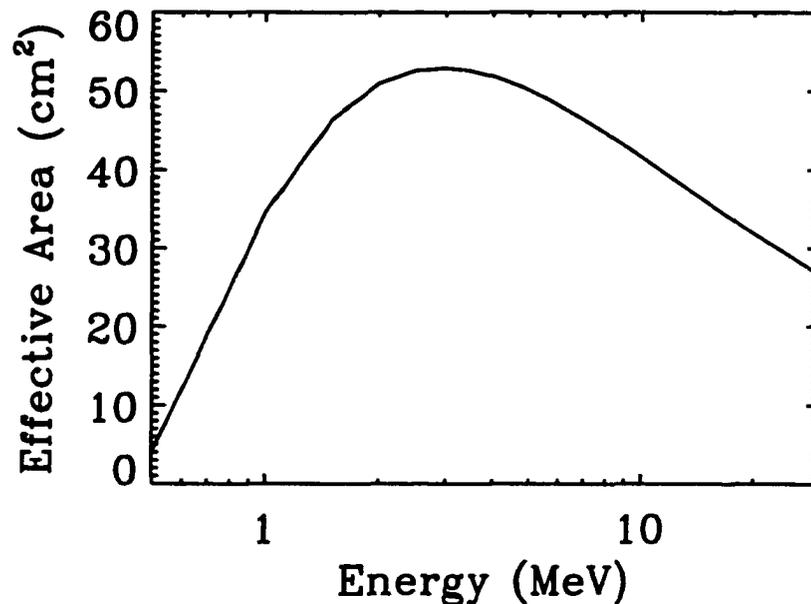
Figure 2.6 - An analytic fit of the calibration and simulated effective area at normal incidence to COMPTEL with no data selections. (Schönfelder et al 1993)

plot of a functional form of COMPTEL's effective area. The standard selection set of event parameters that is used to optimize the signal-to-noise ratio is (van Dijk 96; Rank 96):

- 70 keV < E_1 < 20 MeV

- 650 keV < E_2 < 30 MeV

- 0° < phibar < 36°

- 115 channels < TOF < 130 channels

- 0 channels < PSD < 110 channels

48

- $\zeta > 5°$ (angular distance between the Earth and the event circle)

The upper bounds on deposited energy reflect lack of instrument response knowledge above these energies in D_1. The lower boundary is such to exclude the individual thresholds for the D_1 and D_2 modules. The instrumental background is greatly reduced by these TOF selections. The PSD selections are to reject neutron-induced events generally found above channel 90. The lower boundary on ζ insures the rejection of Earth albedo events.

Livetime Corrections

Almost all detector systems have a minimum time separation needed to distinguish between two different events (Knoll 1989) and COMPTEL is no exception (van Dijk 1996). This minimum time that is due to both the detector and the system electronics is called dead time. If events occur too quickly, data losses due to dead time can be severe. For COMPTEL, we generally discuss the time in which events are accepted so we discuss live time, the inverse if dead time. There are several instrument parameters, mostly contained in the housekeeping data (HKD), which go into the calculation of live time corrections. The parameters and their use in livetime calculations were discussed in detail by van Dyke (1996) and Rank (1996). Usually live times are high, ranging from 94% to 98% with an average of 96.5% (van Dijk 1996). This however is not the case during solar flares. Live times can be as low as ~1% during large solar flares. During a large solar flare, the soft X-ray flux is intense and saturates the plastic domes of the veto system. This causes a nearly constant anti-coincidence signal

49

so most real events are rejected. In addition, a problem during large solar flares is losses due to telemetry limitations. The maximum telemetry rate is 48 events per packet (a packet is 2.048 s and a super-packet is eight packets) or about 24 per second. During the large flares of June 1991 a combination of these effects created dead times of ever 99%. Despite these large dead time losses corrections using the parameters mentioned above where successful, being tested against the data from the high range burst module (HRBM) (Rank 1996). Figure 2.7 shows the live time during the 11 June 1991 X12 flare along with the uncorrected and corrected time profiles.
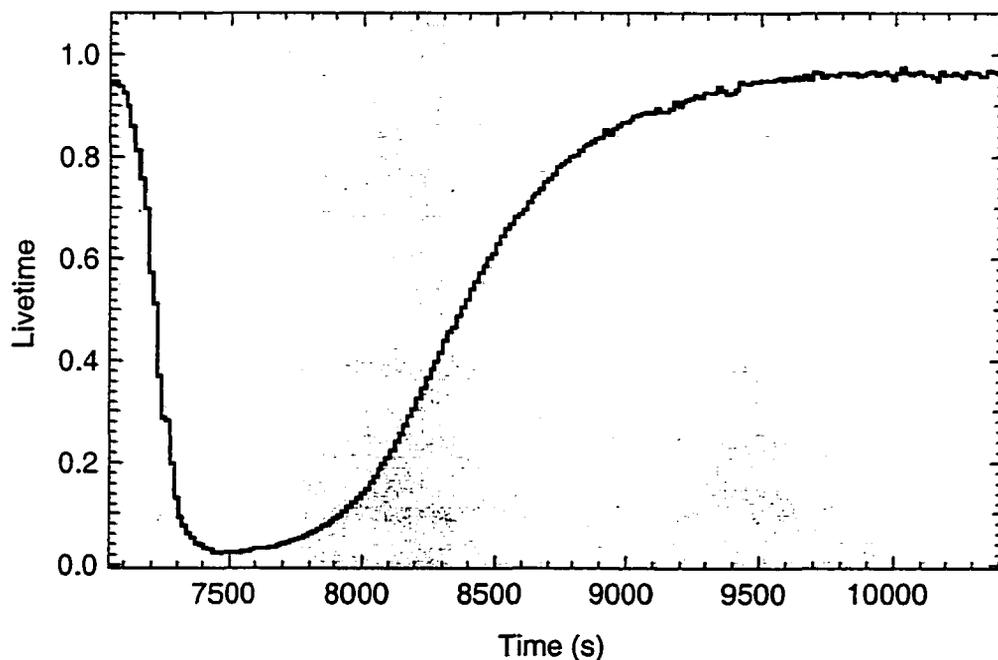
Figure 2.7 - Livetime of the COMPTEL telescope during the X-class flare of 11 June 1991.

50

The Burst Spectroscopy Mode

Two of COMPTEL's 14 D_2 modules are used to accumulate burst spectra upon receipt of an external trigger from BATSE. The modules would have a 4π sr fov except for obscuring intervening material. For zenith angles (measured from the CGRO z-axis) $0°<\Theta<45°$ the D_2 modules are obstructed by the D_1 detectors, veto domes V1-V3 and the D_2 support plate assembly. For angles $\Theta>45°$ the D_2 modules are obstructed by the other CGRO instruments and the electronics. (See (Morris and Xu 1983) for more details the mass distribution obstructing D_2.) Module D_2-14 (low range - LRBM) covers the energy range of ~50 keV to 1.1 MeV and module D_2-7 (high range - HRBM) covers the energy range ~160 keV to 11 MeV, both with 128 channels. These modules are equipped with a dedicated analog-to-digital converter and electronics subsystem (BSA) described in Winkler et al. (1986). The electronics accumulate and make histograms of the burst data over the 128 channels per module integrating over a selectable time interval (the maximum number of counts per histogram is 65,535).

The BSA operates in four modes (shown in Figure 2.8). The background mode is the normal mode of operation. Spectra from the burst modules are accumulated over a period ranging from 2 to 512s per spectrum and then read out continuously or at a reduced rate. These data are used to investigate background before and after the burst. The BSA switches to burst mode upon receipt of a trigger from BATSE. Six burst-mode spectra are accumulated with an integration time from 0.1 to 25.6s. The BSA then switches to tail mode,

51

accumulating 255 spectra with individual integration times of 2-512s. All integration and readout rates are telecommandable. After the last tail mode spectra are recorded, background mode is re-entered.
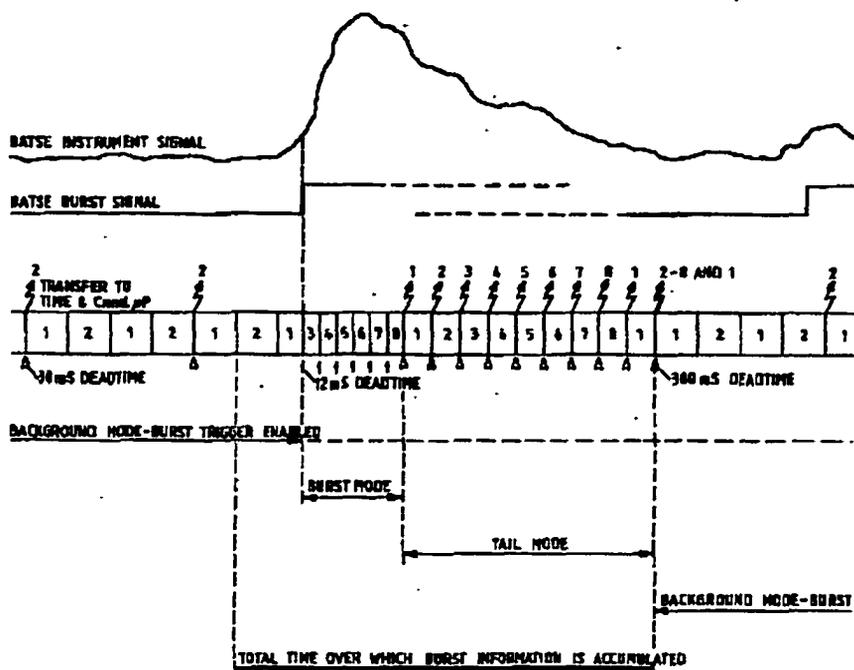
Figure 2.8 - Sequence of COMPTEL's burst mode subsystem.
(Schönfelder et al 1993)

CHAPTER III

NEUTRON TRANSPORT

The 2.223 MeV gamma-ray line in solar flares is produced by neutron capture on hydrogen. Elastic scattering primarily off hydrogen moderates high-energy neutrons in the solar atmosphere. When they reach thermal energies they are captured by hydrogen to produce deuterium with the 2.223 MeV line emission or by ^{3}He that produces no emission. To understand the dynamics of the 2.223 MeV neutron capture line, we must study the dynamics of neutron transport and capture in hydrogen. The study of neutron transport and neutron capture in the solar atmosphere generally requires the use of complex Monte Carlo simulations. This is because neutrons can undergo many nuclear reactions with the ambient solar material. In addition the stratified and spherical geometry of the system must be included. For lower energy neutrons (<10 MeV) inelastic scattering cross sections are small. This means the only important reactions are those of elastic neutron scattering off hydrogen and helium, radiative capture with hydrogen, and non-radiative capture with ^{3}He. This comparatively simple scenario allows for the neutron transport to be modeled analytically (Young and Ryan 1997).

The neutron transport equation in its most general form cannot be solved analytically in any obvious way. Many approximations have been developed to

53

obtain analytic solutions for different applications. Most of these analytical solutions assume that low-order Legendre polynomial expansions yield adequate representations of the neutron distribution function and the elastic scattering kernel. They also assume that the average energy loss of a neutron in a collision is small. These assumptions for a hydrogen medium are not valid. A neutron can lose all its energy in one collision with hydrogen and the scattering is more forward directed. Therefore, the full neutron transport equation must be solved (Weinberg and Wigner 1958; Williams 1966).

We are interested in two regimes of neutron energies, neutrons between about 1 eV to 10 MeV (moderating region) and neutrons with energies equivalent to the thermal ambient background (~0.5 eV for the solar photosphere) (thermalization region). First, we address the neutrons from a few eV to a few MeV in what we call the slowing down or moderating region. The kinematics of slowing down is described first, in particular we elaborate on some of the special properties of elastic scattering in hydrogen. Then we discuss the general transport equation (Boltzmann equation). Though in most cases the Boltzmann equation cannot be solved exactly, we will now discuss a few special cases where closed form analytical solutions exist and provide some useful insight to the general problem.

54

Slowing Down

Kinematics

The slowing down region allows us to make a few approximations in treating the neutron scattering. We treat the scattering as classical elastic "billiard ball" scattering, neglect chemical binding and thermal motion, and treat the nucleus as being at rest, ignoring recoil. We also neglect inelastic scattering in the center-of-mass frame. Elastic scattering is the primary source of energy loss for neutrons during moderation. In the non-relativistic regime the scattering is isotropic in the center-of-mass frame (Beckurts and Wirtz 1964).

In the laboratory frame we start with a neutron of mass m, travelling with speed v. It is incident upon a nucleus of mass mA at rest (Figure 3.1).

(BEFORE)   (AFTER)
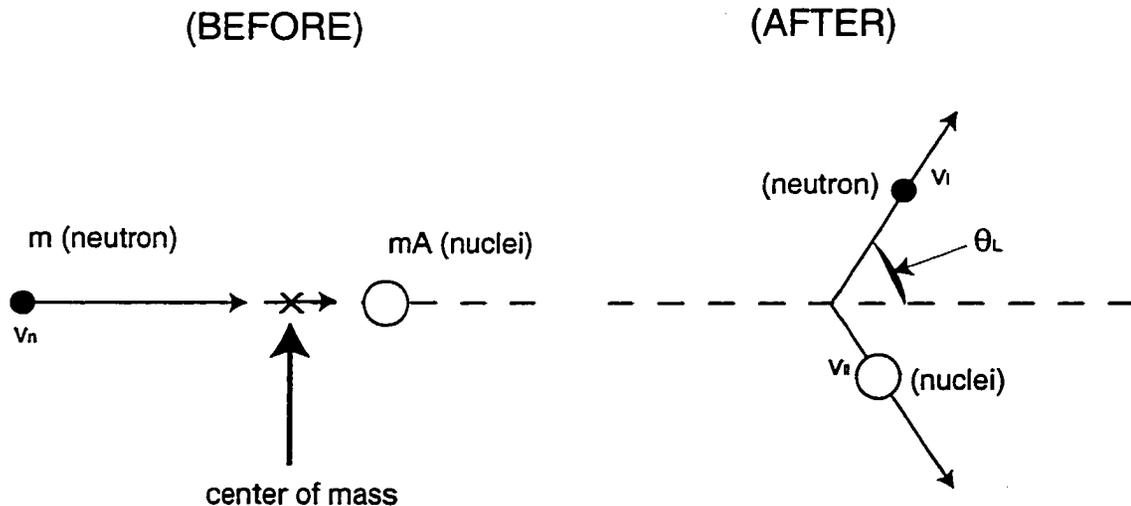
Figure 3.1 - Kinematics of elastic scattering of a neutron with a nucleus in the laboratory frame.

The center of mass is travelling in the same direction as the neutron with speed $v_{cm} = mv_n/M+m = v_n/A+1$. If we transform to the center of mass system, the

55

neutron has speed V_n-V_{cm} and the nucleus has a speed $-V_{cm}$. This collision is elastic so energy and momentum are conserved (Figure 3.2).

(BEFORE)   (AFTER)
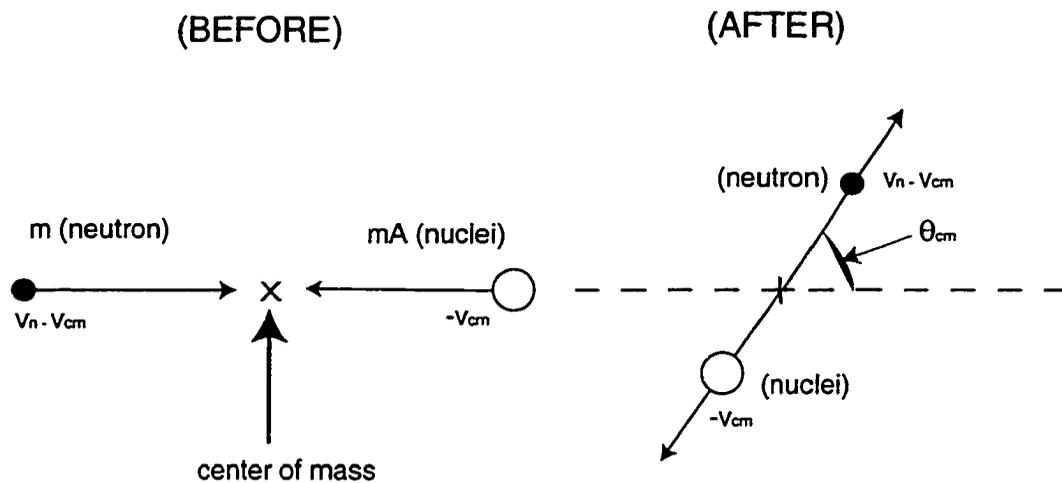
Figure 3.2 - Kinematics of elastic scattering of a neutron with a nucleus in the center of mass frame.

Vectorially, $\mathbf{v} = (\mathbf{v}_n - \mathbf{v}_{cm}) + \mathbf{v}_{cm}$ as shown is Figure 3.3.
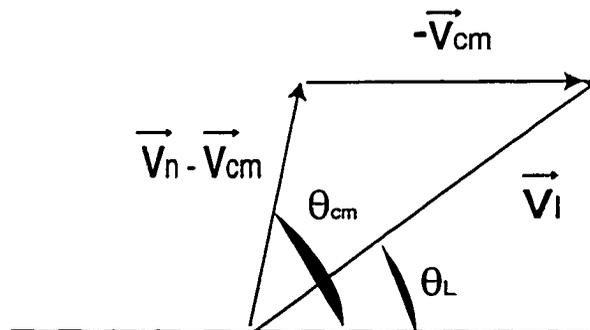
Figure 3.3 - Vector diagram relating the laboratory and center-of-mass frames for neutron-nucleus elastic scattering.

From this we can solve for $v_1{}^2$ in terms of $v_n{}^2$, A, and $\mu_{cm} = \cos\theta_{cm}$.

$$v_1{}^2 = v_n{}^2 \frac{\left[1 + 2A\mu_{cm} + A^2\right]}{\left[1 + A\right]^2} \quad (3.1)$$

56

We can also write the relationship between the center of mass and laboratory angles as $(v_n - v_{cm})\mu_{cm} + v_{cm} = v_1\mu_L$ where $\mu_L = \cos\theta_L$. Using equation 3.1 and the fact that $v_{cm} = v_n/(1+A)$ we obtain the relation

$$\mu_L = \frac{A\mu_{cm} + 1}{\left(A^2 + 2A\mu_{cm} + 1\right)^{1/2}} \quad (3.2)$$

This problem is nonrelativistic so we can write v_1^2/v_n^2 as E'/E. If the parameter

$$\alpha \equiv \left(\frac{A-1}{A+1}\right)^2 \quad (3.3)$$

is introduced (Beckurts and Wirtz 1964) equation 4.1 becomes

$$\frac{E'}{E} = \frac{1}{2}\left[(1+\alpha) + (1-\alpha)\mu_{cm}\right] \quad (3.4)$$

The minimum and maximum of μ_{cm} are -1 and 1, so the range of E'/E can be written as

$$\alpha E' \leq E \leq E' \quad (3.5)$$

Equation 3.5 corresponds to the energy range of the scattered neutron. The case for hydrogen is special. The energy loss range for a neutron scattered off hydrogen is $0 < E < E'$. This shows that hydrogen is the most efficient moderator material and has the distinction of being the only moderator in which a scattered neutron can lose all of its energy in one collision. This will be an important consideration neutron transport problems.

For energies in the slowing down regime (few eV to ~10MeV) neutron scattering is s-wave scattering and is isotropic in the center-of-mass frame (Beckurts and

57

Wirtz 1964). The probability that a neutron of energy E before a collision acquires an energy in the range E' to $E'+dE'$ is $P(E\text{->}E')dE'$. We know from equation 3.4 that the energy E' is uniquely connected to μ_{cm} where $P(E\text{->}E')dE' = g(\mu_{cm})d\mu_{cm}$ is the probability μ_{cm} lies between μ_{cm} and $\mu_{cm}+d\mu_{cm}$. This can be found by calculating the probability of scattering into a solid angle $d\omega$, $d\omega = dA/4\pi$. For an isotropic system $d\omega = 2\pi\sin\theta_{cm}d\theta_{cm}/4\pi$ or $d\omega = 1/2\ d\mu_{cm}$ so $g(\mu_{cm}) = 1/2$ (Beckurts and Wirtz 1964). Using this result and equation and equation 3.4,

$$P(E \rightarrow E') = \frac{1}{2}\frac{d\mu_{cm}}{dE} = \frac{1}{(1-\alpha)E}\ (3.6)$$

Now the average angular distribution in the laboratory frame can be evaluated by averaging μ_L over $+1$ to -1 giving $<\mu_L> = 2/3A$. For a light moderator the forward direction is preferred but the scattering becomes more isotropic for heavy moderators, $2/3A \rightarrow 0$.

Also of interest is the average energy loss per collision, $\overline{\Delta E} = \frac{E}{2}(1-\alpha)$. This depends on energy and A but the fractional energy loss depends only on A,

$\frac{\overline{\Delta E}}{E} = \frac{1}{2}(1-\alpha)$ (Beckurts and Wirtz 1964). For hydrogen, the fractional energy loss per collision is 1/2. Logarithmic energy loss intervals during moderation are equally spaced. This motivates the introduction of a new variable called lethargy,

$$u \equiv \log\left(\frac{E_0}{E}\right)\ (3.7)$$

58

where E_0 is the source energy of a neutron at energy E (Beckurts and Wirtz 1964). The average logarithmic energy loss (Beckurts and Wirtz 1964) is

$$\xi = \log\left(\overline{\frac{E_0}{E}}\right) = 1 + \frac{\alpha}{1-\alpha}\log\alpha. \quad (3.8)$$

The quantity ξ is approximately $\dfrac{2}{(A+2/3)}$ for large A and it is unity for hydrogen.

The quantity ξ can be used to estimate the average number of scatters, n, to moderate a neutron with source energy E_0 to energy E,

$$n\xi = \log\left(\frac{E_0}{E}\right) \text{ or } n = \frac{\log\left(\frac{E_0}{E}\right)}{\xi} = \frac{u}{\xi}.$$

Table 3.1 contains A, α, ξ, n, density and fractional energy loss for ions in the solar photosphere for moderation from 10 MeV to 1/2 eV (corresponding to 6000 K).

Nuclei	Density	A	α	ξ	n	$\Delta E/E$
^{1}H	10^{17}	1	0	1	14.5	0.5
^{4}He	$8.5 \cdot 10^{15}$	4	0.36	0.425	34	0.32
^{3}He	$5 \cdot 10^{12}$	3	0.25	0.5379	27	0.375
C	$3.3 \cdot 10^{13}$	12	0.716	0.158	92	0.142
N	$9.1 \cdot 10^{12}$	14	0.751	0.1364	106	0.1245
O	$6.6 \cdot 10^{13}$	16	0.778	0.12	121	0.111
Ne	$8.3 \cdot 10^{12}$	20	0.9025	0.0504	287	0.049

Table 3.1 - The moderation of neutrons from 10 MeV to 1/2 eV (6000 K) in several moderators with their density in the solar photosphere. The calculated moderation parameters are α, ξ, n, and $\Delta E/E$.

59

The Transport Equation

The differential neutron density $n(r,\Omega,E,t)dVd\Omega dE$ is the number of neutrons in the volume element dV whose flight direction is characterized by the unit vector Ω, lying in the differential solid angle $d\Omega$ around Ω, with position vector r, and with kinetic energy between E and $E+dE$. The quantity $n(r,\Omega,E,t)$ has units of cm^{-3} sr^{-1} ev^{-1} and is thus the number density of neutrons with energies in a unit interval around E and flight directions in a unit solid angle around Ω. The differential neutron flux is defined by $F(r,\Omega,E,t)$ $d\Omega dE = v$ $n(r,\Omega,E,t)d\Omega dE$ where $v = \sqrt{2E/m}$ is the non-relativistic neutron velocity.

The description of neutron behavior in energy, time, and space is described by neutron balance (Beckurts and Wirtz 1964; Williams 1966).

1. Leakage out of the volume V:

$$\bar{\nabla} \cdot (\hat{\Omega}F(\vec{r},\hat{\Omega},E,t))dVd\Omega dE = \hat{\Omega} \cdot \bar{\nabla}F(\vec{r},\hat{\Omega},E,t)dVd\Omega dE \quad (3.9)$$

2. Loss due to absorption and scattering into other directions:

$$\Sigma_t(E)F(\vec{r},\hat{\Omega},E,t)dVd\Omega dE; \Sigma_t = \Sigma_a + \Sigma_s \quad (3.10)$$

3. In scattering of neutrons from other directions:

$$\int_{4\pi}\int_0^{\infty} \Sigma_s(\hat{\Omega}' \rightarrow \hat{\Omega}, E' \rightarrow E)F(\vec{r},\hat{\Omega}',E',t)d\Omega'dE'd\Omega dE \quad (3.11)$$

4. The production of neutrons in volume dV by a source density S:

$$S(\vec{r},\hat{\Omega},E,t)dVd\Omega dE \quad (3.12)$$

The sum of all these terms gives the time rate of change of the differential neutron density that is an integro-differential equation in seven variables called the transport or Boltzmann equation,

$$\frac{1}{v}\frac{\partial F(\vec{r},\hat{\Omega},E,t)}{\partial t} = -\hat{\Omega}\cdot\vec{\nabla}F(\vec{r},\hat{\Omega},E,t) - \Sigma_t(E)F(\vec{r},\hat{\Omega},E,t)$$
$$+\iint \Sigma_s(\hat{\Omega}' \to \hat{\Omega},E' \to E)F(\vec{r},\hat{\Omega}',E',t)d\Omega'dE' + S(\vec{r},\hat{\Omega},E) \quad , (3.13)$$

With this equation, the appropriate boundary conditions are necessary to solve for the vector flux intensity arising from a source distribution. Two particular boundary conditions are important. At the interface G between a medium A and medium B continuity demands that for all r_G, Ω, and E,

$F_A(\vec{r}_G,\hat{\Omega},E) = F_B(\vec{r}_G,\hat{\Omega},E)$. At the interface between the scattering medium and a vacuum or totally absorbing medium for all inward directed neutrons the flux at the boundary must be zero, i.e., $F(\vec{r}_G,\hat{\Omega},E) = 0$.

Steady State and Time-dependent Solutions

The first problems we solve are the time-dependent and steady state solutions for an infinite homogeneous medium, i.e., one with no spatial gradients or no net neutron current. It is convenient to work in terms of lethargy instead of energy. Using the relation for the angular flux in lethargy,

$$\phi(u,\hat{r},\hat{\Omega},t) = \phi(E,\hat{r},\hat{\Omega},t)\left|\frac{dE}{du}\right| \quad (3.14)$$

and integrating over all directions, we obtain the lethargy Boltzmann equation,

61

$$\frac{1}{v}\frac{\partial\Phi(u,t)}{\partial t}+\Sigma(u)\Phi(u,t)=\int_{u-q}^{u}du'\,\Sigma_s(u')f_0(u-u')\Phi(u',t)+S(u,t)\ (3.15)$$

where $q=\log(1/\alpha)$ and $\Sigma(u)=\Sigma_s(u)+\Sigma_a(u)$. We treat the scattering as isotropic

in the CM frame so equation 4.11 in lethargy gives $f_0(u-u')=e^{u'-u}/(1-\alpha)$ (the

isotropic scattering kernel) (Beckurts and Wirtz 1964). The Boltzmann

equation is then

$$\frac{1}{v}\frac{\partial\Phi(u,t)}{\partial t}+\Sigma(u)\Phi(u,t)=\frac{1}{(\alpha-1)}\int_{u-q}^{u}du'\,\Sigma_s(u')e^{u'-u}\Phi(u',t)+S(u,t).\ (3.16)$$

Finding a solution is aided by using the slowing down density, $q(u,t)$, which is

defined as the number of neutrons in unit time and volume that pass from a

lethargy less that u to a lethargy greater than u, minus the number which

cross u in the opposite direction. In the slowing down region there is no up

scattering so $q(u,t)$ is written as

$$q(u,t)=\int_{u-q}^{u}du'\int_{u}^{u'+q}du''\Sigma_s(u')f_0(u''-u')\phi(u',t)\ (3.17)$$

or for isotropic scattering,

$$q(u,t)=\frac{1}{1-\alpha}\int_{u-q}^{u}du'\Sigma_s(u')\left[e^{u'-u}-\alpha\right]\phi(u',t)$$

Slowing Down with Hydrogen
For hydrogen $A=1$, $\alpha=0$ and $q=\infty$ so the slowing down density is

$$q(u)=\int_{-\infty}^{u}du'\Sigma_s(u')\left[e^{u'-u}\right]\phi(u').\ (3.18)$$

62

It is helpful to work with a new variable called the collision density (Beckurts and Wirtz 1964), $\Phi(u)=\Sigma(u)\phi(u)$. A differential equation for $\Phi(u)$ is obtained by differentiating $q(u)$ with respect to u and using the relation $\Phi(u) = q(u) + S(u)$. Combining these equations to eliminate $q(u)$ yields the equation

$$\frac{d\Phi(u)}{du} + (1-c(u))\Phi(u) = S(u) + \frac{dS(u)}{du} \quad (3.19)$$

where $c(u) = \frac{\Sigma_s(u)}{\Sigma(u)}$. Integrating where $S(u) = 0$ for $u < 0$ gives the exact solution

$$\Phi(u) = S(u) + \int_0^{u'} S(u')c(u')\exp\left[\left(-\int_{u'}^u (1-c(u'''))du''\right)du'\right]. \quad (3.20)$$

For the situation of constant scattering, $1/v$ absorption (capture), and a delta function source, integration of equation 3.20 gives the solution (Williams 1966)

$$\phi(u) = \frac{Q}{v_0\Sigma_s^2} \frac{v^3\left(v_0\Sigma_s + \Sigma_a(v)v\right)}{\left[v + \Sigma_a(v)v/\Sigma_s\right]^3}. \quad (3.21)$$

For zero absorption the collision density is constant and $\phi(u)=Q/\Sigma_s(u)$. This corresponds to a $1/E$ slowing down distribution, $\phi(E)=Q/(E\Sigma_s(E))$.

The next solution of interest is the time-dependent solution for a source function of $S(u,t) = Q\delta(u)\delta(t)$. This solution can be used as a Green function to find the flux due to an arbitrary neutron source, i.e.,

$$\phi(u,t) = \int_0^t dt' S(u,t')\phi(u,t-t'). \quad (3.22)$$

63

Taking the Laplace transform of the Boltzmann equation with respect to time we obtain the fortunate result that the Laplace transform is of the same form as the steady state solution with $\Sigma_a(u)v$ replaced by the Laplace variable s. If we then take the inverse Laplace transform by evaluating the residue we obtain,

$$\phi(v,t) = Q(\Sigma_s vt)^2 \left[1 - \frac{v}{v_0} + \frac{2}{\Sigma_s v_0 t} \right] e^{-v\Sigma_s t}, \quad (3.23)$$

using the fact that $\phi(v,t) = \frac{2}{v}\phi(u,t)$. In the limit that the source energy is infinite the solution reduces to a function of the dimensionless variable $\Sigma_s vt$,

$$\phi(v,t) = Q(\Sigma_s vt)^2 e^{-v\Sigma_s t} \quad . \quad (3.24)$$

The last case of interest here is that of arbitrary $\Sigma_a(u)$ and $\Sigma_s(u)$ but the only case for which Laplace inversion is possible is when they both vary as $1/v$ (Sneddon 1951; Williams 1966). This solution is constructed by subtracting the direct contribution of the delta function. By setting $\overline{\phi}(u,s) = \overline{\chi}(u,s) + \beta\delta(u)$, substituting this into the Laplace transformed equation and collecting terms not directly connected to the delta function we obtain,

$$\left[\frac{s}{v} + \Sigma(u) \right] \overline{\chi}(u,s) = \int_{-\infty}^{u} du' \Sigma_s(u')\overline{\chi}(u',s)e^{u'-u} + \beta e^{-u}, u \neq 0 \text{ and}$$

$$\left[\frac{s}{v_0} + \Sigma(0) \right] \beta = Q, u = 0. \quad (3.25)$$

64

Differentiating the equation for $u \neq 0$ and using the boundary condition that the flux vanishes for lethargy less than zero, $\overline{\chi}(0,s) = Q \left/ \left[\dfrac{s}{v_0} + \Sigma(0) \right]^2 \right.$ a first order equation with variable coefficients is obtained.

$$\overline{\chi}(u,s) = \frac{Qvv_0}{\left[s + v_0 \Sigma(0)\right]^2} \exp\left\{ -\frac{s + \Sigma_a(0)v_0}{s + \Sigma(0)v_0} u \right\}. \quad (3.26)$$

Substituting $\Sigma_a(u) = \Sigma_a(0)v_0/v$ and $\Sigma_s(u) = \Sigma_s(0)v_0/v$ gives the equation

There is an essential singularity at $s = -\Sigma(0)v_0$ so to invert this equation it must

$$\phi(u,t) = Qv_0 \delta(u) e^{-v_0\Sigma(0)t} + \frac{Qv_0}{\Sigma_s(0)} \left(\frac{\Sigma_s(0)v_0 t}{u} \right)^{\frac{1}{2}} I_1(2\sqrt{\Sigma_s(0)v_0 u t}) e^{-u - v_0\Sigma(0)t}. \quad (3.27)$$

first be expanded in a Laurent series, after which we obtain,

Energy and Space Dependent Solutions

Here, we solve the energy-space dependent problem. These solutions are from the work of McInerney (1963,1965). For this study, we assume plane symmetry and an energy-independent scattering cross section with a planar monoenergetic, isotropic source. The inhomogeneous neutron transport equation is of the form,

$$\left(\mu \frac{\partial}{\partial x} + 1\right)\phi_G(x,\mu,u) = \frac{\delta(z)\delta(u)}{2} + c \int_0^u du' \int_{\Omega'} d\Omega' \phi_G(x,\mu',u') f(\mu_0, u - u'). \quad (3.28)$$

Where z is in units of optical depth and c is Σ_s/Σ_t.

The scattering kernel, $f(\mu_0, u - u') = \dfrac{e^{-(u-u')}}{2\pi}\delta(\mu_0 - e^{-(u-u')/2})$ implies spherically symmetric elastic scattering in the center-of-momentum frame. It neglects

65

chemical binding and nuclear motion. The procedure for solving this equation

consists of taking the Laplace transform in lethargy. Then a complete set of
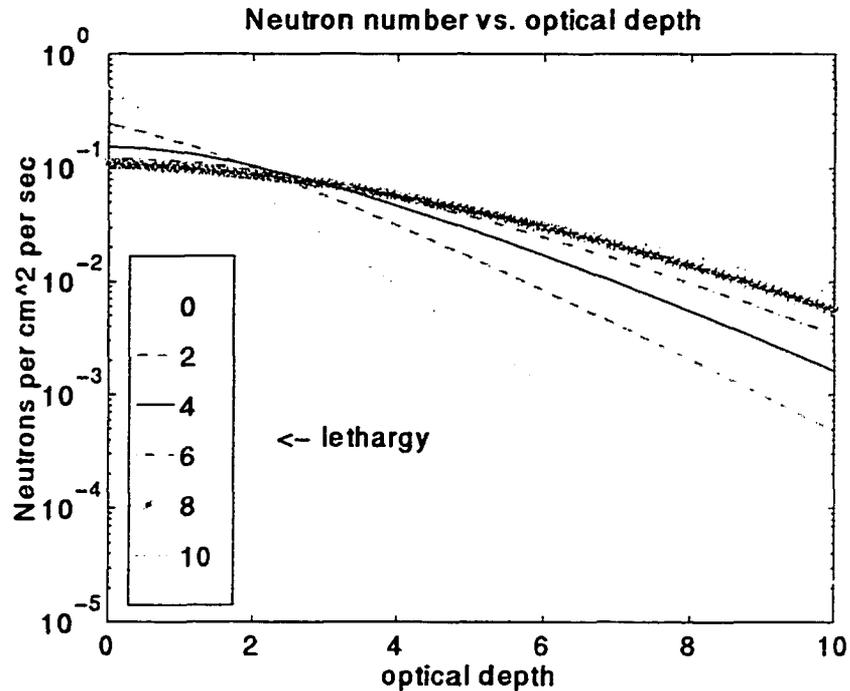
Figure 3.4 - Neutron distribution as a function of optical depth.

eigenfunctions for the transformed equation can be found. The discrete

eigenfunctions describe diffusion-like behavior of the neutrons that have

undergone many collisions. The continuous eigenfunctions have a spatial

dependence similar to the neutrons that have yet to undergo their first scatter.

This means the discrete eigenfunctions contain the spatially asymptotic flux, and

the continuous eigenfunctions are called transients. The transients are only

important near the source. There are no sources for $u > 0$, thus the contribution

of the transients for $u > 0$ is small.

The asymptotic solutions obtained by various authors agree with this

66

solution when the appropriate limits are taken (Weinberg and Wigner 1958). McInerney (1965) has also shown that these results agree well with Monte Carlo calculations over a large range of lethargies. The solution can be expressed in terms of modified Bessel functions (I_0) and exponentials. The angle-integrated solution is as follows:

$$\phi_0(x,u) \approx \frac{e^{-\left(x+\frac{21}{40}u\right)}}{2} I_0\left(\sqrt{\frac{5}{3}ux}\right) + \frac{13}{120} \cdot \int_0^u \frac{e^{-\left(x+\frac{21}{40}u'\right)}}{2} I_0\left(\sqrt{\frac{5}{3}u'x}\right) du' \quad (3.29)$$

The neutron distribution as a function of optical depth for several different lethargies is shown in Figure 3.4. The lower energy neutrons travel farthest from the source. This is what we expect physically because these neutrons have undergone the most collisions. This is evident in a plot of the distribution as function of energy (Figure 3.5). The neutrons farthest from the source increase
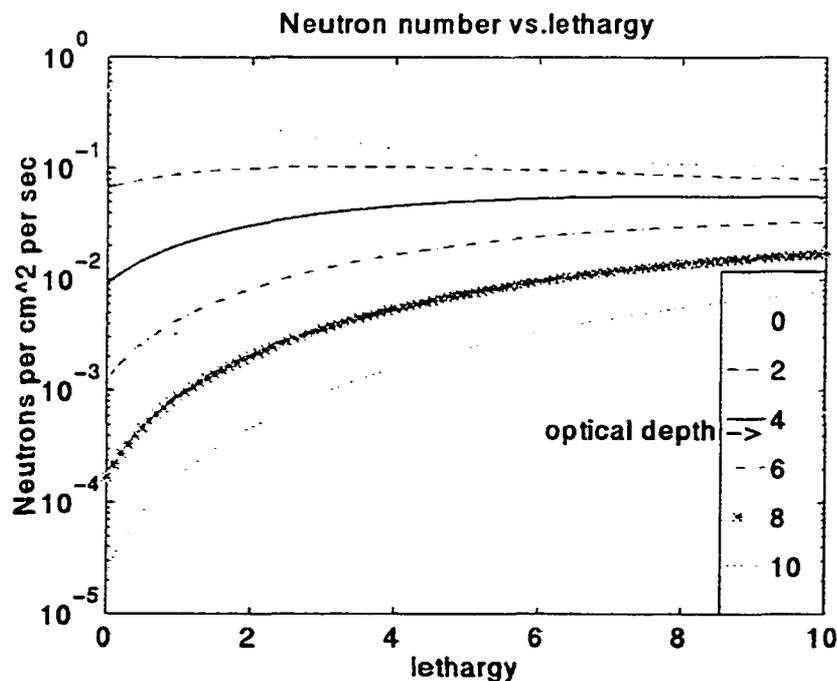
Figure 3.5 - Neutron distribution as a function of lethargy.

67

with decreasing lethargy and those near the source are greatest as the lethargy approaches 0.

Slowing Down with Heavier Elements

Once we consider the moderation of neutrons in a medium other than hydrogen, we can no longer compute exact solutions for any of the previous examples we discussed. The parameter α is no longer zero so the energy loss range no longer starts at zero. This has an advantage though. We can now use approximations that were not allowed for a hydrogen atmosphere. This stems from the fact that a neutron cannot lose all energy in a single collision on nuclei other than hydrogen. There are several techniques available, but the one we chose to use here is Fermi age theory (Beckurts and Wirtz 1964). The first approximation we make is that Fick's law applies. This states that the neutron current density is proportional to the gradient of the flux, $J(\vec{r},u) = -D(u)\nabla\Phi(r,u)$, where $D(u) = \dfrac{1}{3\sum_s(u)(1-\frac{2}{3}A)}$. For heavy moderators since the maximum energy loss is small we can approximate the collision density as $q(u) = \xi\sum_s\Phi(u)$. We now define the Fermi age as,

$$\tau(u) = \int_0^u \frac{D(u')}{\xi\sum_s(u')}du' = \int_E^{E_{source}} \frac{\lambda_s^2(E')}{3\xi(1-2/3A)}\frac{dE'}{E'} \quad (3.30)$$

in place of energy, we can write the transport equation as,

$$\frac{\partial q(\tau)}{\partial \tau} = \nabla^2 q(\tau) - \frac{\Sigma_a/\xi\Sigma_s}{D(u)/\xi\Sigma_s}q(\tau) + S(r)\delta(\tau). \quad (3.31)$$

68

Thermalization

At the end of the slowing-down process, a neutron reaches thermal energies; i.e., its energies approach those of the moderating medium. At this point, the neutron diffuses in a random walk until it is either captured or if there is a free-escape surface, escapes. The transition from the slowing-down regime to "thermalization" is a continuous process and in general is complicated (Beckurts and Wirtz 1964). Thermalization in general is a more difficult problem than slowing-down because now chemical binding and atomic motion are important. Despite this, certain approximations can be made that still produce useful results. We will assume the process is discontinuous, i.e., we use the neutron distribution developed for slowing down as the source for the thermalization problem. Doing this contradicts an assumption that the slowing-down density could be calculated assuming the moderating atoms are at rest. In addition, this method assumes the source of thermal neutrons is already in equilibrium with the thermal distribution.

A useful elementary case is that of an infinite medium with a homogeneously distributed fast-neutron source. If we assume that absorption during slowing-down is small. The slowing-down density q and the thermal flux Φ_{th} are space-energy independent. The thermal flux is related to q by the relationship $\Phi_{th} = q/\Sigma_a$. A useful relationship is the ratio of the thermal to epithermal flux. The epithermal flux per unit lethargy $\Phi_{ep} = q/\xi\Sigma_s$ is constant between one eV and several keV because $\xi\Sigma_s$ is constant. We then see that

69

$\Phi_{th}/\Phi_{ep} = \xi\Sigma_s/\Sigma_a$, i.e., the thermal flux is larger the larger the moderating ratio. This is perfectly exemplified in the interplay between the amount of H and ^{3}He in the photosphere. The thermal flux and thus the 2.2 MeV emission are very sensitive to the ratio of the moderating H to the absorbing ^{3}He.

The study of neutron transport and neutron capture in the solar atmosphere generally requires the use of complex Monte Carlo simulations (Hua and Lingenfelter 1987). This is because neutrons can undergo many nuclear reactions with the ambient solar material. In addition, the geometry of the system must be included. For lower energy neutrons (<10 MeV) general inelastic scattering cross-sections are small. In the next chapter we show that an interval during a flare contains lower energy protons and thus low energy neutrons. This allows us to use our transport model to determine the distribution of thermal neutrons in the solar atmosphere. This intern allows us to determine the ^{3}He abundance.

For our model of a hydrogen atmosphere, we chose to use the slowing-down distribution at a lethargy corresponding to thermal neutrons. Neutrons degrading from 10 MeV to 0.5 eV have a lethargy of 16.8. For this case the thermal distribution as a function of depth in mean free paths becomes,

$$\phi_{th}(x) \approx \frac{e^{-(x+8.82)}}{2} I_0\left(5.29\sqrt{x}\right) + \frac{13}{120} \cdot \int_0^{16.8} \frac{e^{-\left(x+\frac{21}{40}u'\right)}}{2} I_0\left(\sqrt{\frac{5}{3}u'x}\right) du' . \quad (3.32)$$

70

We can see from the figure 3.6 the distribution of thermal neutron as a function of depth and lateral displacement. These neutrons are the source of the 2.2 MeV capture line.
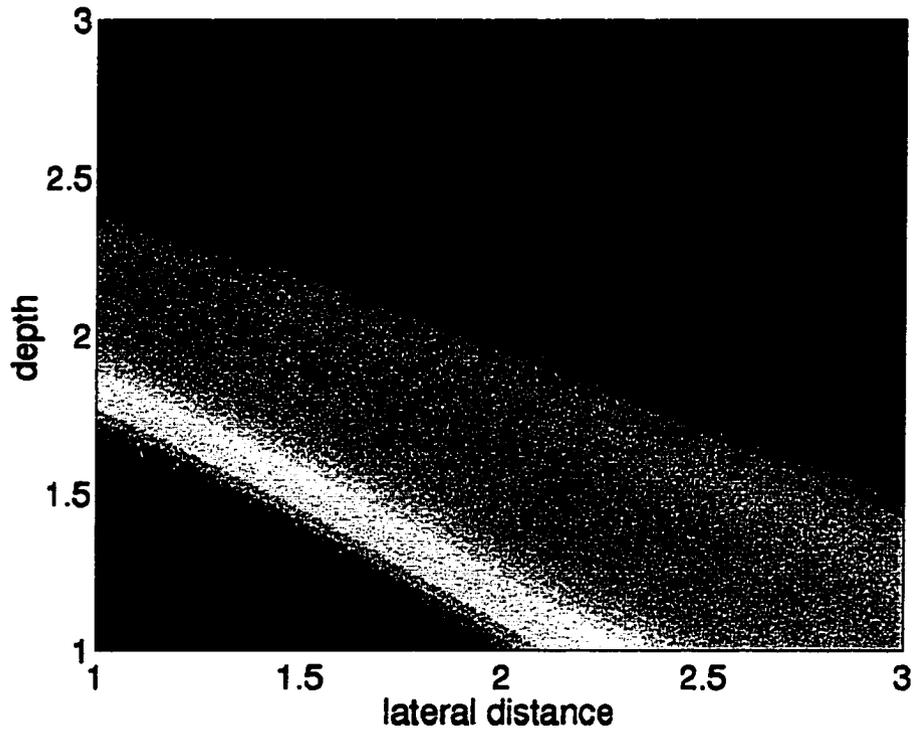
Figure 3.6 - Thermal neutrons due to a source at optical depth 0.

71

CHAPTER IV

ANALYSIS

Inverse Problems

Given a measured energy deposit spectrum we can extract spectral information such as constraints on model parameters and an estimate of the incident photon spectrum. This is the classic problem of spectral deconvolution or spectral inversion. In the ideal case this is equivalent to solving an integral equation for the photon spectrum f(E') given the measured energy loss spectrum C(E) and the energy response of the detector R(E',E),

$$C(E) = \int_0^{E'} R(E,E')f(E')dE' . \quad (4.1)$$

The solution to this deceptively simple equation is part of a larger class of problems commonly referred to as inverse problems. Many mathematical and statistical aspects of inverse problems were discussed in by Craig and Brown (1986) and by Hansen (1998). Here we will discuss some of the assumptions and challenges associated with solving this problem along with some existing methods. If we had the exact continuous forms of C and R we could, in principle, solve the integral equation that is just a Fredholm equation of the first kind (Craig and Brown 1986; Hansen 1998; Press et al. 1992). The first problem we

72

encounter in the search for a solution, due to the discreteness of our measured data, is the uniqueness of the solution. The count data C(E) are only known for a discrete set of energies, E_i, where i=0,...,n-1. We are then solving a set of n integral equations but many functions can satisfy a given discrete set of equations without satisfying our original equation. The first problem is the existence of a solution at all. The instrument response is seldom described analytically so that we then must replace the set of integral equations with the

$$C_i = R_{ij}f_j \text{ for } i = 0,...,n-1 \text{ and } j = 0,...,m-1. \quad (4.2)$$

matrix equation,

The formal solution of this equation is $f=R^{-1}C$ but usually R^{-1} is unbounded and its computation is sensitive and unstable to small perturbations in the data. The inverse problem is then termed "ill-posed".

There exist a number of "classical" methods for numerical inversion of matrix equations and they were discussed in detail by Craig and Brown (1986), Hansen (1998), and Press et al. (1992). These methods are classical in the sense that they explicitly use prior information or make any assumptions about the source function (Craig and Brown 1986). Due to many shortcomings we do not use any of these methods but instead use "non-classical" or regularization methods. The general idea of regularization is to introduce an extra term (or regularization function ϕ) to minimize irregular solutions, i.e.,

$$L(f) = \|C - Rf\|^2 + \phi(f, \alpha) . \quad (4.3)$$

73

The free parameter α is chosen to balance the minimization of the norm (correct inverse) versus the suppression of noise (smoothing). Many of the regularization methods discussed in the above texts approach the inverse problem from a purely deterministic point of view. Due to the need for the understanding of the measurement errors and the need to determine the statistical significance of the data, we chose to approach the problem for a statistical formalism. The problem can be presented in the same fashion as deterministic approaches but instead we determine our regularizing function statistically (Craig and Brown 1986). Below, we will discuss two commonly used techniques and we present the use of a novel new method applied to γ-ray spectroscopy.

Forward Folding

The method of forward folding is commonly used in γ-ray and X-ray astronomy. A model μ is convolved (folded) with the detector response **R** yielding a model set of data **d**. A maximum-likelihood fit of the real data **C** with the model data is then preformed maximizing the log of the probability (or in the case of Gaussian statistics minimizing χ^2). This procedure has the disadvantage that it is inherently restricted to the assumed model. One does not obtain an estimate of the real spectrum but rather a set of parameters associated with that model. However, when the model choice is appropriate and realistic and the response is dominated by diagonal elements the inferred spectrum is robust.

Maximum Entropy

Maximum Entropy methods are also popular for the deconvolution of image data and have proven to be successful in spectral deconvolution (Gull and Daniel 78, Gull and Skilling 90). In addition to maximizing a likelihood, prior information in the form of information entropy S is maximized. Many versions of S have been defined in the literature. We use S defined by (Gull and Skilling 90),

$S = \sum_{i=1}^{n} (\mu_i - m_i - \mu_i \log(\mu_i/m_i))$, with m_i, being the prior model for μ_i. The balance between entropy (smoothest solution) and χ^2 (best fit) is controlled by the regularization parameter alpha. For a Gaussian likelihood the log probability is maximized over α and μ_i, i.e. minimizing the quantity $-\alpha S + \frac{1}{2}\chi^2$.

Bayesian Multiscale Regularization

The methods of forward folding (i.e. parameter fitting) and maximum entropy "deconvolution" (i.e., estimating independent input photon rates for each individual energy bin), have been used successfully for gamma-ray solar flares (e.g. Rank, 1996; Share and Murphy, 1995). These methods worked well under certain conditions but there are situations were they do not apply. These are: 1) when no reasonable model (e.g. fewer parameters than data bins) is yet known, for forward folding; 2) when one expects a mixture of broad and narrow features (e.g. solar flares), for the maximum entropy method; and 3) low count rates and low signal-to-noise, for both. Low count rates are a problem because these methods (as they have been implemented) assume Gaussian statistics whereas

75

the small numbers require Poisson statistics. Background subtraction techniques often lead to negative count rates. For Poisson data the Maximum Likelihood Estimator (MLE) with a Poisson likelihood is appropriate. Without a regularization term, trying to estimate the "true" individual input photon rates per bin can be an ill-posed problem, even without including both broad and narrow features in the spectrum. One way to implement this regularization, though, is through the use of a suitable Bayesian prior. Nowak and Kolaczyk (1999) developed a fast, robust, technique using a Bayesian multiscale framework that addresses these problems with added algorithmic advantages. We outline this new approach so that we can apply it to solar flare gamma-ray spectroscopy.

Recent treatments of Poisson inverse problems have augmented the likelihood equations with a regularization or penalization term as discussed above. This regularization term stabilizes the otherwise ill posed ML problem. The regularization term can take the form of a Bayesian prior so that the MLE is replaced with the Maximum *a posteriori* (MAP) estimator. If we wish to use a MAP estimator, we first apply Bayes' theorem,

$$p(\lambda|y) = \frac{p(y|\lambda)p(\lambda)}{p(y)} . \quad (4.3)$$

This equation relates the likelihood to the posterior with the prior $p(\lambda)$ and $p(y)$ being a normalization based on the data. The prior can also be interpreted as a penalizing function giving the terminology "Penalized MLE". The MAP estimate is then the value of λ that maximizes the log of the posterior, $L(\lambda)$. Thus, we are

76

maximizing $L(\lambda) = \log p(y|\lambda) + \log p(\lambda) + \text{constant}$ or the log of the likelihood plus the log of the prior.

Multiscale analysis is the study of behavior or structure in data at various spatial and/or temporal scales (Mallat 1998). One way to address our ill-posed problem is through a multi-scale framework (Starck, Murtagh, and Bijaoui, 1998). The usual multi-scale model is formulated with a wavelet decomposition but wavelets and Poisson data are somewhat incompatible (Kolaczyk 1999b; Nowak 1998). Nowak and Kolaczyk (1999) developed a deconvolution technique that uses a Bayesian multiscale framework that addresses these problems with other advantages. Below we outline this new approach and demonstrate its application to solar flare gamma-ray spectroscopy.

This deconvolution technique was originally developed for use with Positron Emission Tomography (PET) imaging. We chose to adapt this method to gamma ray spectroscopy primarily because it addresses the issue of low count rates, but it has other advantages as well. The first advantage is its computational simplicity. The technique uses an Estimator Maximization (EM) algorithm that has a closed-form step at each iteration. A second advantage is the estimates' uniqueness. Under reasonable choice of the multiscale priors, the EM algorithm converges to a unique, global MAP estimate.

The problem at hand is to estimate the photon flux, λ, from the observed count data y. The counts are related to the flux by the relation $y_n = P(\mu_n)$, $n=0,...,N-1$, where $P(\mu_n)$ is the Poisson distribution with mean counts μ_n. The

77

mean counts μ_n are related to the flux by the relation $\mu = \mathbf{R} \bullet \lambda$, where R is an N × M matrix (the response) of transition probabilities. The response, when its rows are normalized so as to sum to unity, gives the probability that a photon (in emission space) emitted at energy location m will be detected (in detection space) at detector channel location n.

It will be useful later in this discussion to introduce the idea of the "complete data" z(n,m). This is the total number of m to n (emission to detection) events, $z(n,m) = P(\lambda_m R_{n,m})$. The indirectly observed count data is then given by summing the complete data over m, $y_n = \sum_m z(n,m)$. Also, were we able to detect the photons directly without the detector we would have the direct data, $x_m \equiv \sum_n z(n,m)$, from which it follows that $x_m = P(\lambda_m)$.

To seek a solution of the general inverse problem we must first solve the direct-data Poisson estimation problem, $x_m = P(\lambda_m)$. The simplest multiscale data analysis is the unnormalized Haar analysis, defined as,

$$x_{J,m} \equiv x_m, \quad m = 0,...,2^J - 1$$
$$x_{j,m} = x_{j+1,2m} + x_{j+1,2m+1}, \quad m = 0,...,2^j - 1, 0 \le j \le J-1. \tag{4.4}$$

The index j refers to the resolution of the analysis, 2j, where j = J is the index for the highest or finest scale and j = 0 is the lowest or coarsest scale. The reason for using the Haar analysis is that the decomposition is just a summation and that the sums of independent Poisson variates are also Poisson variates. More general wavelet decompositions give arbitrary linear combinations of Poisson variates that are then not necessarily Poisson variates (Kolaczyk 1999a).

78

The data $\{x_{j,k}\}$ are the unnormalized Haar scaling coefficients of **x**. Using conditional probability relationships, the joint probability of the data in a multiscale representation can be expressed with the factorized form,

$$p(\mathbf{x}) = P(x_{0,0}) \prod_{j=0}^{J-1} \prod_{m=0}^{2^J-1} \Pr(x_{j+1,2m} \mid x_{j,m}). \quad (4.5)$$

This expression holds more generally e.g., Gaussian data (Kolaczyk 1999b).

The parent $(x_{j,k})$, child $(x_{j+1,2k})$ relationship is expressed by the conditional likelihood, $\Pr(x_{j+1,2m}|x_{j,m})$. The MAP estimation of λ requires the likelihood function of **x**,

$$p(\mathbf{x} \mid \lambda) = \prod_{k=0}^{2^J-1} \Pr(x_k \mid \lambda_k), \quad (4.6)$$

where $\Pr(x|\lambda)$ is the Poisson probability density function of x with mean λ. The multiscale expansion of $p(\mathbf{x} \mid \lambda)$ requires that we define the multiscale analysis of the intensity λ, analogous to the analysis of **x** defined as,

$$\lambda_{J,m} \equiv \lambda_m, m = 0,...,2^J - 1$$
$$\lambda_{j,m} = \lambda_{j+1,2m} + \lambda_{j+1,2m+1}, \quad m = 0,...,2^j - 1, 0 \le j \le J-1. \quad (4.7)$$

The parameters $\{\lambda_{j,m}\}$ are the unnormalized Haar scaling coefficients of the intensity λ.

Using the definitions for the multiscale analysis of **x** and λ and the multiscale factorization of Pr(**x**) we can express the parent-child conditional likelihood as,

$$p\left(x_{j+1,2m} \mid x_{j,m}, \lambda_{j,m}\right) = B\left(x_{j+1,2m} \mid x_{j,m}, \rho_{j,m}\right), \quad (4.8)$$

where $B(x \mid n, \rho) = \binom{n}{x} \rho^x (1-\rho)^{n-x}$, is the binomial distribution with parameters n

and ρ. The parameters $\rho_{j,m} = \dfrac{\lambda_{j+1,2m}}{\lambda_{j,m}}$ are the canonical multiscale parameters for

the Poisson model and can be viewed as "splitting" factors, governing the

multiscale refinement of the intensity. This type of multiscale analysis was

introduced independently by Timmermann and Nowak (1999) and Kolaczyk

(1999a). We can represent the multiscale analysis of x and λ as a binary tree

where the splitting factors are multiplicative weights in the tree's links. The

complete factorization of the likelihood is then

$$p(x \mid \lambda) = P(x_{0,0} \mid \lambda_{0,0}) \times \prod_{j=0}^{J-1} \prod_{m=0}^{2^j-1} B(x_{j+1,2m} \mid x_{j,m}, \rho_{j,m}) \quad (4.9)$$

where $P(x_{0,0} \mid \lambda_{0,0})$ is just the Poisson probability function of $x_{0,0}$ with mean $\lambda_{0,0}$.

Maximum Likelihood Intensity Estimation

A maximum likelihood analysis of the binomial conditional likelihood leads

to a MLE estimation of the splitting parameters (Nowak and Kolaczyk 1999) of

$\hat{\rho}_{j,m} = \dfrac{\lambda_{j+1,2m}}{\lambda_{j,m}}$. There is a one-to-one mapping from (ρ, λ_{00}) to λ so using the

multiscale synthesis equation (Nowak and Kolaczyk 1999)

$$\hat{\lambda}_{j+1,2m} = \hat{\lambda}_{j,2m} \hat{\rho}_{j,m}$$

$$\hat{\lambda}_{j+1,2m+1} = \hat{\lambda}_{j,2m}(1 - \hat{\rho}_{j,m}), \quad m = 0, \dots, 2^j - 1, 0 \le j \le J - 1 \quad (4.10)$$

80

and the estimate $\hat{p}_{j,m}$ we find the MLE of each intensity element of the finest

scale to be $\hat{\lambda}_{J,m} = x_{J,m} \equiv x_m$. The MLE returns the raw data as our MLE intensity

estimate, an expected result (Nowak and Kolaczyk 1999). The next step is the

MAP estimation.

Maximum *A Posteriori* Estimation

The crucial ingredient in moving from a MLE estimation to a Bayesian

estimation is the choice of a prior distribution $p(\lambda)$. An good choice of prior

reflects known or assumed attributes of the intensity and matches the functional

form of the likelihood (in our case Poisson and Poisson-binomial). Conjugate

priors have the computational advantage that they are obtained by updating the

parameters of the prior based on the measurements (Gelman 1995; Nowak and

Kolaczyk 1999). The natural choice of the conjugate prior for the total intensity λ_{00}

is the gamma probability density,

$$\lambda_{0,0} \sim \frac{\delta^{\gamma}}{\Gamma(\gamma)} \lambda_{0,0}^{\gamma-1} \exp\{-\delta\lambda_{0,0}\} \equiv G(\lambda_{0,0} \mid \gamma, \delta) \quad (4.11)$$

with parameters γ and β where $\gamma>0$ and $\delta>0$. The choice for modeling the splitting

parameter is as an independent beta distributed random variable,

$$\rho \sim \frac{\rho^{\alpha-1}(1-\rho)^{\beta-1}}{B(\alpha,\beta)} \equiv Be(\rho \mid \alpha, \beta), \quad (4.12)$$

$0 \leq \rho \leq 1$, where $B(\alpha,\beta)$ is the standard beta function. We have no a priori

knowledge of asymmetry therefore we use only a symmetric beta prior of mean

1/2 with $\alpha=\beta$. The prior density for λ_{00} and ρ is then

81

$$p(\lambda_{0,0}, \rho) = G(\lambda_{0,0} \mid \gamma, \delta) \prod_{j=0}^{J-1} \prod_{m=0}^{2^j-1} Be(\rho_{j,m} \mid \alpha_j, \alpha_j). \quad (4.13)$$

In our case the gamma prior has negligible effect so the important parameter is the beta prior in the splitting parameters (Nowak and Kolaczyk 1999). The beta priors $\{\alpha_j\}$ reflect our belief or prior knowledge of the intensities regularity (see).

Combining the prior (Equation 5.13) and the likelihood (Equation 5.9) and using the conjugacy of the prior with the likelihood produces a posterior density (Nowak and Kolaczyk 1999),

$$p(\lambda_{0,0}, \rho \mid x) = G(\lambda_{0,0} \mid \gamma + x_{0,0}, \delta + 1) \prod_{j=0}^{J-1} \prod_{m=0}^{2^j-1} Be(\rho_{j,m} \mid \alpha_j + x_{j+1,2m}, \alpha_j + x_{j,m} - x_{j+1,2m}).$$

$$(4.14)$$

MAP estimates of the ρ, λ_{00} yield

$$\widehat{\lambda}_{0,0} = \frac{\gamma + x_{0,0} - 1}{\delta + 1} \quad (4.15)$$

and

$$\widehat{\rho}_{j,m} = \frac{x_{j+1,2m} + \alpha_j - 1}{x_{j,m} + 2(\alpha_j - 1)}, 0 \le m \le 2^j - 1, 0 \le j \le J - 1. \quad (4.16)$$

As with the MLE, the synthesis equations (Equation 4.10) can be used to obtain a MAP estimate of λ. If we chose uniform prior densities, $\alpha_j = 1$ and $\gamma = 1$, $\delta = 0$, we obtain the MLE estimate ($\widehat{\lambda}_{J,m} = x_{J,m} \equiv x_m$).

Moving back to the more difficult Poisson inverse problem: As we showed for the analysis of the directly observed Poisson data, a multiscale factorization of the data likelihood played a key role. For the analysis of the indirectly

82

observed data (which is our ultimate goal) the complete data likelihood plays a key role through the EM algorithm. Nowak and Kolaczyk (1999) show that the complete data likelihood is proportional to the direct data likelihood. The log complete data posterior is then just a combination of the log complete data likelihood (Equation 4.9) and the log prior (Equation 4.13),

$$
\begin{aligned}
L(\lambda) &\equiv \log p\big(\lambda_{0,0}, \rho \mid z\big) \\
&= \log P(x_{0,0} \mid \lambda_{0,0}) + \log G\big(\lambda_{0,0} \mid \gamma, \delta\big) + \\
&\quad \sum_{j=0}^{J-1} \sum_{m=0}^{2^{j}-1} \log B\big(x_{j+1,2m} \mid x_{j,m}, \rho_{j,m}\big) + \log Be\big(\rho_{j,m} \mid \alpha_j, \alpha_j\big) + C,
\end{aligned}
\tag{4.17}
$$

where C is a constant that does not depend on (ρ, λ_{00}). Maximizing Equation 4.17 is simple, one differentiates it with respect to the splitting parameters and the total intensity. This is given by Equations 4.15 and 4.16, leading to a formulation of the EM algorithm.

EM Algorithm

The key to the EM algorithm for MLE (Nowak and Kolaczyk 1999) is the introduction of the complete data, z(n,m). If we could observe these complete data, we have shown that a closed-form maximizer of the complete data posterior exists. The EM algorithm iteratively alternates between computing the expected complete data log-posterior and a maximizer of this function leading to a MAP estimate of the log-posterior. The problem with the MAP-EM algorithm is that now the M-step does not have a closed-form solution. Fortunately, Nowack

83

and Kolaczyk (1999) solved this problem by taking a multiscale approach that does have a closed-form M-step.

Starting with an arbitrary positive initialization of λ^0 say $\lambda^0=1$, the E (estimation) step is equivalent to estimating $z^{(k)}(n,m)$. The M (maximization) step computes the maximizer of the complete data log-likelihood, yielding $\lambda^{(k+1)}$. It turns out that this is found by computing a simple closed-form expression that involves $z^{(k)}$, $\lambda^{(k)}$, and R. The k+1-st iteration of the E-step and M-step of the algorithm are:

- E-Step: Compute the expectation of the log posterior, conditioned on y under the Poisson law induced by $\lambda^{(k)}$. This is equivalent to computing (Nowak and Kolaczyk 1999),

$$z^{(k)}(n,m) = \frac{y_n \lambda_m^{(k)} R_{n,m}}{\sum\limits_{l=0}^{2^J-1} \lambda_l^{(k)} R_{n,l}}. \quad (4.18)$$

- M-Step: Maximize the expected complete-data log-posterior after transforming into the multiscale representation (Equation 4.17). This is a two-step process.

    1. Generate $x^{(k)}$ from $z^{(k)}$.

    2. Calculate $(\lambda^{(k+1)}_{0,0}, \rho^{(k+1)})$ using

$$\hat{\lambda}^{(k+1)}_{0,0} = \frac{\gamma + x^{(k)}_{0,0} - 1}{\delta + 1} \quad (4.19)$$

and

84

$$\hat{p}_{j,m}^{(k)} = \frac{x_{j+1,m}^{(k)} + \alpha_j - 1}{x_{j,m}^{(k)} + 2(\alpha_j - 1)}, \quad 0 \le m \le 2^j - 1, 0 \le j \le J - 1. \quad (4.20)$$

The intensity $\lambda^{(k+1)}$ is then reconstructed using Equation 4.10.

The algorithm has many desirable properties. As an EM algorithm it has the standard property that the posterior probability does not decrease with subsequent iterations and the estimate is non-negative. Also as discussed above if uniform priors with $\gamma=1$ and $\delta=0$ are selected, the MLE method is recovered

(Nowak and Kolaczyk 1999). The algorithm also has the feature that it is computationally simple and is no more demanding than the simple likelihood approach unlike most other proposed MAP solutions (Nowak and Kolaczyk 1999).

Nowak and Kolaczyk (1999) derived a proof showing that for a certain choice of prior parameters the MAP converges to a global solution. This proof further shows that δ plays no role in the convergence and the convergence conditions are satisfied if the hyper-parameters α_j are essentially doubled with decreasing j (fine to coarse scale) with $\alpha_{J-1} > 1$. We found through the simulation of a test line spectrum through the COMPTEL response that $\alpha_{J-1} = 2$ produced statistically (and visually) good reconstructions except for the case of count spectra containing less than 200 source counts. Then a value of $\alpha_{J-1} = 1.5$ produced statistically good reconstructions.

85

Unfortunately, errors or confidence intervals in the traditional sense do not follow (Kolaczyk 1999). In order to produce spectra with which we can then calculate line fluxes and physicals parameters; we must be able to produce errors or uncertainties in our estimates. The most straightforward method for this is to use a parametric bootstrap (Connors 2000; Kolaczyk 2000a; Kolaczyk 2000b; Efron and Tibshirani 1993). The first step in this process is to compute an estimate of a photon spectrum using the BMS method. One then creates artificial data by using the estimate times the response as the mean of a Poisson variate. N of these artificial data are created were N is large, e.g., 10,000. N new estimates of the spectrum are computed from the N synthetic data. The square
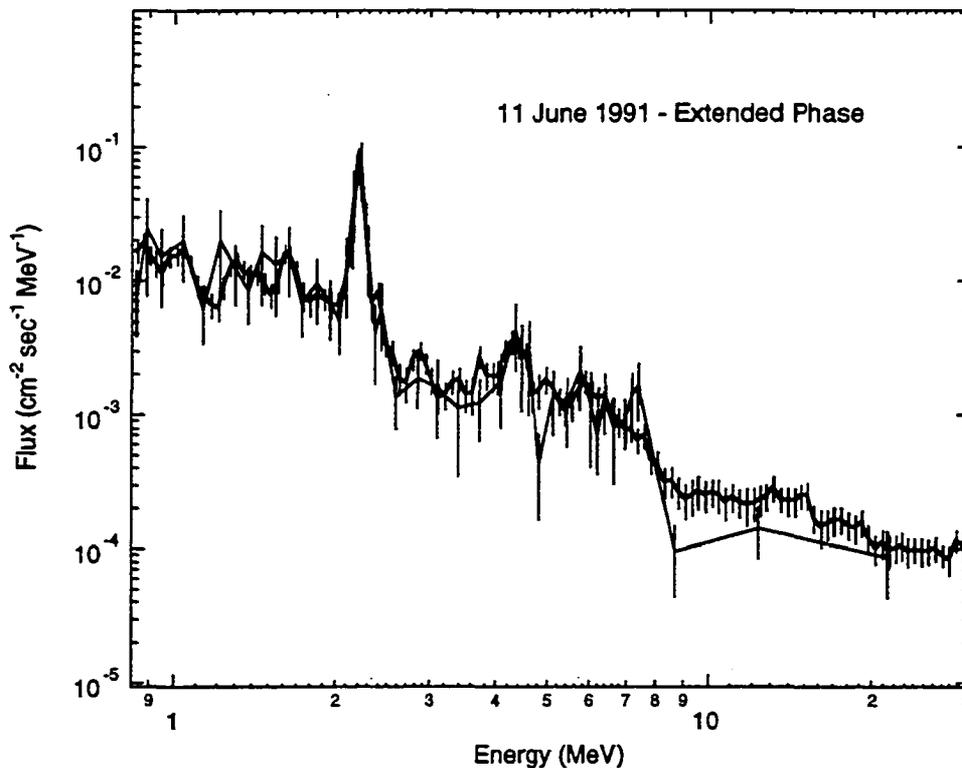
Figure 4.1 - Comparison of Maximum Entropy (large bins) and BMS deconvolution.

86

root of variance we call the error (sigma) for the original spectrum. The errors in the spectrum produced by a parametric bootstrap are estimates of the combined errors in the data and the method (Kolaczyk 2000a; Kolaczyk 2000b).

The Figure 4.1 shows a comparison between parts of the extended phase of the 11 June 1991 flare observed with COMPTEL. The coarser binned spectrum (black) was deconvolved using a Maximum Entropy technique (Rank 1996). The finer binned spectrum (red) was deconvolved using the BMS method we presented here. These two spectra are in good agreement with each other as determined using a χ^2 test. There are several advantages to the BMS method over the Maximum Entropy Method. The BMS is computationally simpler, faster and the solution is more robust. In order to obtain a stable solution using the Maximum Entropy Method much larger energy bin were required to ensure that the counts per bin were high. On the other hand the BMS method has allowed for smaller energy bins this enabling us to obtain more detailed spectral information. This technique is used in the next chapter to study the spectrum of two gamma-ray solar flares.

87

CHAPTER V

RESULTS AND CONCLUSIONS

20 January 2000

On January 20, 2000, a GOES C4.1 class solar flare occurred. The soft X-ray flux began at 8640 s (02:21 UT) peaked at 8760 s (02:26 UT) and ended at 9000 s (02:30 UT). There was no Hα identification but the Nobeyama radio telescope observed a radio burst from the flare at N15W33 corresponding to NOAA active region number 8829. COMPTEL's rapid gamma ray burst response
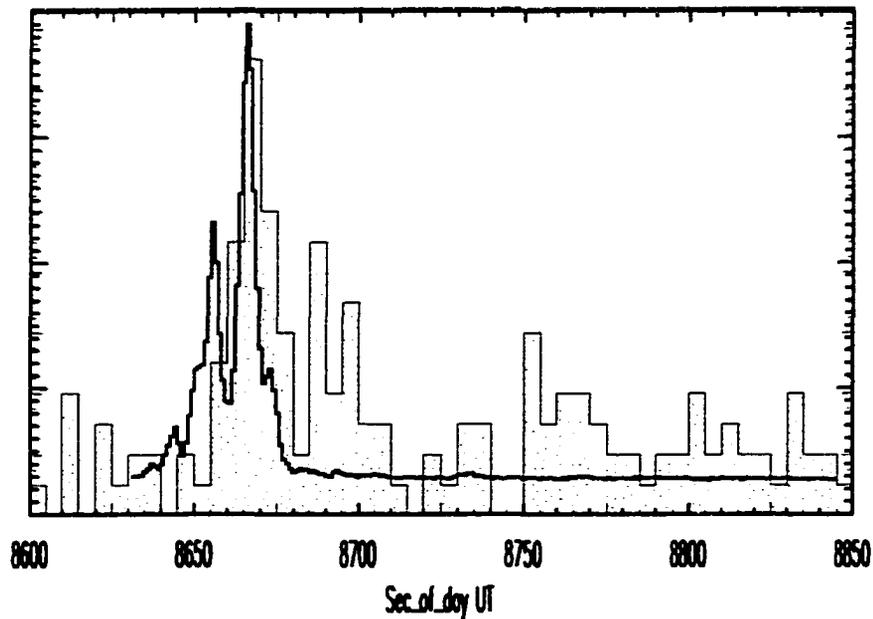
Figure 5.1- Light curves of the 20 January 2000 events observed in BATSE 1024 ms data (solid line) and the COMPTEL telescope (histogram).

system was triggered by BATSE at 8642 s. The trigger from BATSE also alerted

OSSE, which subsequently slew its four detectors to the direction of the Sun.

The automated system of COMPTEL imaged the Sun at a significance of

7.2 σ using 94 events recorded from annuli within 1° of the Sun. Significant

emission was detected from approximately 8640 s to 8740 s (Figure 5.1). There

is evidence in the energy loss spectrum for nuclear line emission from ~1 – 10
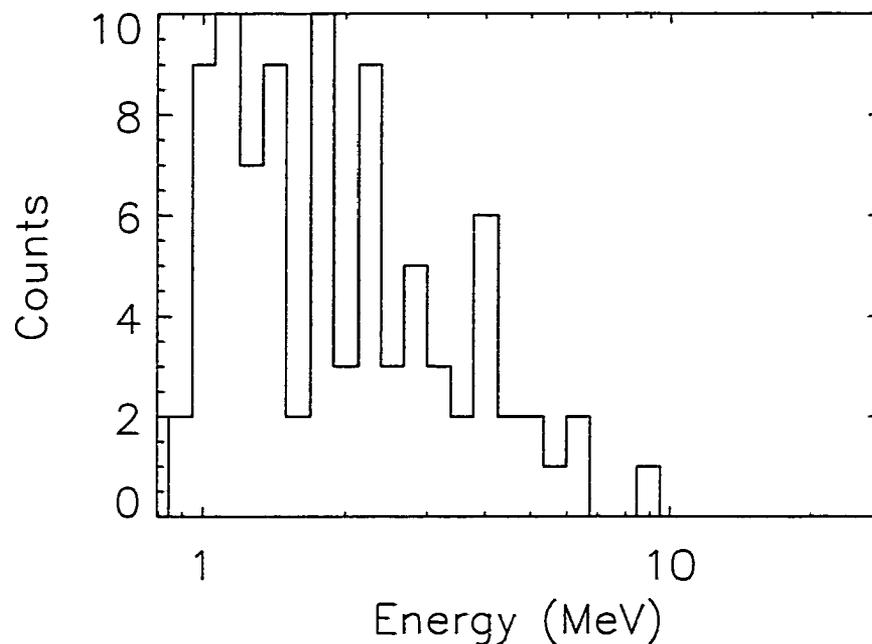
Figure 5.2 - COMPTEL energy loss spectrum of the 20 January 2000 solar flare.

MeV (Figure 5.2). The flare was only observed in the telescope mode, no

emission was detected in the raw or processed burst data.

OSSE observed emission above one MeV during the time from 8663 s to

8696 s (OSSE solar flare web page). A single power law with photon spectral

index -2.85±0.3 (Murphy 2000) provided an adequate fit to the OSSE data with no evidence of nuclear line emission. The total fluence above 50 keV and 1 MeV was 86±1 and 0.8±0.6 photons cm^{-2}, respectively (Murphy 2000). The OSSE data place a 2-σ upper limit for the 2.223 MeV neutron capture line of 0.4 photon cm^{-2}.

Two solar radio observatories also observed the solar flare. Hiraiso Radio Spectrograph (HiRAS) observed emission from 8628 to 8940 s in 200 MHz, 500 MHz, and 2.8 GHz light curves and a type III burst in the 25-2500 MHz spectrum analyzer (HiRAS web page). The Nobeyama Radio heliograph observed the event from 8641-9261 s with peak flux at 8666 s at 17 and 34 GHz (Nobeyama web page) (Figure 5.3).
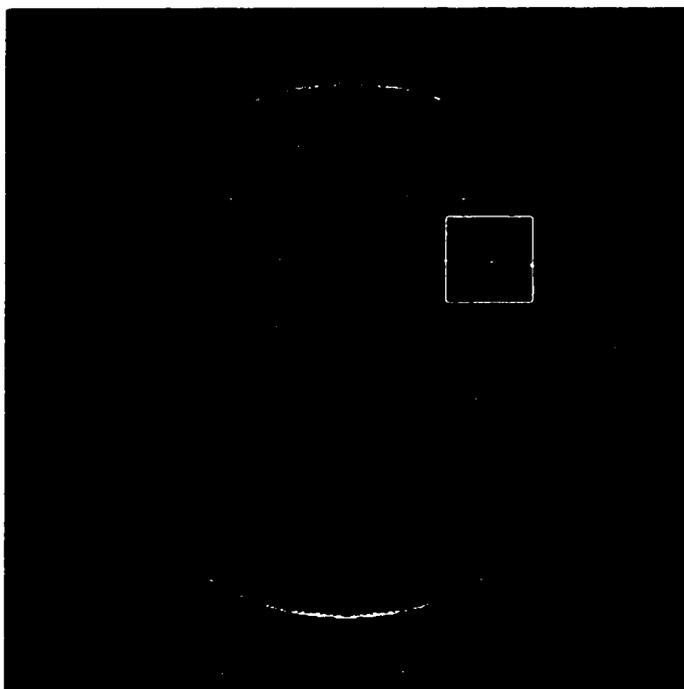
Figure 5.3 - Nobeyama image map of the 20 January 2000 solar flare.

90

We selected the analysis interval for the COMPTEL telescope data to be 8640 s to 8740 s. Normally, the background is modeled by using the average of 15 and 16 orbits before and after the event so that the geomagnetic conditions during the flare are similar. However, due to large data gaps only data 15 orbits before the flare are available. This limits the ability to produce the most accurate
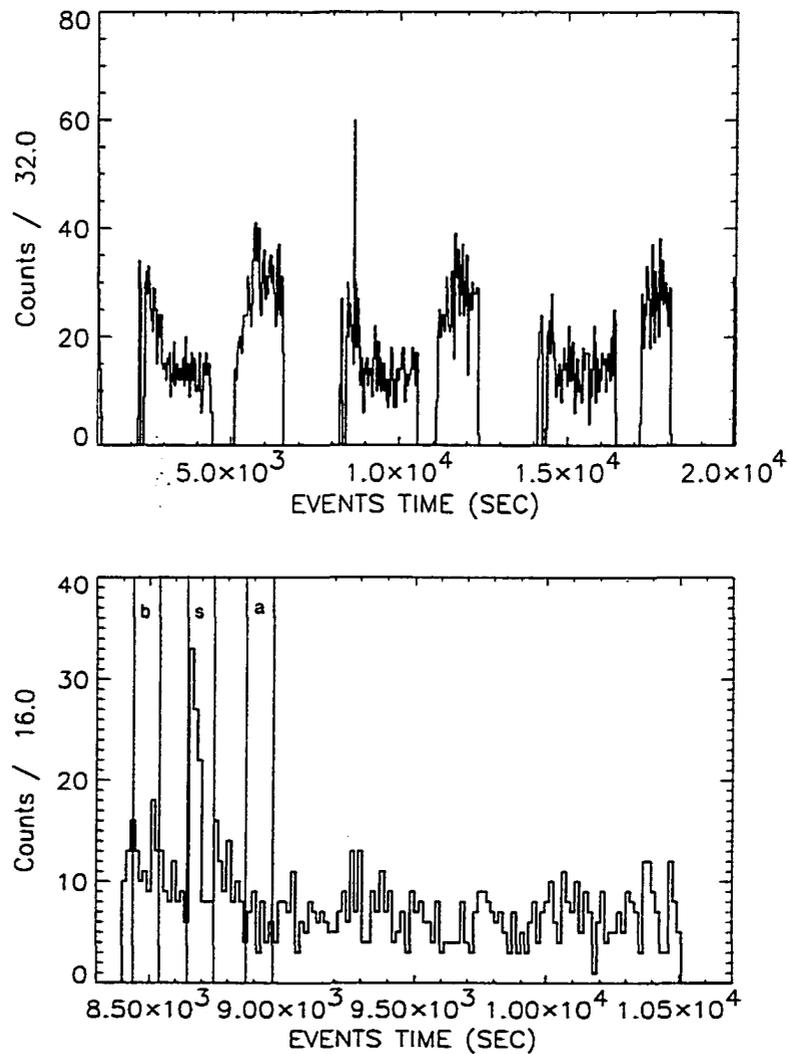
Figure 5.4 – Light curves of the January 20 2000 flare, (a) shows 1000 seconds UT until 20000 seconds UT. The flare around 8640 seconds UT stands out. The region containing the flare between the data gaps at approximately 8400 seconds UT and 10500 seconds UT are shown in (b).

91

background model. Consequently, a different approach to background estimation was necessary. The next reasonable choice was to choose intervals just before and just after the flare as the background estimate. In order for this to be an acceptable choice the background must behave linearly. Figure 5.4(a) shows the count rates from 1000 s until 20000 s. The flare around 8640 s stands out. The

EVENTS TIME (SEC)
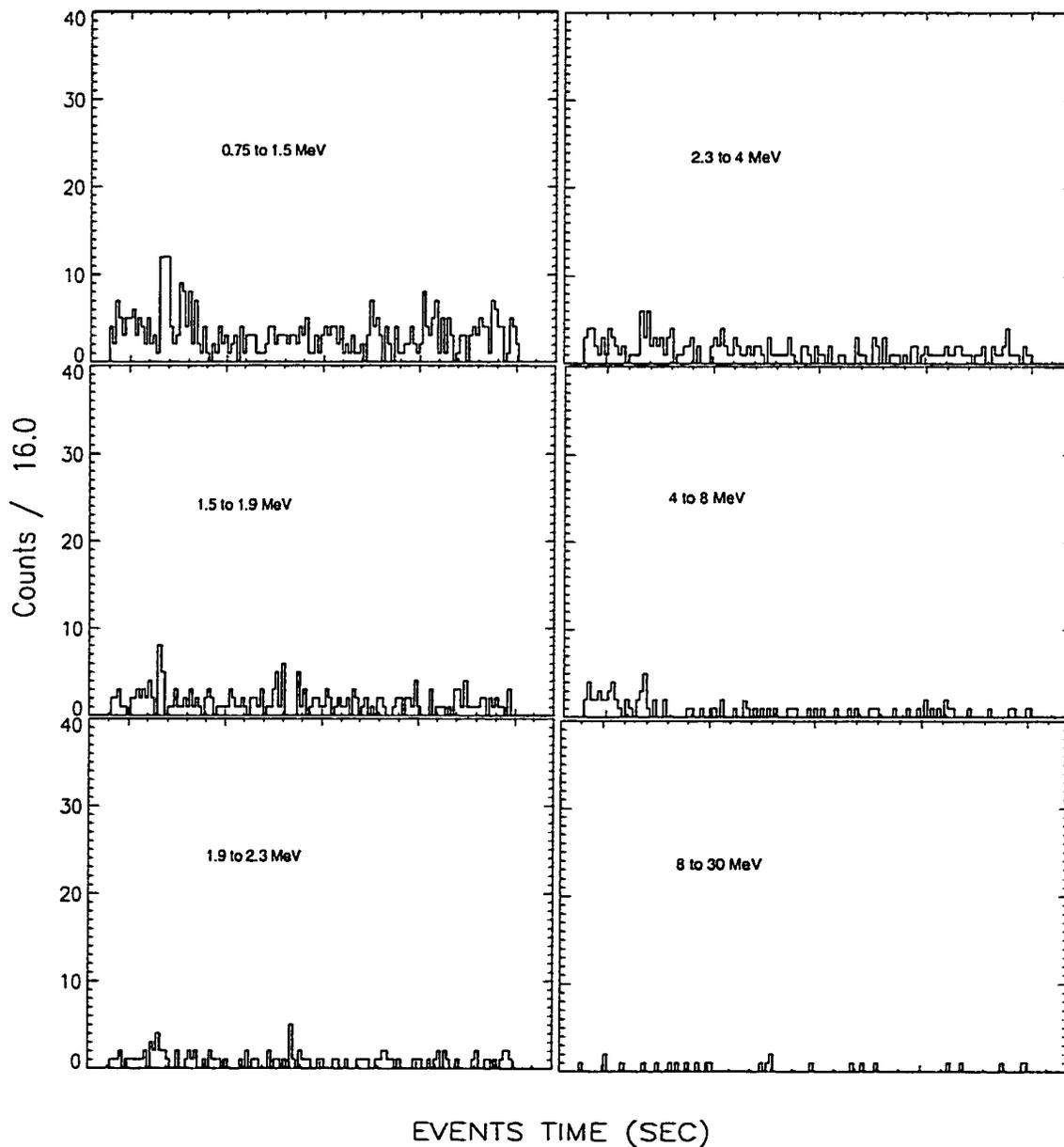
Figure 5.5 - The second light curve interval from Figure 5.4(b) for 6 energy bans (8400 s to 10500s).

92

region containing the flare between the data gaps at approximately 8400 s and 10500 s is shown in figure 5.4(b). The vertical lines show the time intervals for the chosen source and background. The source interval taken to be 8640 s to 8740 s is labeled *s* while the before and after background selections are labeled *b* and *a* respectively. Figure (5.5) shows the second light curve from figure 5.4(b)
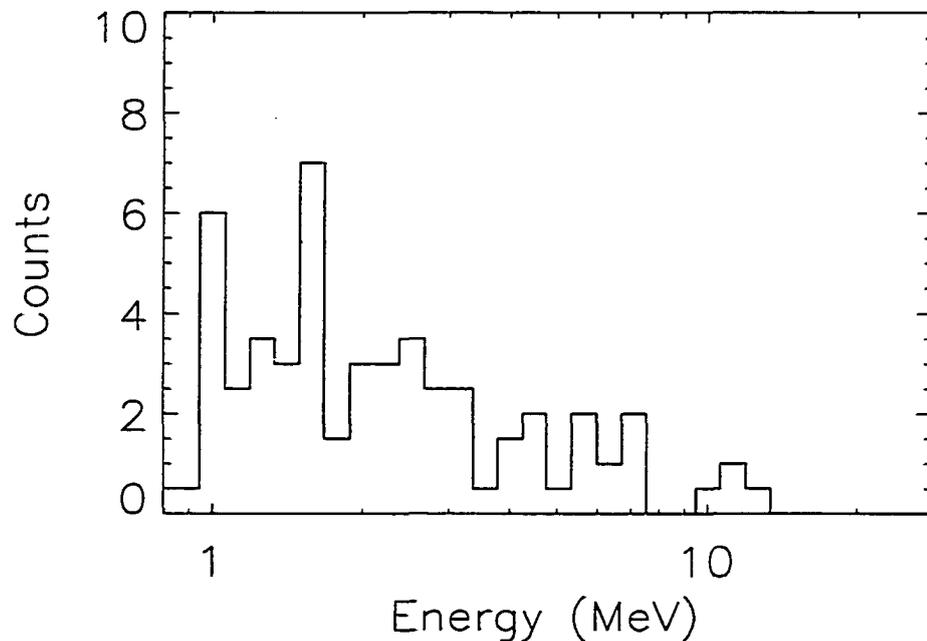
Figure 5.6 – COMPTEL background energy loss spectrum of the 20 January 2000 solar flare.

broken out into 6 energy bans. These light curves show an approximate linear trend so we accept these background intervals. Figures 5.6 and 5.7 show the background and background subtracted source energy loss spectrum.

After this suitable background was selected, the energy loss spectrum (Figure 5.2) and the selected background (Figure 5.6) were deconvolved with the instrument response to obtain an estimate of the flux spectrum. In order to deal

effectively with few counts in the energy loss spectrum at energies greater than ~8 MeV, two energy binning were used. The flux spectrum was computed for a binning of 32 energy bins and 8 energy bins. These two were then combined, using the finer binning up to 8 MeV and the coarser binning greater than 8 MeV.

Ideally, one would fit a gamma-ray spectrum with the individual components of the spectrum varying all parameters. Even for a large, intense event such as the June 4, 1991 event shown in Chapter 1, COMPTEL does not have the statistics to resolve all the components such as the broad lines. A first approach even for a large event is to fit the expected strong lines and a composite spectrum for the remaining lines and continuum, varying only the
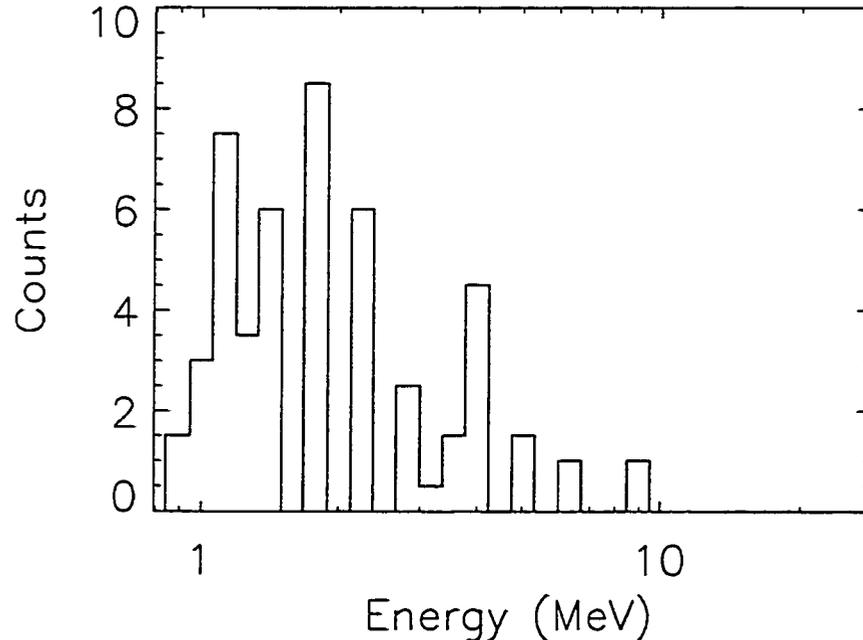
Figure 5.7- Background subtracted COMPTEL energy loss spectrum of the 20 January 2000 solar flare.

94

amplitude of the lines and the composite spectrum. However, for the case of the January 20 flare, the fitting process is more difficult due the small number of counts.

Our approach to obtaining a reasonable model fit was to use data from the BATSE instrument to estimate the intensity and shape of the Bremsstrahlung continuum. Using the most solar-facing BATSE detector, the data from 30 keV to 1000 MeV was fit with a broken power law with a first index of -3.13±0.5, a break energy of 86.7 keV and a second index of -2.85±0.02 yielding a continuum flux above 1 MeV of $(3.2\pm0.2)\times10^{-3}$ γ cm^{-2} s^{-1}. The higher energy power law for the BATSE data is consistent with the fit obtained by OSSE.

In addition to the BATSE based power law continuum, different combinations of several nuclear components were tested. Eight different combinations were used. The two standard components of all the models were the power law from BATSE and a narrow line of unknown strength at 2.223 MeV. The first model contained the addition of 3 narrow lines at 1.1, 1.8, and 4.4 MeV to account for the 3 strongest features in addition to the 2.2 MeV line (These four lines were determined significant with a P-value of 3×10^{-3} (3 σ) by calculating the probability, under the assumption the mean rate of the source is zero, of obtaining as many events as observed or more given the background (see Cowan 1998 pg. 59)). The second model further included a composite spectrum of previously identified broad lines (Share and Murphy 1995).

Model	Broad line template	June 4 narrow line template	SMM 19-flare average narrow line template	Additional narrow lines	χ_v^2	Degrees of freedom	Prob
1				1.1,2.2,1.8,4.4	1.92	8	0.95
2	X			1.1,2.2,1.8,4.4	0.96	7	0.54
3	X			2.2	1.04	16	0.59
4	X	X		2.2	1.07	15	0.62
5	X		X	2.2	1.06	15	0.61
6		X		2.2	1.58	13	0.92
7			X	2.2	1.5	13	0.89
8		X		1.1,2.2	1.58	13	0.92
9			X	1.1,2.2	1.5	13	0.89

Table 5.1 – The set of nine models used in fitting the 20 January 2000 spectrum. The entries with an X indicate the model contained that component. Included with each model is the reduced Chi squared of the fit, the degrees of freedom, and the probability for rejecting the model.

A third model is the same as the second except that the individual three strong lines were replaced with a composite of narrow lines based on the June 4, 1991 flare (see below). The fourth and fifth models contained, the broad line template and the June 4 and 19-flare SMM narrow line templates (see below), respectively. The sixth and seventh models were like the previous 2 models but without the broad component. The eighth and ninth models again contained the June 4 and SMM narrow line templates respectively with the addition of a line at 1.1 MeV because this line is not in the narrow line templates.

The broad line template based on 19 summed SMM flares was used (Share and Murphy 1995; Share and Murphy 1999). The lines used in the template were at 0.819 MeV (^{56}Fe), 1.515 MeV (^{56}Fe;^{24}Mg;^{20}Ne;^{28}Si), 1.979 MeV (Unresolved narrow lines; scattered n-capture; ^{14}N;^{16}O), 4.05 MeV (^{12}C), and

5.175 MeV (^{16}O;^{14}N). The two narrow line templates were taken from the results

presented in the OSSE analysis of the June 4 1991 X12+ flare (Murphy et al. 97).

These results presented as fluxes relative to the 6.13 MeV line are shown in

Table 5.2.

Line Energy (MeV)	CGRO/OSSE	SMM/GRS
1.24	0.35±0.07	0.30±0.03
1.37	0.77±0.09	0.77±0.04
1.63	1.26±0.07	1.36±0.05
1.78	0.60±0.06	0.49±0.04
4.44	1.47±0.06	1.10±0.04
~5.4	0.07±0.03	0.26±0.02
6.13	≡1.00±0.05	≡1.00±0.03
~7.0	0.95±0.06	0.56±0.02

Table 5.2 – The relative (to 6.13 MeV line) narrow line fluxes used in the templates fits for the Jun 4 1991 template and the SMM 19-flare template (Murphy et al. 97).
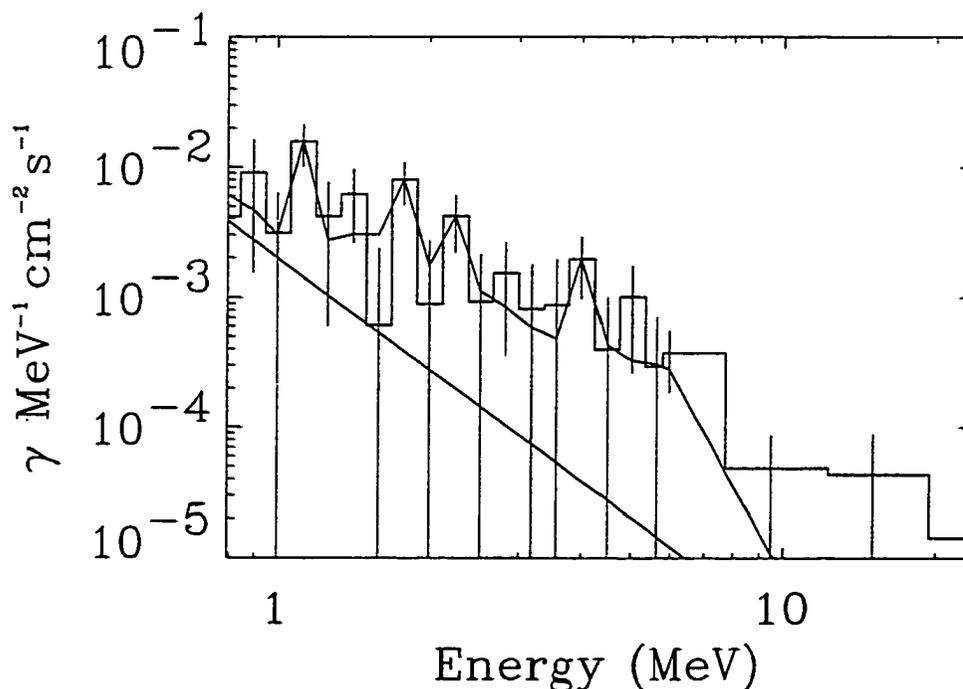
Figure 5.8 – The best-fit model for the January 20, 2000 event. The model consists of a power law based on the BATSE data fit, a broad line template, and lines at 1.1,1.8,2.2, and 4.4 MeV (model 2).

97

A Chi-squared test was used for testing goodness-of-fit against the hypothesis that the model is acceptable. Models 2 (Figure 5.8), 3 (Figure 5.9), 4 (Figure 5.10), and 5 (Figure 5.11) all produced acceptable fits, with indistinguishable probabilities (Table 5.1). Of these four models, we chose model 2 because model 2 is the only one that allowed the narrow line positions to float and it is the only model that contains the significant 1.1 MeV feature.

Using the results from the OSSE solar flare web page (Murphy 2000) and those of Murphy et al. 97, we can compare this small flare (model 2) to the X12+ class flare from 4 June 1991. Based on the OSSE fluence measured above 1
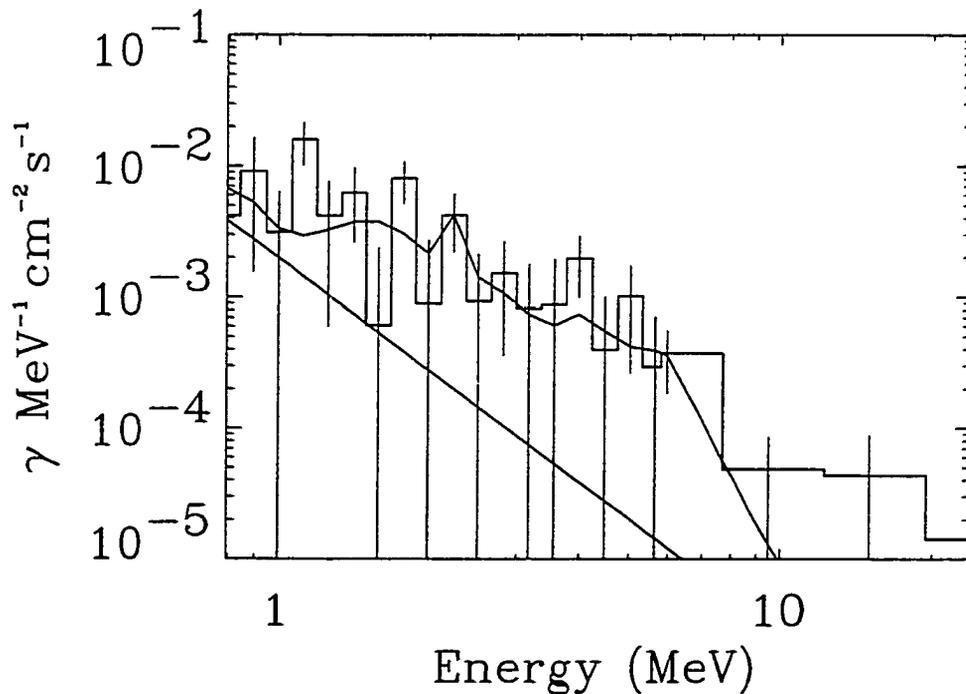
Figure 5.9 – The best-fit model for the January 20, 2000 event. The model consists of a power law based on the BATSE data fit, a broad line template, and a narrow line at 2.2 MeV (model 3).

98

MeV Murphy et al. estimated the 2.223 MeV fluence to be 0.24±0.16 γ cm⁻². This

is consistent with our measurement of 0.23±0.1 γ cm⁻². The 4 June 4 1991 flare

had a strong nuclear component with a ratio of the 2.223 MeV fluence to that of

the above 1 MeV fluence (OSSE solar flare web page) of 0.3. For the January 20

event, COMPTEL measurements gave a ratio of 0.28±0.2. The ratio of the 2.223

MeV fluence to the 4.4 MeV fluence gives a measure of the spectral index of the

parent proton population. Using the results of Ramaty (1996), we obtain an index

of > 5.5 (measured ratio was off the scale). These values are shown in Table 5.2.
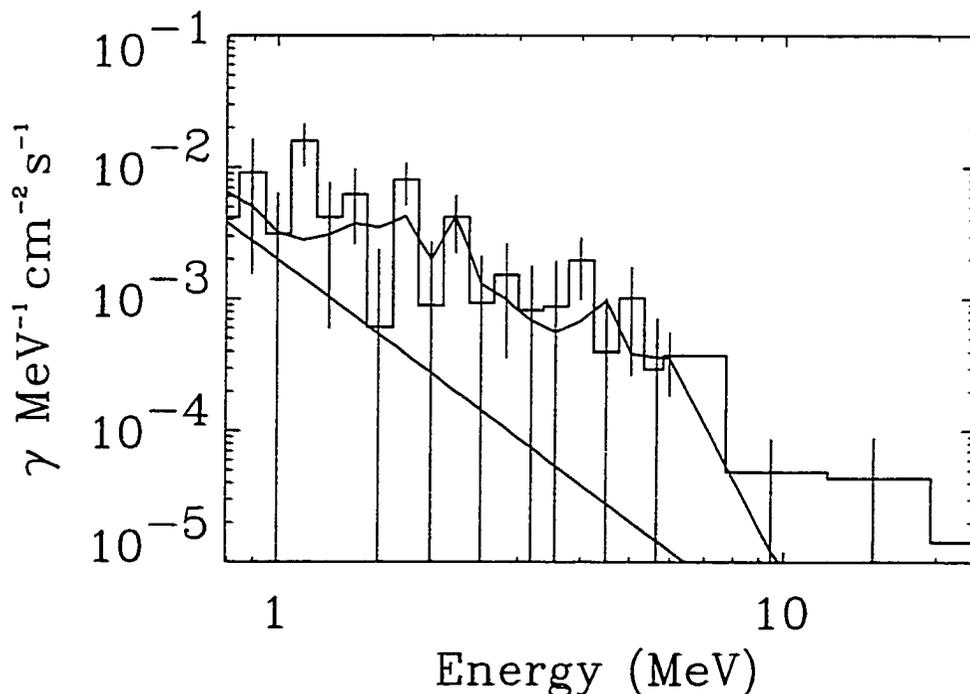
Figure 5.10 – The best-fit model for the January 20, 2000 event. The
model consists of a power law based on the BATSE data fit, a narrow
line template (June 4), a broad line template, and a narrow line at 2.2 MeV
(model 4).

99
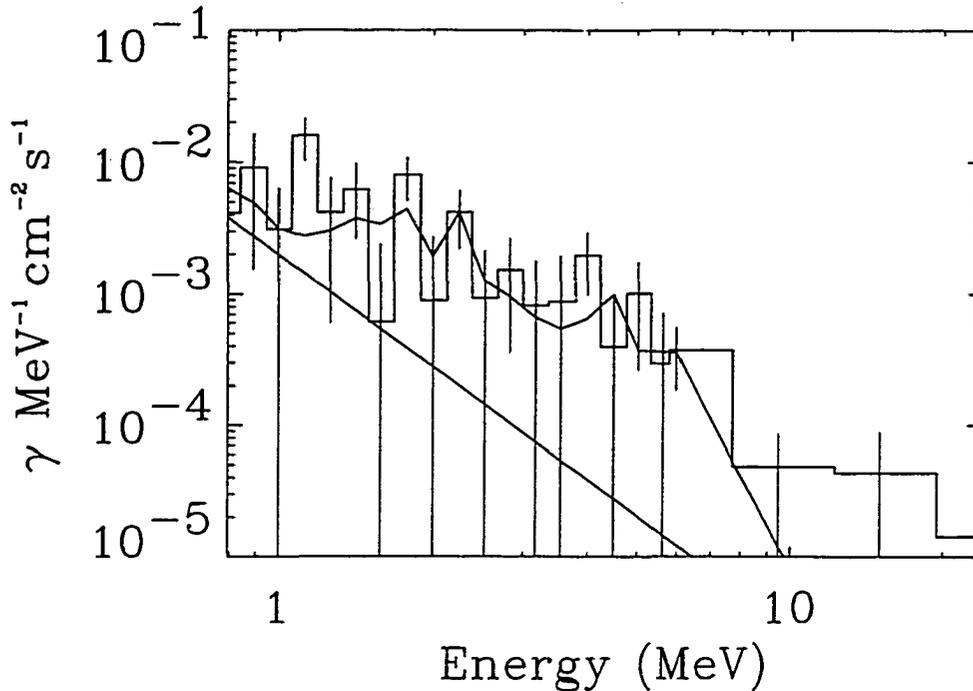
Figure 5.11 – The best-fit model for the January 20, 2000 event. The model consists of a power law based on the BATSE data fit, a narrow line template (SMM), a broad line template, and a narrow line at 2.2 MeV (model 5).

	2000 January 20	1991 June 4
2.223 MeV fluence	0.23±0.1	1050±19
4.4 MeV fluence	1.28±0.1	189±9
> 1 MeV fluence	0.813±0.67	~3500±63
2.223-to-4.4 fluence	0.18±0.14	5.56±0.28
Proton spectral index	>5.5 (α/p = 0.1)	3.37±0.1 (α/p = 0.1)
2.223-to- >1 MeV ratio	0.24	~0.3
# > 30 MeV protons	1×10^{31}	$(6.7 \pm 1.2) \times 10^{32}$

Table 5.3 – A comparison of the COMPTEL measurement of the January 20 2000 C4 GOES event and the OSSE measurement of the June 4 1991 X12+ GOES event.

100

One final important comparison for this flare is with the set of gamma-ray line events observed by SMM. SMM was pivotal in dispelling the idea that gamma-ray line emission was rare and only occurred in the largest of flares. However, due to its sensitivity SMM never had a positive detection of nuclear lines from any of the C class flare that it observed. COMPTEL, which is roughly an order of magnitude more sensitive than SMM has extended the SMM distribution of gamma ray flares by roughly an order of magnitude smaller. Figure 5.9 shows the SMM distribution of flare narrow nuclear line fluence as a function of the continuum power law fluence and GOES soft X-ray class (Vestrand et al. 1999).
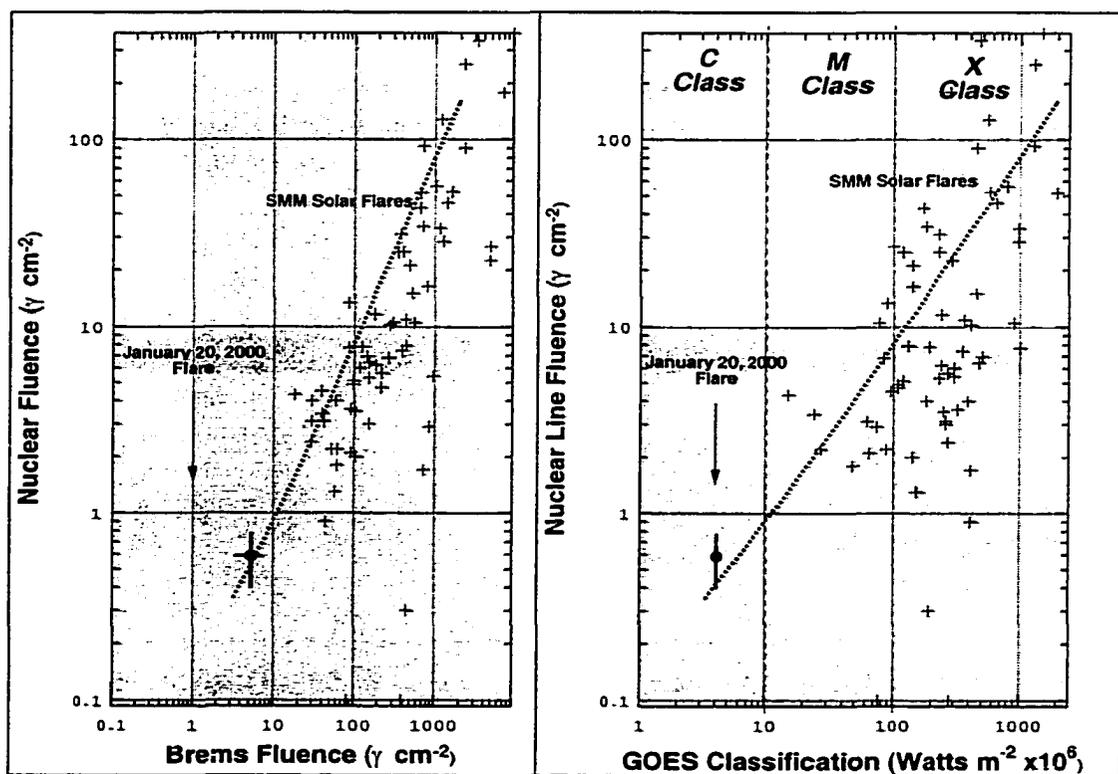
Figure 5.12 - Scatter plots of narrow nuclear line fluence vs. continuum fluence and GOES classification respectively for the SMM GRS catalog and the 20 January 2000 event observed with COMPTEL.

101

All of these comparisons indicate that as compared to the June 4, 1991 flare and the SMM observed gamma-ray flares, the solar flare on January 20, 2000 is a normal or ordinary gamma-ray line solar flare. Actually, this comparison has soon that the 4 June 1991 flares is the odd flare of the bunch. It shows an unusually large electron bremsstrahlung component.

11 June 1991

During the 22nd solar cycle NOAA active region 6659 crossed the solar disk from 1 June to 15 June 1991 and produced some of the largest flares of that cycle. Six X-class flares occurred on 1,4,6,9,11, and 15 June 1991. After the X12 flare on 4 June 1991, the Sun was declared a CGRO target-of-opportunity and CGRO was re-oriented toward the Sun on 9 June 1991. This placed the Sun into the FoV of all CGRO's instruments from 9 to 15 June 1991. On 11 June 1991 a X12/3B flare started at 0156 UT as measured by the 1-8 Å SXR channel of GOES-7. The flare sit was at a heliographic location of N31W17. COMPTEL measured gamma-ray emission from 0.8 to 30 MeV and neutrons for several hours (Ryan et al. 1993; McConnell et al. 1994; Suleiman et al. 1994). This included nuclear line emission, 2.223 MeV emission lasting over 5 hours (Rank 1996) and 8-30 MeV Pion decay emission. The EGRET spark chamber could not observe the impulsive phase due to dead-time effects but observed > 1 GeV emission for at least 8 hours after the peak. The EGRET spectrum showed no sign of a high-energy cut-off (Kanbach et al. 1993). EGRET/TASC impulsive phase measurements of 2.223 MeV emission and nuclear line emission were

102
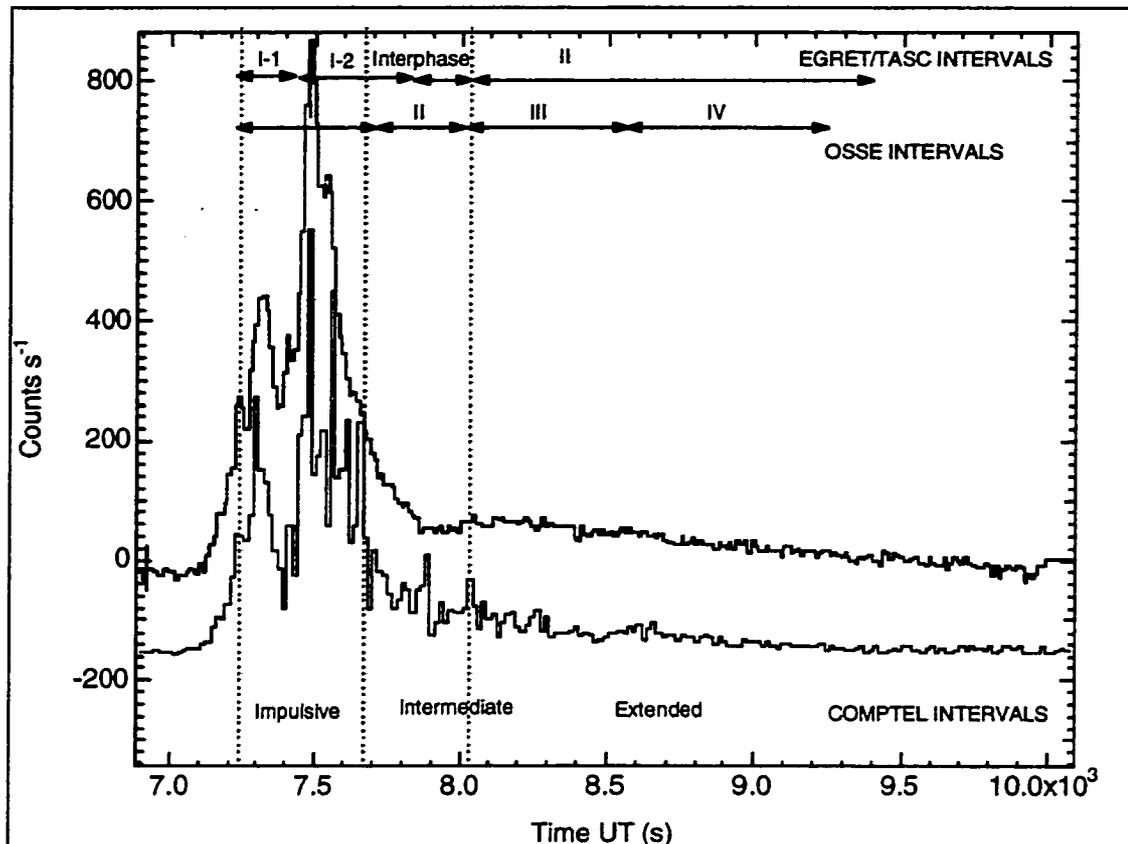
Figure 5.13 – Light curves of the 11 June 1991 X-class solar flare as measured by the COMPTEL telescope (lower-blue) and burst modes (upper-green). Included are the observation intervals for COMPTEL, OSSE, and EGRET/TASC. The curves are slightly offset arbitrarily.

reported (Dunphy et al. 1999; Schneid et al. 1994) along with evidence for pion emission, neutrons and spectral evolution (Dunphy et al. 1999). OSSE reported prolonged 2.223 MeV emission (Murphy et al. 1993) and nuclear emission, 0.511 MeV positron-annihilation emission, >16 MeV gamma rays and neutrons. BATSE-LADs measured HXRs and gamma rays for about one hour in the energy range of 20 keV to ~1.9 MeV. CGRO was not the only gamma-ray experiment that observed the 11 June 1991 flare. GRANAT/PHEBUS also reported

103

observations of Bremsstrahlung, 2.223 MeV, and nuclear emission during the impulsive phase of the flare (Trottet et al. 1994; Trottet et al. 1993).

Figure 5.10 shows a lightcurve of the 11 June 1991 phase with both the Telescope and Burst modes of COMPTEL. The flare was subdivided into the three phases as defined by Rank (1996). Also included are the similar phases defined for an OSSE analysis (Murphy and Share 1999) and an EGRET/TASC analysis (Dunphy et al. 1999).

The following three tables (5.3, 5.4, and 5.5) list the times intervals used in the analysis of the 11 June 1991 event for the OSSE, EGRET TASC, and COMPTEL instruments respectively.

OSSE INTEGRATION INTERVALS	TIME (UT)	TIME (SEC)
I	01:58:46 - 02:07:30	7126 – 7650
II	02:07:30 - 02:11:52	7650 – 7913
III	02:11:52 - 02:23:53	7913 – 8634
IV	02:23:53 - 02:36:59	8634 – 9420

Table 5.4 - OSSE TIME INTERVALS for 11 JUNE 91

EGRET/TASC INTEGRATION INTERVALS	TIME (UT)	TIME (SEC)
I-1	01:59:15 – 02:03:06	7155 – 7386
I-2	02:03:06 – 02:09:39	7386 – 7779
Interphase	02:09:39 – 02:12:56	7779 – 7976
II	02:12:56 – 02:40:13	7976 – 9613

Table 5.5 - EGRET/TASC TIME INTERVALS for 11 JUNE 91

COMPTEL INTEGRATION INTERVALS	TIME (UT)	TIME (SEC)
Impulsive	01:54:54 - 02:07:11	6895 - 7632
Intermediate	02:07:11 - 02:14:17	7632 - 8058
Extended	02:14:17 - 02:54:00	8058 - 10440

Table 5.6 - COMPTEL TIME INTERVALS for 11 JUNE 91

The OSSE analysis used three techniques to compute the spectral index of the parent particle spectrum from the gamma ray measurements. They used the 6.13/1.63 MeV (^{16}O to ^{20}Ne) line flux ratio, the 0.511/4.44 MeV (positron decay to ^{12}C) line ratio and the 2.223/4.44 MeV (neutron capture to ^{12}C) line ratio. During Interval I (peak of the MeV emission), only the first two ratios were available (0.511/4.44 MeV and 2.223/4.44 MeV ratios). They both gave consistent power law indices indicating an unbroken power law from ~10 to ~100 MeV and with an index of ~4.5. All three methods were used in interval II but they did not yield consistent results. Murphy and Share (1999) suggested that this indicates the power law is broken and that there are possibly two separate particle populations, one hard and one soft. We will return to this point later. Interval III (peak of the >16 MeV emission) has a harder index than that I of about 3.2. The consistency of all three methods again indicate an unbroken proton power law from about 2 to > 100 MeV. The emission > 16 MeV is consistent with Pion decay. In the last phase (Interval IV) during the decay of the flare the three techniques do not agree. This is again possibly due to two components, a hard and soft. The hard component is consistent with the high-energy emission seen by the EGRET spark chamber.

The analysis of the EGRET/TASC data by Dunphy et al. (1999) again breaks the flare into four intervals. Their first two phases, I-1 and I-2 correspond to the two peaks in the impulsive phase. Analysis of phase I using the 2.223/4-7 MeV ratio gives a spectral index of ~4, consistent with OSSE. During phase I there is significant 2.0-2.4 MeV and 4.0-8.4 MeV emission but the > 30 MeV emission is consistent with zero. The interphase does not allow for the calculation of a spectral index because only the 2.0-2.4 MeV emission is significant. Phase II gives a spectral index of 3.35±0.10, which is consistent with the value of 3.2, derived by OSSE. All of the significant > 30 MeV emission is during phase II and is consistent with the previous assumptions of a pion component.
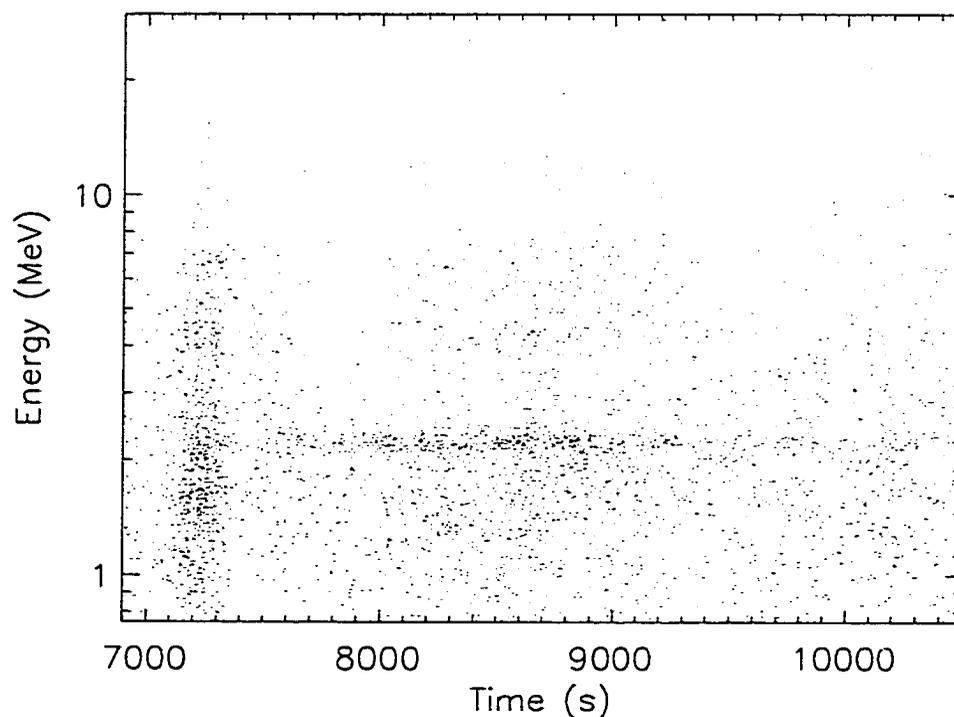
Figure 5.14 – COMPTEL event data for the 11 JUNE 91 flare from 6895 s to 10440 s.

106

Before looking at a detailed analysis of the COMPTEL observations it is useful to look at the event data for the flare and the event data for one of the four background intervals for comparison. Figure 5.11 shows the COMPTEL telescope event data for the full time interval, containing the impulsive, intermediate, and extended phases defined for the COMPTEL analysis. The event data for the flare show the three distinct phases of the flare. There is strong excess through all energies during the impulsive phase. During the intermediate phase the emission is dominated by events around 2.2 MeV and lower, with a lack of emission above 4 MeV. The greater than 4 MeV emission, especially the greater than 8 MeV emission is strong again in the extended phase. The other
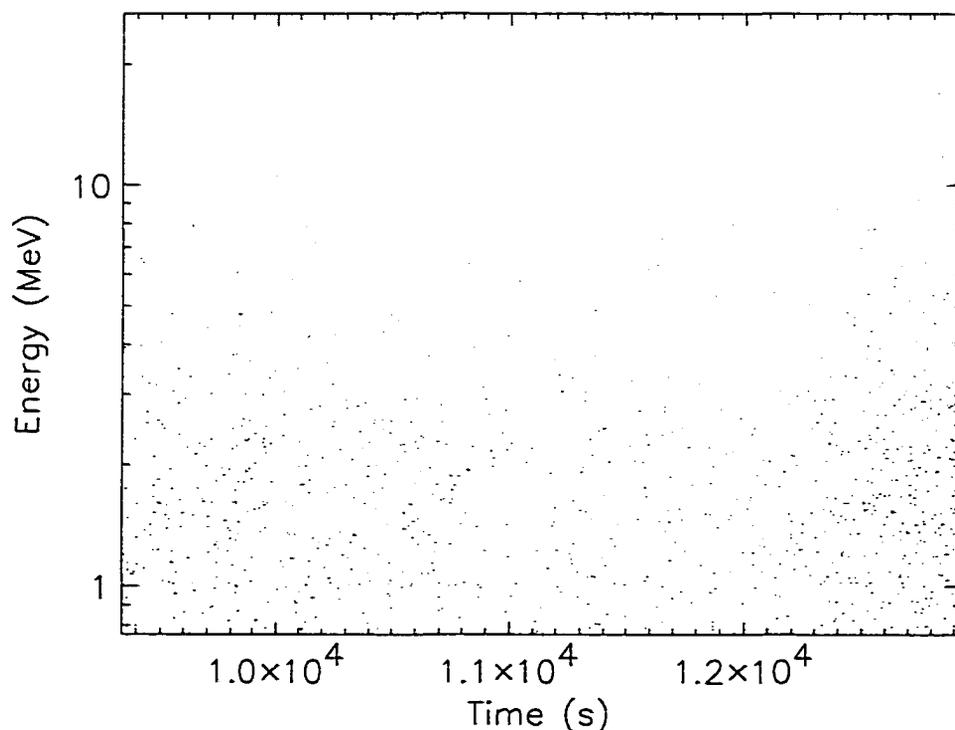
Figure 5.15 - COMPTEL event data 15 orbits before the 11 JUNE 91 flare.

107

strong feature in the data is the persistence of the 2.2 MeV emission through the entire event. Figure 5.12 shows the data for one of the four background intervals, containing data from 15 orbits before the flare. These data show the general random distribution of the background events at all energies except at energies above about 8 MeV were there are almost no background events. These event data (full source and 4 background sets) were then binned in energy space into 128 bins. The resulting background subtracted count spectrum is shown in figure 5.13.
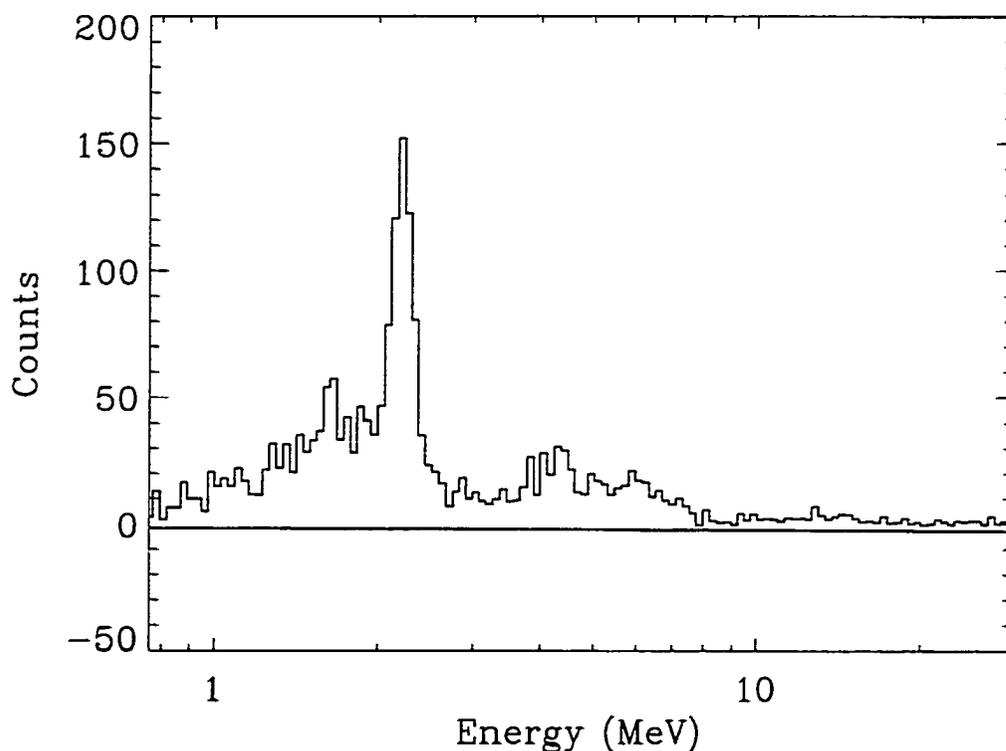
Figure 5.16 - COMPTEL background subtracted energy loss spectrum for the entire 11 JUNE 91 flare.

The energy loss spectrum contains strong line features at 1.63, 2.2, 4.4 and 6.1 MeV. Next this spectrum was deconvolved with the telescope response generated for the 11 June 1991 flare (based on its location within the COMPTEL FoV). Figure 5.14 is the photon flux spectrum for the full flare. Included in the plot is the best fit model composed of the 19 flare SMM broad line template (Share and Murphy 1995), a power law for the electron Bremsstrahlung component (determined with BATSE data and PHEBUS (Trottet et al. 1993)), the 10 strongest narrow lines (based on flare modeling) and another power law to account for pion decay secondary Bremsstrahlung. Table 5.7 is of the fitted energies and fluences for the 10 strongest lines in the full 11 June 1991 flare.

Energy (MeV)	Fluence (photons cm-2)
1.05±0.03	2.19±0.47
1.33±0.03	2.61±0.43
1.62±0.02	4.74±0.94
1.84±0.07	3.19±0.6
2.22±0.01	21.66±3
2.89±0.23	0.5±0.12
4.34±0.06	3.51±1.46
5.04±0.13	1.17±0.23
6.0±0.19	1.99±0.4
6.84±0.34	1.44±0.3

Table 5.7- The fitted energies and fluences for the 10 strongest lines in the full 11 June 1991 flare.

109
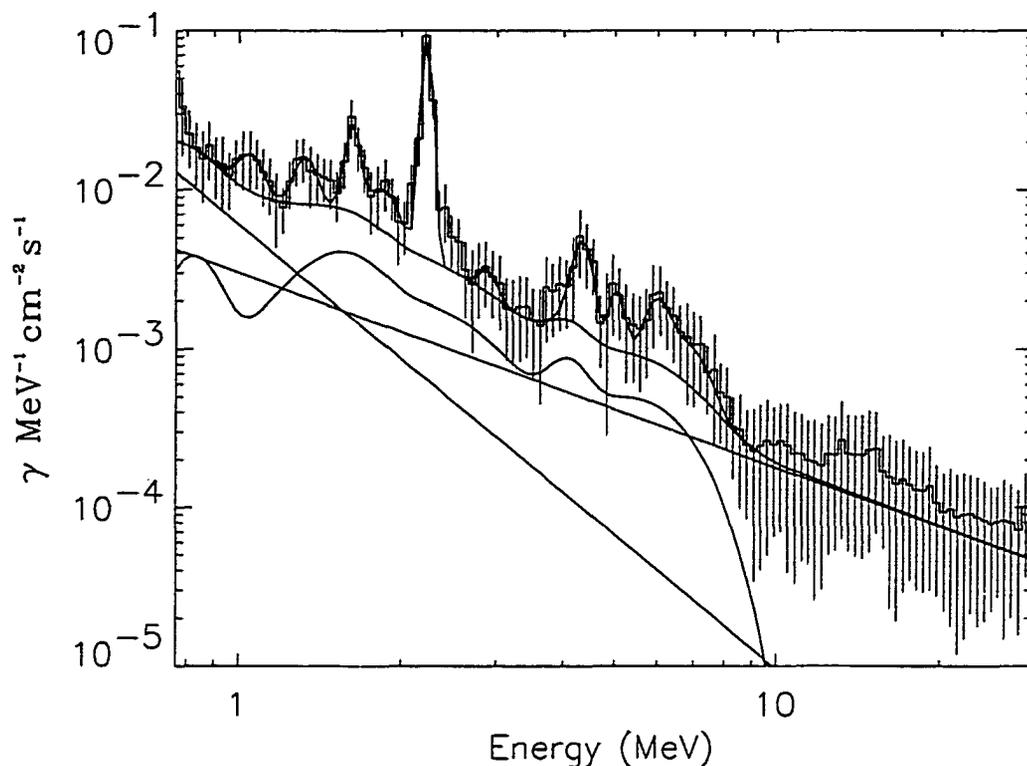
Figure 5.17 - COMPTEL flux spectrum for the entire 11 JUNE 91 flare.

We have separately analyzed the data for each of the 3 phases (impulsive, intermediate, and extended) defined in table 5.5 (See also Figure 5.13). The impulsive and intermediate phases are more difficult to analyze because of low statistics due to their short time intervals and high dead time. Figures 5.15 and 5.16 contain plots of the deconvolved photon flux for the impulsive and intermediate phases, respectively. The impulsive phase contains some evidence for line emission at ~1, 1.63, 4.4 and 6.1 MeV with a relatively small amount of 2.2 MeV emission. The short intermediate phase between the

110

impulsive and extended phases is very different from the phase before. Except
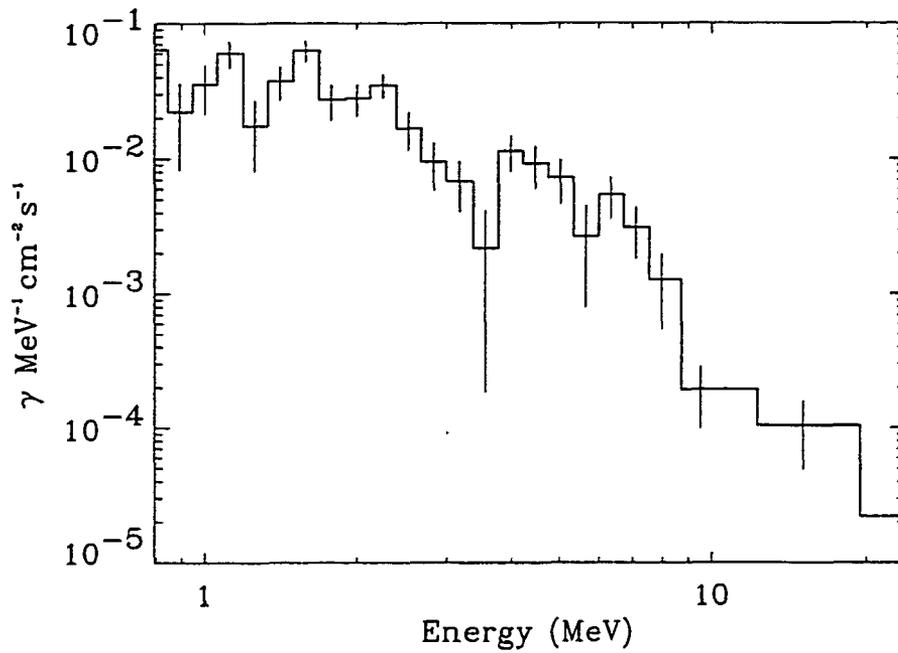
Figure 5.18 - COMPTEL flux spectrum for the impulsive phase of the 11 JUNE 91 flare.
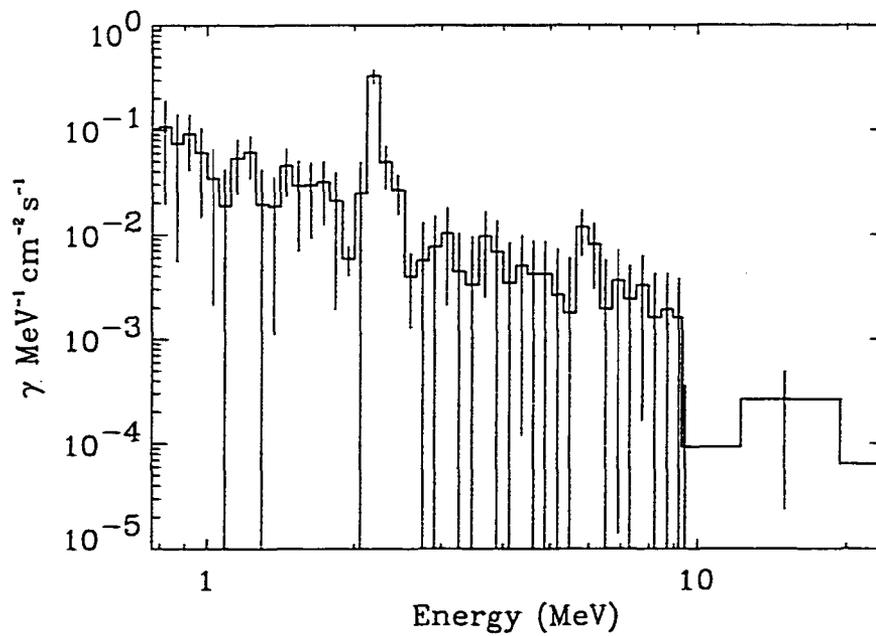
Figure 5.19 - COMPTEL flux spectrum for the intermediate phase of the 11 JUNE 91 flare.

111

for a line around 6 MeV there is little emission between 4-7 MeV. There is emission below 2 MeV round 1 and 1.6 MeV. The most striking feature is the 2.2 MeV line. This line is strong, dominating all other emission during this phase. The last phase, the extended phase is plotted in Figure 5.20. The spectrum has emission that is very similar to the full flare shown in Figure 5.17. As was done in
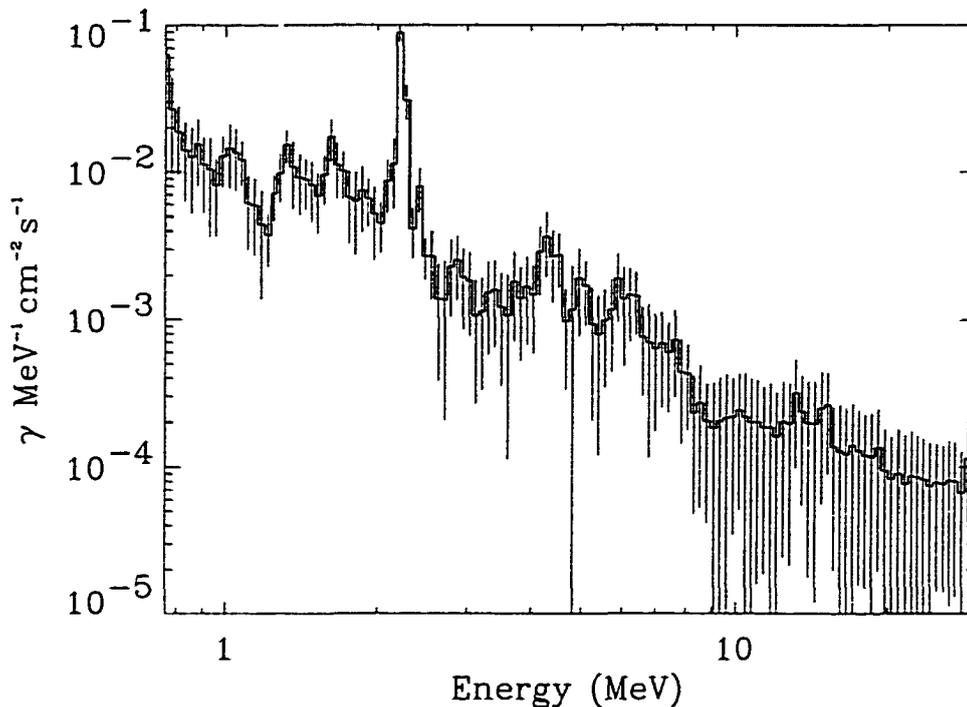
Figure 5.20 - COMPTEL flux spectrum for the extended phase of the11 JUNE 91 flare.
the OSSE and EGRET analysis of the flare we calculated ratios of specific line

fluences to obtain an estimate of the parent proton spectrum's shape. We

calculated the 2.2/4.4 MeV and 1.6/6.1 MeV fluence ratios for all three phases. In

addition we were able to calculate the 4.4+6.1/5.3 MeV fluence ratio. The fluence

ratios and the corresponding estimated spectral indices are shown in Table 5.7.

112

Phase of the	Fluence Ratio Type	Ratio	Power law index
Impulsive	1.63-to-6.13 MeV	2.34±0.97	5±0.5
	2.22-to-4.44 MeV	2.43±1.08	4.7±1
Intermediate	1.63-to-6.13 MeV	2.27±1.18	4.7±1
	2.22-to-4.44 MeV	30.3±10.37	2±0.5
Extended	1.63-to-6.13 MeV	1.51±0.44	3.8±0.5
	2.22-to-4.44 MeV	5.97±1.47	4±0.5
	4.4+6.1-to-5.3 MeV	6.2±0.86	3.8±0.1

Table 5.8 – Fluence ratios and the corresponding proton spectral indices for the impulsive, intermediate and extended phases of the 11 June 1991 flare.

The difficult interval to explain is the Intermediate (Rank 1996) or Interphase (Murphy and Share 1999, Dunphy et al. 1999) immediately following the peak of the impulsive phase. All three analysis of this flare using COMPTEL, OSSE and EGRET data obtained a hard proton spectrum with an index around 2 using the 2.2 to 4-7 MeV fluence ratio. This hard a spectrum would suggests the possible presence of a high energy Pion component above 8 MeV and an emission line at 5.3 due to spallation of C and O. However, none of the three instruments observed such a component. Murphy and Share (1999) argued that the inconsistencies in their measurements, in the interphase (II) and IV, indicate a two-component spectrum. Though this is plausible for the extended interval (IV), we do not agree with this conclusion for the interphase (II). We contend that this interval only contains a soft spectrum. If it did contain a hard spectrum, we would expect to see significant emission at 5.3 MeV and above 8 MeV. This is not seen in OSSE, EGRET/TASC, and not by the more sensitive instrument COMPTEL.

113

Determining the amount of expected charged pion component in the data with the COMPTEL data is difficult but we can estimate the expected amount of emission at 5.3 MeV. We were not able to fit a line at 5.3 MeV in the intermediate phase spectrum but we can estimate an upper limit for the emission. An upper limit for the measured emission at 5.3 MeV is 0.046 γ cm^{-2}. If the parent proton spectrum was very hard with a spectra index of 2 (as indicated by 2.2-to-4.4 fluence ratio) then based on the measured 4.44 and 6.13 MeV flux we would expect a fluence of 0.28$\pm$0.07 γ cm^{-2} (Ramaty et al 1996; Mandzhavidze and Ramaty 2000). On the other hand, the softer proton spectrum of 5 (indicated by the 1.6/6.1 MeV fluence ratio) would produce a fluence of 0.06$\pm$0.02 γ cm^{-2}. So the upper limit on the 5.3 MeV fluence is consistent with the softer proton spectrum.

We contend that the reason a hard spectrum is indicated by the 2.223-to-4.44 ratio is simply an indication of the inability of the ratio to give reliable results and its double valueness in this regime. The ratio turns up sharply because when the spectrum is soft the only neutron production channel is the p and α on CNO process. At these lower energies, the ratio turns up because the production of neutrons continues in this channel but the production of lines from CNO quickly turns off. So the ratio sharply turns up which is not accounted for in many of the published results

114

Another indicator of the soft spectrum comes from the study of the time decay of the 2.223 MeV line. The measurements from COMPTEL have been used to model (Rank 1996) the 2.223 MeV emission with a decay constant of τ=230 s (long compared to the average 100 s). The time constant τ can be defined as (Prince et al. (1983)),

$$\tau = \left[\frac{1}{\tau_H} + \frac{1}{\tau_{He}} + \frac{1}{\tau_d} \right]^{-1} ; \tau_H = \frac{1.4 \cdot 10^{19}}{n_H} s; \tau_{He} = \frac{8.5 \cdot 10^{14}}{r \cdot n_H} s$$

where τ_H is the capture time on hydrogen, τ_{He} is the capture time on ^{3}He, τ_d is the neutron decay time, n_H is the hydrogen number density, and r is the ^{3}He/H ratio. τ is maximum when r = 0 (no competing radiation less capture on ^{3}He). So if we set r = 0 and solve for n_H when τ = 230 s we find that n_H = $4.56 \cdot 10^{16}$ cm-3. This corresponds to a depth above the base of the photosphere of about 170 km (Fontenla et al. 1993). For an average r of $5 \cdot 10^{-05}$ (Prince et al. 1983) the depth of would be about 50 km above the photosphere's base. These calculations suggest that the capture time of 230 s means neutrons are being captured higher up in the photosphere. For neutrons to be captured at a point of lower hydrogen density and higher height in the photosphere they would have to be of lower energy or travelling at a shallow angle in the atmosphere. The existence of low energy neutrons would indicate that the proton spectrum during this part of the flare was soft not hard. So given the indication of a soft spectrum in terms of unambiguous line ratios and the extremely long 2.223 MeV decay the most

115

plausible explanation for the proton spectrum during the interphase is that it has a very soft spectrum.

Discrete 2.223 MeV Decay Model

Now that we feel strongly that the interphase has a very soft proton spectrum we can use that information to obtain other information, namely we can estimate the ^{3}He content of the photosphere. What we will use is the neutron thermalization obtained at the end of chapter IV. This will allow us to calculate the distribution of thermal neutrons in the solar atmosphere and then calculate the neutron absorption rate and decay time using a model for the density distribution for the lower chromosphere and the photosphere (Fontenla et al. 1993). Previous calculations of the ^{3}He content in the photosphere have not used information about the spatial distribution of the thermal neutrons. They only used a single average depth and so a single atmosphere density to calculate the ^{3}He/H ratio. We will now use our calculations of neutron transport to calculate a more realistic ratio using the spatial distribution of the thermal neutrons.

Since the protons spectrum is soft, the neutron spectrum is dominated by low energy neutrons (<10 MeV). This allows the use of the analytical neutron transport outlined in chapter IV because we do not have to worry about inelastic scattering. Since the low energy neutrons are created mainly by p and alpha on CNO we assume an evaporation neutron spectrum (Lingenfelter and Ramaty 67) of the form,

$$f(E) = \frac{E}{\theta^2} \exp(\frac{-E}{\theta}),$$

116

where E is the neutron energy and θ is the temperature of the excited nucleus,

~1.5 MeV. This spectrum is peaked around 2 MeV so the energy of the neutrons is chosen to be an impulse at 2 MeV. This starting energy for thermal neutrons corresponds to lethargy of 15. As we stated in chapter IV, the distribution is insensitive to lethargies around 10 or greater. In addition, we showed that the distribution of thermal neutrons is clustered around the first several mean free paths. Neutrons produced at the bottom of the chromosphere or top of the
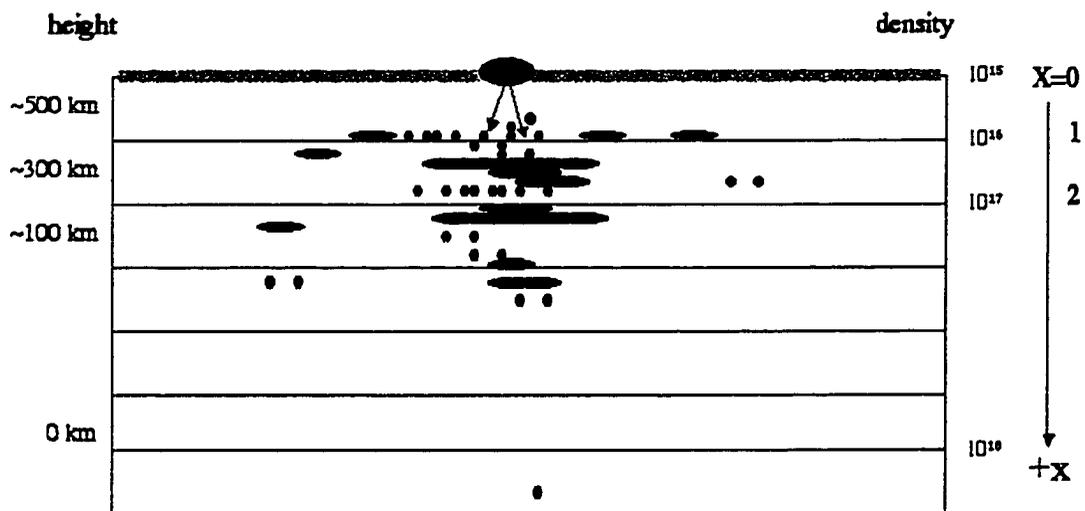
Figure 5.21 – A cartoon of solar flare neutrons hitting the top of the photosphere and thermalizing in a stratified atmosphere. The left side of the figure shows the height of the photosphere relative to a zero point where the optical depth (optical light) in the photosphere is unity. The right shows the hydrogen number density and the neutron optical depth for the layers.

photosphere would not see material until around an altitude of 500 km in the photosphere. Above this point, the densities are such that a neutron would have a mean free path of several thousand km. At around 500 km, the first density plateau in the photosphere starts at a hydrogen density of about 10^{15} cm^{-3}. Here

117

the mean free path of the neutron is a few hundred km. The next density level at 300 km is about 10^{16} cm^{-3}. Here the neutrons have average mean free paths on the order of tens of km. By 100 km, the density levels out at 10^{17} cm^{-3} and increases much more slowly to 10^{18} cm^{-3} at the 0 km mark where the optical depth of one defines the base of the photosphere. Therefore, thermal neutrons from the lower energy neutrons cluster around the layers at 500, 300 and 100 km with decreasing neutron density (see cartoon in Figure 5.21). Using the distribution for thermal neutrons we calculated, we then have the fraction of neutrons at these three levels. If we start by assuming there is no ^{3}He we can compute the decay time at each of these three levels and weight their sums by
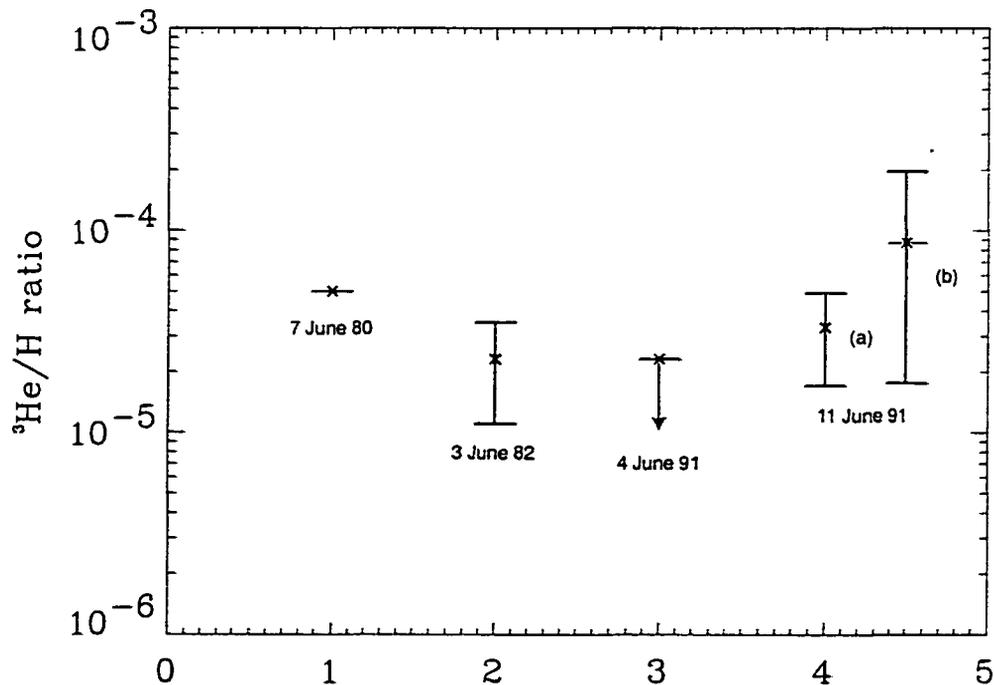
Figure 5.22 – ^{3}He/H ratios for 2 June 1980 (Chupp et al. 1981), 3 June 1982 (Hua and Lingenfelter 1987), 4 June 1991 (Murphy et al. 1997), and 11 June 1991 (a) (Rank 1996) and (b) this work.

118

the fraction of thermal neutrons at each level. This gives us a neutron capture time of 473 s. This is clearly too high so we can calculate how much ^{3}He is needed to obtain the corrected time calculated from the COMPTEL data (Rank 1996). The value obtained from COMPTEL is 230 s with a 1 σ range of 140-390 s. This gives a ^{3}He/H ratio of 8.7e-05 with a 1 σ range of 1.96e-04 to 1.75e-05.

Previous values that have been reported are 5e-05 (no error reported) for the 7 June 1980 flare (Chupp et al. 1981), (2.3±1.2)e-05 for the 3 June 1982 flare (Hua and Lingenfelter 1987), 2.3e-05 (2 σ upper-limit) for the 4 June 1991 flare (Murphy et al. 1997) and (3.0±1.6)e-05 for this flare (Rank 1996). The distribution of these values is shown in Figure 5.22.

Conclusions

The purpose of this work is to present an explanation of the puzzle presented by the spectral observations by CGRO of the intermediate phase of the 11 June 1991 solar flare. Analysis of observations by OSSE (Murphy and Share 1999), COMPTEL (Rank 1996) and EGRET (Dunphy et al. 1999) using standard spectroscopy methods indicates the presence of both a hard and a soft parent proton spectrum. We present a fine-tuning of and application of a new spectroscopy technique to the COMPTEL observations. We then show that the theoretically expected emission from a hard proton spectrum is not observed by COMPTEL. We conclude that the lack of this predicted emission and the longer than normal 2.223 MeV emission decay time (Rank 1996) can only be due to a soft parent proton spectrum. This means that the region of 2.223/4-7 MeV

119

fluence space is largely unexplored for soft proton spectra. The use of this ratio must be reexamined for proton spectra with indices greater than 5 or 6. We then apply a model we developed for the transport of neutrons created from a soft proton spectrum to determine the photospheric ^{3}He abundance during this flare. We calculated a ^{3}He/H ratio of 8.7e-05 with a 1 σ range of 1.96e-04 to 1.75e-05 for this flare using this new model. This is larger than all previous values reported.

In addition we present an additional flare observation from COMPTEL. In response to a BACODINE cosmic gamma-ray burst alert, COMPTEL on the CGRO recorded gamma rays above 1 MeV from the C4 flare at 0221 UT 20 January 2000. This event, though at the limits of COMPTEL's sensitivity, clearly shows a nuclear line excess above the continuum. Using the new spectroscopy techniques we are able to resolve individual lines. This has allows us to make a basic comparison of this event with the GRL flare distribution from SMM and also compare this flare with a well-observed large GRL flare seen by OSSE. We show that this flare is normal, i.e., it is a natural extension of the SMM distribution of flares. The analysis of this flare means there is no evidence for a lower flare size for proton acceleration. Protons even in small flares contain a large part of the accelerated particle energy.

REFERENCES

1. Achterberg, A. and C.A. Norman, *Particle acceleration by shock waves in solar flares.* Astronomy and Astrophysics, 1980. **89**: p. 353-362.

2. Anastasiadis, A. and L. Vlahos, *Particle Acceleration in An Evolving Active Region by an Ensemble of Shock Waves.* Astrophysical Journal, 1994. **428**(June 20): p. 819-826.

3. Arnoldy, R.L., S.R. Kane, and J.R. Winckler, *Energetic Solar Flare X-Rays Observed by Satellite and Their Correlation with Solar Radio and Energetic Particle Emission.* Astrophysical Journal, 1968. **151**: p. 711.

4. Axford, W. I., E. Leer, and G. Skadron. *Acceleration of Cosmic Rays by Shock Fronts.* in *International Conference of Cosmic Rays #15.* 1977.

5. Bai, T., *Two Classes of Gamma-Ray/Proton Flares: Impulsive and Gradual.* Astrophysical Journal, 1986. **308**: p. 912.

6. Bastian, T.T., A.O. Benz, and D.E. Gary, *Radio Emission from Solar Flares.* Ann. Rev. Astron. Astrophys., 1998. **36**: p. 131-188.

7. Beckurts, K.H. and K. Wirtz, *Neutron Physics.* 1964, New York: Springer. 444.

8. Blandford, R.D., *Particle Acceleration Mechanisms.* Astrophysical Journal (Suppl. Series), 1994. **90**(Feb): p. 515-520.

9. Brown, J.C. and D.F. Smith, *Solar flares.* Reports on Progress in Physics, 1980. **43**: p. 125-197.

10. Cane, H.V., R.E. McGuire, and T.T. von Rosenvinge, *Two Classes of Solar Energetic Particle Events Associated with Impulsive and Long-Duration Soft X-Ray Flares.* Astrophysical Journal, 1986. **301**: p. 448-459.

11. Cane, H.V., D.V. Reames, and T.T. von Rosenvinge, *Solar Particle Abundances at Energies of Greater than 1 MeV per Nucleon and the Role of Interplanetary Shocks.* Astrophysical Journal, 1991. **373**(June 1): p. 675-682.

12. Carrington, R.C., *Description of a Singular Appearance Seen in the Sun on September 1, 1859.* Monthly Notices of the Royal Astronomical Society, 1859. **20**: p. 13-15.

13. Chupp, E.L., et al., *Solar Gamma Ray Lines Observed During the Solar Activity of August 2 to August 11, 1972.* Nature, 1973. **241**: p. 333-335.

14. Chupp, E.L., *Gamma-ray Astronomy: Nuclear Transition Region.* Geophysics and astrophysics monographs, ed. B.M. McCormac. Vol. 14. 1976, Boston: Dordrecht:Reidel.

15. Chupp, E.L., et al., *Observation of the 2.223 MeV gamma-ray line on the SMM satellite - The event of 1980 June 7.* Astrophysical Journal Letters, 1981. **244**: p. 171.

16. Cliver, E.W., et al., *Solar Flare Nuclear Gamma-Rays and Interplanetary Proton Events.* Astrophysical Journal, 1989. **343**(Aug 15): p. 953-970.

17. Connors, A., *Confidence Intervals for MAP estimation method.,* Private Comm. 2000.

18. Cowan, G., *Statistical Data Analysis.* 1998, Oxford: Clarendon Press.

19. Craig, I.J.D. and J.C. Brown, *Inverse problems in astronomy: A guide to inversion strategies for remotely sensed data.* 1986, Bristol, England and Boston, MA: Adam Hilger, Ltd. 159.

20. de Jager, C. . in *COSPAR Symp. on Solar Flares and Space Research.* 1969: D.

122

Reidel Publ. Co.

21. Dennis, B.R., *Solar Hard X-Ray Bursts*. Solar Physics, 1985. **100**: p. 465-490.

22. Dennis, B.R., *Solar Flare Hard X-Ray Observations*. Solar Physics, 1988. **118**: p. 49-94.

23. Dodson, H.W. and R.E. Hedeman, *The Proton Flare of August 28, 1966*. Solar Physics, 1968. **4**: p. 229.

24. Dolan, J.F. and G.G. Fazio, *Gamma Ray Spectrum of the Sun*. Astronomical Journal, 1964. **69**.

25. Dunphy, P.P., *et al.*, *Gamma-Rays and Neutrons as a Probe of Flare Proton Spectra: The Solar Flare of 11 June 1991*. Solar Physics, 1999. **187**: p. 45-57.

26. Eddy, J.A. *The new solar physics*. 1978. Washington: Westview Press.

27. Efron, B. and R.J. Tibshirani, *An Introduction to the Bootstrap*. 1993, New York: Chapman & Hall.

28. Ellison, D.C. and R. Ramaty, *Shock acceleration of electrons and ions in solar flares*. Astrophysical Journal, 1985. **298**: p. 400-408.

29. Fermi, E., *On the Origin of the Cosmic Radiation*. Physical Review, 1949. **75**(No. 8): p. 1169-1174.

30. Fishman, G.J., *et al. BATSE: The Burst and Transient Source Experiment on the Gamma Ray Observatory*. in *Proceedings of the Gamma Ray Observatory Science Workshop*. 1989. Goddard Space Flight Center, Greenbelt, MD: NASA.

31. Fisk, L.A., *^{3}He-Rich Flares: A Possible Explanation*. Astrophysical Journal, 1978. **224**(Sept 15): p. 1048-1055.

32. Fletcher, L., *Numerical Simulations of Coronal Particle Trapping*. Astronomy and Astophysics, 1997. **326**: p. 1259-1267.

33. Fontenla, J.M., E.H. Avrett, and R. Loeser, *Energy balance in the solar transition region. III - Helium emission in hydrostatic, constant-abundance models with diffusion*. Astrophysical Journal, 1993. **406**: p. 319.

34. Forbes, T.G., *A review on the genesis of coronal mass ejections*. Journal of Geophysical Research, 2000. **105**(A10): p. 23,153-23,165.

35. Gehrels, N., E. Chipman, and D.A. Kniffen, *The Compton Gamma Ray Observatory*. Astronomy and Astrophysics (Suppl. Ser.), 1993. **97**: p. 5-12.

36. Gelman, A., *Bayesian Data Analysis*. 1995, New York: Chapman & Hall. 526.

37. Golub, L. and J.M. Pasachoff, *The Solar Corona*. 1997, Cambridge and New York: Cambridge University Press.

38. Gubchenko, V.M. and V.V. Zaitsev, *On Proton and Electron Acceleration by Shock Waves During Large Solar Flares*. Solar Physics, 1979. **63**: p. 337-352.

39. Gull, S.F. and G.J. Daniell, *Image Reconstruction from Incomplete and Noisy Data*. Nature, 1978. **272**: p. 686-690.

40. Gull, S.F. and J. Skilling, *the MEMSYS5 User's Manual*, . 1990, Maximum Entropy Data Consultants Ltd: Royston.

41. Hansen, P.C., *Rank-Deficient and Discrete Ill-Posed Problems*. 1998, Philadelphia: Siam.

42. Hey, J.S., *Solar radiations in the 2-6 metre radio wavelength band*. Nature, 1945. **157**: p. 47.

43. Heyvaerts, J., E.R. Priest, and D.M. Rust, *An emerging flux model for the solar flare phenomenon*. Astrophysical Journal, 1977. **216**: p. 123-137.

44. Hirayama, T. *Stochastic acceleration in the diffusion region and the structure of slow shocks in solar flares*. in *Proc. of Kofu Symposium*. 1994. Kofu: Nobeyama Radio

123

Observatory.

45. Hodgson, R., *On a curious Appearance seen in the Sun.* Monthly Notices of the Royal Astronomical Society, 1859. **20**.

46. Holman, G.D. and M.E. Pesses, *Solar type II radio emission and the shock drift acceleration of electrons.* Astrophysical Journal, 1983. **267**: p. 837-843.

47. Hua, X.-M. and R.E. Lingenfelter, *Solar Flare Neutron Production and the Angular Dependence of the Capture Gamma-Ray Emission.* Solar Physics, 1987. **107**: p. 351-383.

48. Hua, X.-M. and R.E. Lingenfelter, *A Determination of the ^{3}He/H Ratio in the Solar Photosphere From Flare Gamma-Ray Line Observations.* Astrophysical Journal, 1987. **319**(Aug 1): p. 555-566.

49. Hulot, E., N. Vilmer, and G. Trottet, *Relative Timing of Solar Prompt g-ray Line and X-ray Emission Expected from a Trap Plus Precipitation Model for Protons and Electrons.* Astronomy and Astrophysics, 1989. **213**: p. 383-396.

50. Isenberg, P.A., *On a difficulty with accelerating particles at slow-mode shocks.* Journal of Geophysical Research, 1986. **91**: p. 1699.

51. Kallenrode, M.B., et al. . in *20th International Cosmic Ray Conference.* 1987.

52. Kanbach, G., et al., *Detection of a long-duration Solar Gamma-Ray Flare on June 11, 1991 with EGRET on COMPTON - GRO.* Astronomy and Astrophysics (Suppl. Series), 1993. **97**: p. 349-353.

53. Kappadath, S.C., *Measurement of the Cosmic Diffuse Gamma-Ray Spectrum from 800 keV to 30 MeV*, in *Physics.* 1998, University of New Hampshire: Durham, NH.

54. Knoll, G.F., *Radiation Detection and Measurement.* 2nd ed. 1989, New York: John Wiley and Sons, Inc. 831.

55. Koch, H.W. and J.W. Motz, *Bremsstrahlung Cross-Section Formulas and Related Data.* Reviews of Modern Physics, 1959. **31**(No. 4 October): p. 920-955.

56. Kocharov, L.G. and G.A. Kovaltsov. *Acceleration of Particles by an Ensemble of Shock Waves and High Energy Emission of Solar Flares.* in *Particle Acceleration in Cosmic Plasmas.* 1992. Newark, DE: AIP.

57. Kocharov , G.E., *Nuclear Processes in the Solar Atmosphere and the Particle Acceleration Problem.* ASTROPHYSICS AND SPACE PHYSICS REVIEWS, 1988. **6**: p. 315.

58. Kolaczyk, E.D., *Bayesian Multi-scale Models for Poisson Processes.* J. Amer. Statist. Assoc., 1999a. **94**: p. 920-933.

59. Kolaczyk, E.D., *Some observations on the tractability of certain multiscale models.* Bayesian Inference in Wavelet-Based Models, ed. M.A. Vidakovic. 1999b, New York: Springer-Verlag.

60. Kolaczyk, E.D., *Confidence Intervals for MAP estimation method*, Private Comm. 2000a.

61. Kolaczyk, E.D., *Bootstrapping Poisson Estimators*, Private Comm. 2000b.

62. Kuzhevskii, B.M., *Gamma astronomy of the sun and study of solar cosmic rays.* Soviet Physics-Uspekhi,, 1982. **25**: p. 392-408.

63. Lang, K.R., *Astrophysical formulae.* Astronomy and astrophysics library. 1999, New York: Springer, 1999.

64. LaRosa, T.N., R.L. Moore, and S.N. Shore, *A New Path for the Electron Bulk Energization in Solar Flares: Fermi Acceleration by Magnetohydrodynamic Turbulence in Reconnection Outflows.* Astrophysical Journal, 1994. **425**(Apr 20):

p. 856-860.

65.LaRosa, T.N., et al., New Promise for Electron Bulk Energization in Solar Flares: Preferential Fermi Acceleration of Electrons over Protons in Reconnection-Driven Magnetohydrodynamic Turbulence. Astrophysical Journal, 1996. **467**(Aug 10): p. 454-464.

66.Lee, M.A.V., Heinrich J., Damping and Non-Linear Wave-Particle Interactions of Alfvén-Waves in the Solar Wind. Astrophysics and Space Science, 1973. **24**: p. 31.

67.Lee, M.A. Stochastic Fermi Acceleration and Solar Cosmic Rays. in High-Energy Solar Phenomena—A New Era of Spacecraft Measurements. 1994. Waterville Valley, New Hampshire: AIP: New York.

68.Lingenfelter, R.E. and R. Ramaty. High energy nuclear reactions in solar flares. in High energy nuclear reactions in astrophysics. 1967: W. A. Benjamin.

69.Litvinenko, Y.E., Particle Acceleration in Reconnecting Current Sheets with a Nonzero Magnetic Field. Astrophysical Journal, 1996. **462**: p. 997-1004.

70.Mallat, S., A Wavelet Tour of Signal Processing. 1998, San Diego: Academic Press.

71.Mandzhavidze, N. and R. Ramaty. Particle Acceleration and Abundances from Gamma-Ray Line Spectroscopy. in High Energy Solar Physics Workshop - Anticipating HESSI. 2000: Astronomical Society of the Pacific.

72.McClements, K.G.B., R.; Su, J. J.; Dawson, J. M.; Spicer, D. S., Lower hybrid resonance acceleration of electrons and ions in solar flares and the associated microwave emission. Astrophysical Journal, 1993. **409**(1): p. 465-475.

73.McConnell, M. An Overview of Solar Flare Results from COMPTEL. in High-Energy Solar Phenomena—A New Era of Spacecraft Measurements. 1994. Waterville Valley, New Hampshire: AIP: New York.

74.McInerney, J.J., Nuclear Science and Engineering, 1963. **17**: p. 392.

75.McInerney, J.J., Nuclear Science and Engineering, 1965. **22**: p. 215.

76.Melrose, D.B. and J.C. Brown, Precipitation in Trap Models for Solar Hard X-Ray Bursts. Monthly Notices of the Royal Astronomical Society, 1976. **176**: p. 15-30.

77.Melrose, D.B., Tubulent Acceleration in Solar Flares. Astrophysical Journal (Suppl. Series), 1994. **90**(February): p. 623-630.

78.Miller, J.A. and R. Ramaty. Stochastic acceleration in impulsive solar flares. in Particle Acceleration in Cosmic Plasmas. 1992. Newark, Delaware: AIP.

79.Miller, J.A.R., D. Aaron, Stochastic Proton Acceleration by Cascading Alfven Waves in Impulsive Solar Flares. Astrophysical Journal, 1995. **452**: p. 912.

80.Miller, J.A. and D.V. Reames. Heavy Ion Acceleration by Cascading Alfvén Waves in Impulsive Solar Flares. in High Energy Solar Physics. 1996. Greenbelt, MD: AIP.

81.Miller, J.A.L., T. N.; Moore, R. L., Stochastic Electron Acceleration by Cascading Fast Mode Waves in Impulsive Solar Flares. Astrophysical Journal, 1996. **461**: p. 445.

82.Miller, J.A., et al., Critical issues for understanding particle acceleration in impulsive solar flares. Journal of Geophysical Research, 1997. **102**(A7): p. 14631-14660.

83.Morris, D.J. and P. Xu, Inegrated Spacecraft Mass as Viewed from the COMPTEL Burst Modules, . 1983, University of New Hampshire: Durham, NH.

84.Murphy, R.J., et al., Nuclear Line Spectroscopy of the 1981 April 27 Solar Flare. Astrophysical Journal, 1990. **358**: p. 298-312.

85.Murphy, R.J., et al., Solar Abundances from Gamma-Ray Spectroscopy: Comparisons with Energetic Particle, Photospheric, and Coronal Abundances. Astrophysical Journal, 1991. **371**: p. 793-803.

125

86. Murphy, R.J., et al. OSSE Observations of Solar Flares. in Compton Gamma-Ray Observatory Workshop. 1993. St. Louis: AIP: New York.

87. Murphy, R.J., et al., Accelerated Particle Composition and Energetics and Ambient Abundances from Gamma-Ray Spectroscopy of the 1991 June 4 Solar Flare. Astrophysical Journal, 1997. 490: p. 883-900.

88. Murphy, R.J., Accelerated Particle Composition and Energetics and Ambient Abundances from Gamma-Ray Spectroscopy of the 1991 June 4 Solar Flare: Erratum. Astrophysical Journal, 1998. 500: p. 523.

89. Murphy, R.J. and G.H. Share. Accelerated-Particle Spectral Variability in the 1991 June 11 Solar Flare. in The Fifth Compton Symposium. 1999. Portsmouth, NH: American Institute of Physics.

90. Murphy, R., OSSE SOLAR FLARE OBSERVATIONS , . 2000.

91. Nakajima, H., et al., A High-Speed Shock Wave in the Impulsive Phase of the 1984 April Flare. Astrophysical Journal (Suppl. Series), 1990. 73(June): p. 177-183.

92. Nowak, R.D., Multiscale Hidden Markov Models for Bayesian Image Analysis, . 1998, Michigan State University.

93. Nowak, R.D. and E.D. Kolaczyk. A Bayesian multiscale framework for Poisson inverse problems. in Proceedings of the IEEE International Conference on Acoustics, Speech, and Signal Processing. 1999.

94. Pallavicini, R., S. Serio, and G.S. Vaiana, A Survey of Soft X-Ray Limb Flare Images: The Relation Between their Structure in the Corona and Other Physical Parameters. Astrophysical Journal, 1977. 216: p. 108-122.

95. Parker, E.N., Acceleration of Cosmic Rays in the Solar Flares. Physical Review, 1957. 107((3)): p. 830-836.

96. Peterson, L.E. and J.R. Winckler, Gamma-Ray Burst From a Solar Flare. Journal of Geophysical Research, 1959. 64(No. 7 July): p. 697-707.

97. Press, W.T., et al., Numerical Recipes in FORTRAN. 2nd ed. 1992, New York: Cambridge University Press.

98. Priest, E. and T. Forbes, Magnetic reconnection : MHD theory and applications. 2000, New York: Cambridge University Press.

99. Prince, T.A., et al. The Time History of 2.22 MeV Line Emission in Solar Flares. in 18th International Cosmic Ray Conference. 1983. Bangalore, India.

100. Ramaty, R., B. Kozlovsky, and R.E. Lingenfelter, Solar Gamma Rays. Space Science Reviews, 1975. 18: p. 341-388.

101. Ramaty, R., R.J. Murphy, and C.D. Dermer, On the Origin of the Pion-Decay Radiation in the 1982 June 3 Solar Flare. Astrophysical Journal (Letters), 1987. 316: p. L41-L44.

102. Ramaty, R., N. Mandzhavidze, and B. Kozlovsky. Solar Atmospheric Abundances from Gamma Ray Spectroscopy. in Proceedings of the High Energy Solar Physics Workshop. 1996: AIP: New York.

103. Rank, G., Gamma Rays and Neutrons of the Solar Flares on 11 and 15 June 1991 Measured with COMPTEL, . 1996, Technical University of Munich. p. 115.

104. Rieger, E., Solar Flares: High-Energy Radiation and Particles. Solar Physics, 1989. 121: p. 323-345.

105. Ryan, J.M., Particle Propagation Effects on Solar Flare X- and g-Ray Time Profiles. Solar Physics, 1986. 105: p. 365-382.

106. Ryan, J.M. and M.A. Lee, On the Transport and Acceleration of Solar Flare Particles in a Coronal Loop. Astrophysical Journal, 1991. 368: p. 316-324.

107. Ryan, J., et al. COMPTEL Gamma Ray and Neutron Measurements of Solar Flares.

in *Compton Gamma-Ray Observatory Workshop.* 1993. St. Louis: AIP: New York.

108. Ryan, J.M., *Long Duration Solar Gamma-Ray Flares.* Space Science Reviews, 1999. **accepted.**

109. Schneid, E.J., et al. *EGRET Observations of Extended High Energy Emissions from the Nuclear Line Flares of June 1991.* in *High-Energy Solar Phenomena—A New Era of Spacecraft Measurements.* 1994. Waterville Valley, New Hampshire: AIP: New York.

110. Schönfelder, V., et al., *Instrument Description and Performance of the Imaging Gamma-Ray Telescope COMPTEL Aboard the Compton Gamma-Ray Observatory.* Astrophysical Journal Supplement Series, 1993. **86**: p. 657-692.

111. Share, G.H. and R.J. Murphy, *Gamma-Ray Measurements of Flare-to-Flare Variations in Ambient Solar Abundances.* Astrophysical Journal, 1995. **452**: p. 933.

112. Share, G.H. and R.J. Murphy. *Gamma-Ray Measurement of Energetic Heavy Ions at the Sun.* in *26th ICRC.* 1999. Salt Lake City.

113. Sneddon, I.N., *Fourier Transforms.* International Series in Pure and Applied Mathematics. 1951, New York: McGraw-Hill. 542.

114. Southworth, G.C., *Microwave radiation from the sun.* J. Franklin Institute, 1944. **239**: p. 285.

115. Speiser, T.W., *Particle Trajectories in Model Current Sheets.* Journal of Geophysical Research, 1965. **70**(17): p. 4219-4226.

116. Starck, J.-L., F. Murtagh, and A. Bijaoui, *Image Processing and Data Analysis: The Multiscale Approach.* 1998, New York: Cambridge University Press.

117. Sturrock, P., *Flare Models,* in *Solar Flares A Monograph from the Solar Skylab Workshop II,* P.A. Sturrock, Editor. 1980, Colorado Associated University Press: Boulder. p. 411-449.

118. Suleiman, R., et al. *COMPTEL'S Solar Flare Catalog.* in *High-Energy Solar Phenomena - A New Era of Spacecraft Measurements.* 1994. Waterville Valley, NH: AIP: New York.

119. Svestka, Z., *Solar Flares.* Vol. 8. 1976, Dordrecht: Dordrecht:Reidel. 399.

120. Tanaka, T. *Activity in Red Dwarf Stars.* in *IAU Colloquia.* 1983.

121. Tanaka, K., *Impact of X-ray observations from the Hinotori satellite on solar flare research.* Publications of the Astronomical Society of Japan, 1987. **39**: p. 1-45.

122. Tandberg-Hanssen, E. and A.G. Emslie, *The physics of solar flares.* 1988, Cambridge and New York: Cambridge University Press. 286.

123. Temerin, M. and I. Roth. *Selective Enrichment of Energetic Ions in Impulsive Solar Flares.* in *High Energy Solar Physics.* 1996. Greenbelt, MD: AIP.

124. Thompson, D.J., et al., *Calibration of the Energetic Gamma-Ray Experiment Telescope (EGRET) for the Compton Gamma-Ray Observatory.* Astrophysical Journal (Suppl. Series), 1993. **86**: p. 629-656.

125. Timmermann, K.E. and R.D. Nowak, *Multiscale Modeling and Estimation of Poisson Processes with Application to Photon-Limited Imaging.* IEEE Transactions Infomation Theory, 1999. **45**(Special Issue on Multiscale Statistical Signal Analysis and Its Applications): p. 846-862.

126. Trottet, G., et al., *Temporal and Spectral Characteristics of the June 11, 1991 Gamma-Ray Flare.* Astronomy and Astrophysics, 1993. **97**(Astron. Astrophys. Suppl. Ser.): p. 337-339.

127. Trottet, G. *X-Ray and Gamma-Ray Observations of Solar Flares by GRANAT.* in

High-Energy Solar Phenomena—A New Era of Spacecraft Measurements. 1994. Waterville Valley, NY: AIP: New York.

128.Tsuneta, S. *Proc. of Japan-France Seminar on Active Phenomena in the Outer Atmosphere of the Sun and Stars.* 1983. CNRS and L'Observatorie de Paris, Paris, France.

129.Tsuneta, S. and T. Naito, *Fermi Acceleration at the Fast Shock in a Solar Flare and the Impulsive Loop-Top Hard X-Ray Source.* Astrophysical Journal Letters, 1998. **495**: p. L67.

130.van Dijk, R., *Gamma-Ray Observations of X-Ray Binaries with COMPTEL,* in *Astronomy.* 1996, University of Amsterdam: Amsterdam.

131.van Hollebeke, M.A.I., L.S. Ma Sung, and F.B. McDonald, *The variation of solar proton energy spectra and size distribution with heliolongitude.* Solar Physics, 1975. **41**: p. 189.

132.van Hollebeke, M.A.I., *On solar cosmic rays.* Rev. Geophys. Space Phys., 1979. **17**: p. 545.

133.Vestrand, W.T. and J.A. Miller, *Particle Acceleration During Solar Flares,* in *The Many Faces of the Sun: A Summary of the Results from NASA's Solar Maximum Mission,* K.T. Strong, *et al.,* Editors. 1999, Springer-Verlag: New York. p. 231-272.

134.Vestrand, W.T., *et al., The Solar Maximum Mission Atlas of Gamma-Ray Flares.* Astrophysical Journal Supplement, 1999. **120**: p. 409.

135.Vlahos, L., T.E. Gergely, and K. Papadopoulos, *Electron acceleration and radiation signatures in loop coronal transients.* Astrophysical Journal, 1982. **258**: p. 812-822.

136.Weidenspointner, G., *The Nature of the 2.2 MeV Line in the Compton Telescope COMPTEL,* . 1994, Technical University of Munich: Munich.

137.Weinberg, A.M. and E.P. Wigner, *The Physical Theory of Nuclear Chain Reactors.* 1958, Chicago: University of Chicago Press.

138.Wild, J.P., S.F. Smerd, and A.A. Weiss, *Solar Bursts.* Annual Review of Astronomy and Astrophysics, 1963. **1**: p. 291-366.

139.Williams, M.M.R., *The Slowing Down and Thermalization of Neutrons.* 1966, New York: John Wiley and Sons, Inc. 582.

140.Winkler, C., *et al., Gamma-Ray Burst Detection Capabilities of COMPTEL.* Adv. Space Res., 1986. **6**(4): p. 113-117.

141.Young, C.A. and J.M. Ryan. *Neutron Transport in the Solar Atmosphere.* in *25th International Cosmic Ray Conference.* 1997. Durban, South Africa.

142.Zirin, H. and R.D. Lackner, *The Solar Flares of August 28 and 30, 1966.* Solar Physics, 1969. **6**: p. 86.

143.Zweibel, E. and D. Haber, *The Propagation of Energetic Ions in Magnetic Loops and Gamma-Ray Emission from Solar Flares.* Astrophysical Journal, 1983. **264**(Jan 15): p. 648-659.